

# A Thesis Title

*Author Name*

A dissertation submitted in partial fulfillment

of the requirements for the degree of

**Doctor of Philosophy**

of

**University College London.**

Department of Something

University College London

November 5, 2017

I, Author Name, confirm that the work presented in this thesis is my own. Where information has been derived from other sources, I confirm that this has been indicated in the work.

# **Abstract**

My research is about stuff.

It begins with a study of some stuff, and then some other stuff and things.

There is a 300-word limit on your abstract.

# **Acknowledgements**

Acknowledge all the things!

# Contents

<b>1</b>	<b>Introductory Material</b>	<b>23</b>
<b>2</b>	<b>An Incomplete Theory</b>	<b>24</b>
2.1	The Standard Model . . . . .	25
2.1.1	Particles . . . . .	25
2.1.2	Forces . . . . .	27
2.2	QCD: Hadronic Jet Formation and Dijet Production . . . . .	28
2.2.1	Renormalisation and the Running of $\alpha_S$ . . . . .	29
2.2.2	Hadronic Jet Formation . . . . .	30
2.2.3	Dijet Production in $pp$ Collisions . . . . .	31
2.2.4	A Special Case: $t\bar{t}$ . . . . .	37
2.3	Beyond the Standard Model . . . . .	39
2.3.1	Motivations for Beyond the Standard Model Physics . . . . .	39
2.3.2	Beyond Standard Model Theories . . . . .	42
<b>3</b>	<b>The ATLAS Detector</b>	<b>45</b>
3.1	The Large Hadron Collider . . . . .	45

## Contents

3.1.1 LHC running conditions in 2015 and 2016 . . . . .	45
3.2 ATLAS Detector Description . . . . .	46
3.2.1 ATLAS Co-ordinate System . . . . .	47
3.2.2 Inner Detector . . . . .	49
3.2.3 Calorimeters . . . . .	51
3.2.4 Muon Spectrometer . . . . .	55
3.2.5 Magnets . . . . .	56
3.3 Trigger . . . . .	57
<b>4 Object Definition and Reconstruction</b>	<b>59</b>
4.1 Tracks . . . . .	59
4.2 Jets . . . . .	61
4.2.1 Hadronic Topocluster Reconstruction . . . . .	62
4.2.2 Jet Reconstruction . . . . .	63
4.2.3 Jet Calibration . . . . .	66
4.2.4 Jet Energy Uncertainties . . . . .	69
4.3 $b$ -Jets . . . . .	71
4.3.1 Assigning a Flavour Label . . . . .	71
4.3.2 Baseline $b$ -tagging Algorithms . . . . .	71
4.3.3 Multi-Variate $b$ -tagging Algorithm . . . . .	74
4.3.4 Calibration and Uncertainties . . . . .	76
4.3.5 $b$ -Jet Energy Scale . . . . .	78

4.4	Electrons and Muons . . . . .	81
4.5	Further objects . . . . .	82
<b>5</b>	<b>Triggering in the di-<i>b</i>-jet analysis</b>	<b>83</b>
5.1	Jet-Triggers . . . . .	83
5.1.1	Level 1 . . . . .	84
5.1.2	HLT . . . . .	84
5.1.3	High-mass trigger selection . . . . .	84
5.2	<i>b</i> -Jet Triggers . . . . .	85
5.2.1	General description . . . . .	85
5.3	Efficiency Measurement of the <i>b</i> -Jet Trigger . . . . .	87
5.3.1	Strategy . . . . .	87
5.3.2	Datasets . . . . .	88
5.3.3	Event Selection . . . . .	89
5.3.4	The Initial Problem . . . . .	90
5.3.5	Investigation . . . . .	90
5.3.6	Solution: <i>b</i> -Jet Trigger GRL . . . . .	97
5.3.7	Efficiency Measurement and Systematic Derivation . . . . .	99
5.3.8	Cross-checks . . . . .	109
5.4	To Do . . . . .	110
<b>6</b>	<b>Di-<i>b</i>-jet Search: Outline and Event Selection</b>	<b>111</b>
6.1	Analysis Outline . . . . .	111

6.2	List of Data Sets Used . . . . .	113
6.3	Backgrounds and Signal . . . . .	114
6.4	Event Selection . . . . .	116
6.4.1	Jet Selection . . . . .	116
6.4.2	Event Level Cuts . . . . .	118
6.4.3	$b$ -Tagging . . . . .	119
6.4.4	Event Selection Summary . . . . .	122
<b>7</b>	<b>Di-<math>b</math>-jet Search: Search Phase</b>	<b>125</b>
7.1	Invariant Dijet Mass Spectrum . . . . .	125
7.2	Background Estimation . . . . .	126
7.2.1	Dijet Fit Functions . . . . .	126
7.2.2	Wilks' Statistic . . . . .	127
7.3	BumpHunter Algorithm . . . . .	128
7.4	<i>Summer16+15</i> Search Phase . . . . .	130
7.4.1	Background Modelling Strategy . . . . .	130
7.4.2	Fit Tests: Background-Only Dataset . . . . .	131
7.4.3	Fit Tests: Mass Range Studies . . . . .	132
7.4.4	Fit Tests: Spurious Signal . . . . .	135
7.4.5	Search Phase . . . . .	139
7.5	Full 2016 Search Phase . . . . .	140
<b>8</b>	<b>Di-<math>b</math>-jet Search: Limit Setting</b>	<b>141</b>

8.1	Bayesian Limits . . . . .	141
8.2	Systematic Uncertainties . . . . .	144
8.3	Limits: 2016_Summer . . . . .	146
8.4	Limits: 2016_Full . . . . .	149
<b>9</b>	<b>General Conclusions</b>	<b>150</b>
	<b>Appendices</b>	<b>151</b>
<b>A</b>	<b>Dijet Binning</b>	<b>151</b>
<b>B</b>	<b>Colophon</b>	<b>152</b>
<b>C</b>	<b>Contents Plan</b>	<b>153</b>
C.1	Introduction . . . . .	153
C.2	Theoretical Background . . . . .	153
C.3	ATLAS Detector . . . . .	153
C.4	Object Reconstruction And Calibration . . . . .	154
C.5	Trigger . . . . .	154
C.6	Event Selection . . . . .	154
C.7	Background Estimation and Search Phase . . . . .	154
C.8	Systematics and Limits Setting . . . . .	154
C.9	Looking Forward - What more can be done? . . . . .	154
C.10	Rough list of things I have done . . . . .	156

<i>Contents</i>	<b>10</b>
C.11 2014/15 - High $p_T$ b-tagging . . . . .	156
C.12 2015 - Validation of b-tagging in dijet events . . . . .	156
C.13 2015 Di-b-jet - Moriond . . . . .	156
C.14 2015 low mass Di-b-jet - LHCP . . . . .	157
C.15 Half 2016 high mass Di-b-jet - ICHEP . . . . .	157
C.16 2017 - bTrigger . . . . .	158
C.17 Full 2016 low mass Di-b-jet . . . . .	158
C.18 Event Display . . . . .	159
<b>Bibliography</b>	<b>160</b>

# List of Figures

2.1 A schematic showing the gluon propagator with the additional first order loops. . . . .	29
2.2 Summary of measurements of $\alpha_S$ as a function of the energy scale $Q$ . The respective degree of QCD perturbation theory used in the extraction of $\alpha_S$ is indicated in brackets (NLO: next-to-leading order; NNLO: next-to-next-to-leading order; res. NNLO: NNLO matched with resummed next-to-leading logs; N3LO: next-to-NNLO). . . . .	30
2.3 A Feynman diagram showing dijet production in a proton-proton collision through the $qg \rightarrow qg$ channel. . . . .	32
2.4 A Feynman diagram showing an example of a di-lepton $t\bar{t}$ event. . . . .	38
2.5 The leading-order Feynman diagram of the process $q\bar{q} \rightarrow Z' \rightarrow b\bar{b}$ . . . . .	42
2.6 The leading-order Feynman diagram of the process $bg \rightarrow b^* \rightarrow bg$ . . . . .	44
3.1 Cumulative luminosity versus time delivered to (green) and recorded by ATLAS (yellow) during stable beams for pp collisions at 13 TeV centre-of-mass energy in (a) 2015 and (b) 2016 . . . . .	46
3.2 A cut-away schematic of the ATLAS detector. . . . .	47

3.3	A visualisation of the ATLAS detector and the various sub-detectors. The view is taken as a slice in a plane perpendicular to the beam-pipe, showing the radial range from the beam-pipe to the edge of the detector. Overlaid are simplified illustrations of how various types of particles interact with the ATLAS detector; specifically from left to right the particles are an electron, a chargeless hadron (e.g. a neutron), a photon, a muon and a charged hadron (e.g. proton). The sub-detector components are not to scale. . . . .	48
3.4	A cut-away schematic of the ATLAS Inner Detector (ID). . . . .	50
3.5	A cut-away schematic of the ATLAS calorimeter system. . . . .	52
3.6	The layout of the ATLAS magnets. . . . .	56
3.7	A schematic of the ATLAS trigger and data-acquisition system in Run-2, with a focus on the components required for triggering. . . . .	58
4.1	A schematic illustrating the formation of hadronic jets and the resulting observed energy deposits in the calorimeter system. . . . .	61
4.2	A schematic illustrating the algorithm used to form a topocluster. The numbers on the grid represent $ S_{\text{cell}} $ and the colours represent the cell label. . .	63
4.3	A comparison of the jets formed using the (a) Cambridge-Aachen, (b) $k_T$ and (c) anti- $k_T$ algorithm from the same simulated event. The constituent clusters of each of the jets formed is indicated using various colours. . . .	66
4.4	Calibration stages for the EM+JES calibration scheme. . . . .	68
4.5	The fractional jet energy resolution uncertainty as a function of jet- $p_{\text{T}}$ and $\eta$ . The total uncertainty is shown as are the contributions from the various sources of uncertainty. . . . .	70
4.6	The fractional jet energy scale uncertainty as a function of jet- $p_{\text{T}}$ and $\eta$ . The total uncertainty is shown as are the contributions from the various sources of uncertainty. . . . .	70

4.7 A diagram to illustrate the key features of a $b$ -jet that are utilised by the base $b$ -tagging algorithms. . . . .	72
4.8 A diagram illustrating how three base flavour tagging algorithms are combined in the MV2 algorithm. . . . .	74
4.9 The expected $b$ -jet efficiency of $b$ -tagging algorithm, MV2, with respect to (a) light-jet and (b) $c$ -jet rejection in simulated $t\bar{t}$ events. The various lines show the performance of the algorithm for different configurations and training setups. . . . .	75
4.10 Ratio of b-tagging efficiency in data and Monte Carlo for the MV2c10 b-tagging algorithm at the 77% working point as a function of jet- $p_T$ , extracted using di-lepton $t\bar{t}$ events. Statistical uncertainties (black lines) and total uncertainties (green shaded region) are shown. . . . .	77
4.11 The total fractional $b$ JES uncertainty shown with the various contributions. . . . .	79
4.12 The validation of the $b$ JES uncertainty in data using the double-ratio $R'_{trk}$ . . . . .	80
5.1 The expected $b$ -jet efficiency of $b$ -jet triggers with respect to (a) light-jet and (b) $c$ -jet rejection in the case where the $b$ -tagging algorithm used is MV2c20 (Black), IP3D+SV1 (Blue) and for the set-up used in Run-1 (red stars). . . . .	86
5.2 The 60% $b$ -jet trigger efficiency with respect to an offline 70% operating point tag for Data (black) and simulation (red) against jet- $p_T$ (a) and jet- $\eta$ (b). The $b$ -trigger aware GRL is not applied and trigger matching is not required. . . . .	90
5.3 The 60% $b$ -jet trigger efficiency with respect to an offline 70% operating point tag for data from Epoch 1 (black) and simulation (red) against jet- $p_T$ (a) and online beamspot $z$ -position (b). The $b$ -jet trigger aware GRL has not been applied. . . . .	93

5.4 (a) The 60% $b$ -jet trigger efficiency with respect to an offline 70% operating point tag and (b) the number of offline jets passing 70% operating point tag and matching a HLT trigger jet against vertex class for data from Epoch 1 (black) and simulation (red). The $b$ -jet trigger aware GRL has not been applied. . . . .	93
5.5 The 60% $b$ -jet trigger efficiency with respect to an offline 70% operating point tag for data from epoch 2 (black) and simulation (red) against jet- $p_T$ (a), jet- $\eta$ (b) and online beamspot $z$ -position (c). . . . .	95
5.6 $b$ -perf efficiency, $\epsilon_{bPerf}$ , for data from Epoch 2 (black) and simulation (red) against leading-jet $p_T$ (a), online beamspot $z$ -position (b) and leading jet- $\eta$ (c). . . . .	95
5.7 The 60% $b$ -jet trigger efficiency with respect to an offline 70% operating point tag for data from Epoch 3 (black) and simulation (red) against (a) jet- $p_T$ , (b) jet- $\eta$ , (c) online beamspot $z$ -position and (d) vertex class. . . . .	96
5.8 The 60% $b$ -jet trigger efficiency with respect to an offline 70% operating point tag for data from Region 1 (black) and simulation (red) against jet- $p_T$ (a) and jet- $\eta$ (b). The $b$ -jet trigger aware GRL has been applied. . . . .	98
5.9 $b$ -perf efficiency, $\epsilon_{bPerf}$ , for data from Region 2 (black) and simulation (red) against leading (a) jet- $p_T$ and (b) jet- $\eta$ . The $b$ -jet trigger aware GRL has been applied. . . . .	98
5.10 The 60% $b$ -jet trigger efficiency with respect to an offline 70% operating point tag for the full 2016 data-set (black) and simulation (red) against jet- $p_T$ (a), jet- $\eta$ (b), online beamspot $z$ -position (c) and vertex class (d). . . . .	99
5.11 $b$ -perf efficiency, $\epsilon_{bPerf}$ , for the full 2016 data-set (black) and simulation (red) against (a) leading jet- $p_T$ and (b) jet- $\eta$ . The $b$ -jet trigger aware GRL has been applied. . . . .	99

5.12 A comparison of offline jets tagged at the 70% operating point for inclusive jets (red) and truth-matched b-jets (blue) against jet- $p_T$ (a) and jet- $\eta$ (b) in a simulated $t\bar{t}$ sample. . . . .	101
5.13 The 60% $b$ -jet trigger efficiency with respect to an offline 70% operating point tag for inclusive jets (black) compared to truth matched b-jets and non b-jets (a) and the case where non $b$ -jet content has been doubled (b) for a simulated $t\bar{t}$ sample. The lower panel in both plots show the ratio to the inclusive efficiency. . . . .	101
5.14 The 60% $b$ -jet trigger efficiency with respect to an offline 70% operating point tag for nominal inclusive case (black) compared to varied inclusive case (red) and just non $b$ -jets (blue) in the case where non $b$ -jet efficiency has been halved (a) and doubled (b) for a simulated $t\bar{t}$ sample. The lower panel in both plots show the ratio of the varied inclusive efficiency to the nominal inclusive efficiency. . . . .	102
5.15 A figure to demonstrate the high- $p_T$ extrapolation procedure for the 60% $b$ -jet trigger efficiency with respect to an offline 70% operating point tag. Data (black) is compared against simulation (red) after various corrections have been applied as a function of jet- $p_T$ . Panel (a) shows the flat normalisation fit uncorrected simulation, panel (b) shows the linear correction fit to normalised simulation, panel (c) shows the linear correction fit errors to the corrected simulation and panel (d) shows the quadratic fit to the corrected simulation. . . . .	104
5.16 The measured 60% $b$ -jet trigger efficiency with respect to an offline 70% operating point tag as measured in data as a function of offline jet- $p_T$ . The central values are shown in black with the statistical error and the green bands represent the total error including systematic errors. . . . .	106
5.17 Data/simulation scale factors for the 60% $b$ -jet trigger efficiency with respect to an offline 70% operating point tag as a function of offline jet- $p_T$ . The central values are shown in black with the statistical error and the green bands represent the total error including systematic errors. . . . .	106

5.18 The measured 60% $b$ -jet trigger efficiency with respect to an offline 70% operating point tag as measured in data (black) and from the corrected simulation (red) as a function of offline jet- $p_T$ . In the ratio plot on the lower panel the extrapolation errors is represented by the red band, whilst the total error is overlaid in green. . . . .	107
5.19 The measured $\varepsilon_{bPerf}$ as measured in data as a function of offline leading jet- $\eta$ . The central values are shown in black with the statistical error and the green bands represent the total error including systematic errors. . . . .	109
6.1 A cartoon illustrating the use of the dijet invariant mass ( $m_{jj}$ ) distribution in the search phase of the di- $b$ -jet analysis. Shown is the smoothly falling distribution from multijet QCD (SM) and a resonance shape caused by a Beyond Standard Model particle (BSM) . . . . .	112
6.2 The comparisons of the leading jet- $p_T$ using unprescaled L1_J75 trigger (black dots) to the HLT_J360 trigger (red dots), HLT_J380 trigger (green dots) and HLT_J400 trigger (blue dots) in one run of 2016 data. The ratio with respect to L1_J75 is shown in the lower panel. . . . .	117
6.3 The comparisons of the $m_{jj}$ distribution of events that pass an unprescaled L1_J75 trigger (black dots) to the events that pass the HLT_J380 trigger with leading jet- $p_T > 430$ GeV (red dots) and the HLT_J400 trigger with a leading jet- $p_T > 450$ GeV (green dots) in one run of 2016 data. The ratio with respect to L1_J75 is shown in the lower panel. . . . .	119
6.4 The dijet flavour composition of the simulated dijet background as a function of dijet mass, shown without applying $b$ -tagging (inclusive) and for $\geq 1$ $b$ -tag and 2 $b$ -tag categories. In the legend b, c and l refere to a truth matched $b$ -jet, $c$ -jet and light jet respectively. The <i>Summer16+15</i> dataset event selection has been applied. . . . .	121

6.5 Event displays showing high $m_{jj}$ events that pass the (a) 2 and (b) $\geq 1$ $b$ -tag di- $b$ -jet event selection. The left section of the figures show a cut-away of the ATLAS detector; the inner detector is shown in purple, the hadronic calorimeter is shown in blue and the toroid magnet and supporting structure is shown in black and grey. The upper right section of the figures show a close-up view of the inner tracker in the $r - z$ plane. In both sections tracks inside the inner detector are shown in orange and energy deposits in the EM and hadronic calorimeter are shown in cyan and yellow respectively. The two leading jets formed are indicated by the cones, where a blue cone indicates that the jet has been $b$ -tagged and a yellow cone shows that it has not. The yellow spheres show the primary vertex candidates and the red spheres show the secondary vertex candidates. . . . .	123
6.6 Plots to show the acceptance of the <i>Summer16+15</i> data-set event selection for the $b^*$ quark and $Z'$ -boson signal models. Panel (a) shows the signal acceptance multiplied by trigger efficiency as a function of the simulated mass of the signal model, in the case where $b$ -tagging has been applied and not. Panel (b) shows the event tagging efficiency as a function of the dijet invariant mass, $m_{jj}$ , for a range of simulated masses, $m$ , as indicated on the plot. In both figures the $b$ -tagging categories used are indicated in the legend. Details of the <i>Summer16+15</i> data-set event selection are described in the text. . . . .	124
7.1 The Wilks' $p$ -value as a function of luminosity in the case that the 3 parameter is the nominal function and the 4 parameter is the alternate (blue) and the case where the 4 parameter is the nominal function and the 5 parameter is the alternate (purple) for a $8.8 \text{ fb}^{-1}$ subset of data in the (a) 2 $b$ -tag and (b) $\geq 1$ $b$ -tag category. The <i>Summer16+15</i> data-set event selection has been applied. . . . .	131

7.2 The scaled invariant mass distribution (red) compared to the effective entries of the invariant mass distribution (green) of Monte-Carlo simulation for the (a) 2 $b$ -tag and (b) $\geq 1$ $b$ -tag category. The <i>Summer16+15</i> dataset event selection has been applied.	132
7.3 The invariant mass distribution taken from multi-jet simulation for the (a) 2 $b$ -tag and (b) $\geq 1$ $b$ -tag, category, fitted to using the 4 parameter fit function, with lower mass bound of the fit range $m_{jj} = 1100$ GeV. The BumpHunter algorithm is run to identify the most discrepant excess, as indicated by the blue lines. Pseudo-experiments are used to assign the excess a $p$ -value, which is shown on the plot. The <i>Summer16+15</i> dataset event selection has been applied.	133
7.4 The invariant mass distribution taken from multi-jet simulation for the (a) 2 $b$ -tag and (b) $\geq 1$ $b$ -tag, category, fitted to using the 5 parameter fit function, with lower mass bound of the fit range $m_{jj} = 1100$ GeV. The BumpHunter algorithm is run to identify the most discrepant excess, as indicated by the blue lines. Pseudo-experiments are used to assign the excess a $p$ -value, which is shown on the plot. The <i>Summer16+15</i> dataset event selection has been applied.	134
7.5 The distribution of the (a) BumpHunter, (b) DeficitHunter and (c) $\chi^2$ $p$ -values for different values of lower mass bound of the fit range, when fitting to 2 $b$ -tag category invariant mass distribution taken from multi-jet simulation with the 4 parameter fit function. The <i>Summer16+15</i> dataset event selection has been applied, with the exception of the $m_{jj}$ cut.	135
7.6 The distribution of the (a) BumpHunter, (b) DeficitHunter and (c) $\chi^2$ $p$ -values for different values of lower mass bound of the fit range, when fitting to $\geq 1$ $b$ -tag category invariant mass distribution taken from multi-jet simulation with the 4 parameter fit function. The <i>Summer16+15</i> dataset event selection has been applied, with the exception of the $m_{jj}$ cut.	135

7.7 The invariant mass distribution taken from multi-jet simulation for the (a) 2 $b$ -tag and (b) $\geq 1$ $b$ -tag, category, fitted to using the 4 parameter fit function, with lower mass bound of the fit range $m_{jj} = 1378$ GeV. The BumpHunter algorithm is run to identify the most discrepant excess, as indicated by the blue lines. Pseudo-experiments are used to assign the excess a $p$ -value, which is shown on the plot. The <i>Summer16+15</i> dataset event selection has been applied. . . . .	136
7.8 The scaled invariant mass distribution (red) compared to the effective entries of the invariant mass distribution (green) for the 2 $b$ -tag category, for the (a) 2 $b$ -tag and (b) $\geq 1$ $b$ -tag case. Overlaid is a data-like distribution (blue) created by applying Poisson fluctuations to the scaled distribution. The <i>Summer16+15</i> dataset event selection has been applied. . . . .	137
7.9 A data-like distribution taken from multi-jet simulation for the (a) 2 $b$ -tag and (b) $\geq 1$ $b$ -tag, category, fitted to using the 3 parameter fit function. The BumpHunter algorithm is run to identify the most discrepant excess, as indicated by the blue lines. Pseudo-experiments are used to assign the excess a $p$ -value, which is shown on the plot. The <i>Summer16+15</i> dataset event selection has been applied. . . . .	137
7.10 The distribution of the BumpHunter test statistic for 10,000 pseudo experiments compared to the value observed in a data-like distribution from the (a) 2 $b$ -tag category and (b) $\geq 1$ $b$ -tag category. The fraction of pseudo-experiments with a BumpHunter test statistic greater than the value in data is the estimation of the respective $p$ -value. . . . .	138
7.11 The distribution of (a) BumpHunter, (b) DeficitHunter and (c) $\chi^2$ $p$ -values for fits to 200 data-like invariant mass spectra in the 2 $b$ -tag category. The <i>Summer16+15</i> dataset event selection has been applied. . . . .	139
7.12 The distribution of (a) BumpHunter, (b) DeficitHunter and (c) $\chi^2$ $p$ -values for fits to 200 data-like invariant mass spectra in the $\geq 1$ $b$ -tag category. The <i>Summer16+15</i> dataset event selection has been applied. . . . .	139

7.13 The final <i>Summer16+15</i> data-set in the (a) 2 $b$ -tag and the (b) $\geq 1$ $b$ -tag category, where the background has been modelled using the 3 parameter dijet fit function. The upper panel shows the data compared to the background estimate, benchmark signal models with enhanced cross sections are overlaid. The lower panel shows the significance of the difference between the data and the background estimate. The most discrepant excess as found by the BumpHunter algorithm is indicated by the vertical blue lines and the $p$ -value of this excess is printed on the plot. . . . .	140
8.1 The background systematic uncertainties for the (a) 2 and (b) $\geq 1$ $b$ -tag categories as a function of dijet invariant mass, $m_{jj}$ , for the <i>Summer16+15</i> data-set. The red shaded region shows the function parameter uncertainty and the function choice uncertainty is shown by the blue line. . . . .	146
8.2 Bayesian 95% confidence level upper limits on cross-section times acceptance times tagging efficiency for the (a) $Z'$ -boson and (b) $b^*$ -quark as a function of simulated mass using the <i>Summer16+15</i> data-set in the 2 and $\geq 1$ $b$ -tag category respectively. The observed limit is shown by the solid black line, the expected limit is shown by the dotted black line and the 1 and 2 $\sigma$ error bands on the expected limit are shown by the green and yellow bands. The theoretical prediction of $\sigma \times A \times \varepsilon$ for the Sequential Standard Model (SSM) and leptophobic $Z'$ -boson and the $b^*$ -quark are overlaid. . . .	147
8.3 95% confidence observed upper limits on the product of cross-section, detector acceptance, tagging efficiency and branching ratio, $\sigma \times A \times \varepsilon \times BR$ , for Gaussian signals for both $b$ -tagging categories using the <i>Summer16+15</i> data-set. The Gaussian widths considered are 15%, 10% and 7% of the simulated mass in addition to a Gaussian with the width of the detector mass resolution. . . . .	149

# List of Tables

2.1	The key properties of the 6 flavours of quark in the Standard Model, organised into the three generations of quarks. . . . .	25
2.2	The 6 types of lepton in the Standard Model and their key properties, organised into the three generations of leptons. Neutrino masses are not well known. . . . .	26
2.3	The key properties of the bosons of the Standard Model. . . . .	26
2.4	A table showing $S(ij \rightarrow kl)$ , the process dependant part of the parton cross-section, for all possible processes. The indices refer to quark flavour, if no indices are used then the same flavour is used for all quarks in that process.	34
2.5	MMHT2014 NNLO PDFs at $Q^2 = 10 \text{ GeV}^2$ and $Q^2 = 10^4 \text{ GeV}^2$ , with associated 68% confidence-level uncertainty bands. . . . .	35
3.1	The key spatial coverage, granularity and readout parameters of the ATLAS calorimeter. . . . .	54
4.1	The Mv2c10 b-tagging algorithm operating points; with the corresponding $b$ -jet efficiency, $c$ -jet rejection, light-jet rejection and $\tau$ rejection. . . . .	76
5.1	A table describing the effect of not finding a valid xPrmVtx primary vertex on different epochs of data. . . . .	91
5.2	A table showing the systematic assigned for the high- $p_T$ extrapolation. . . .	103

5.3	A table showing the jet-level Data/simulation scale factor (SF) as a function of jet- $p_T$ with total error and the contributions of the different systematics considered; specifically statistical, high- $p_T$ extrapolation, non- $b$ -jet purity and non- $b$ -jet trigger efficiency. . . . .	105
5.4	A table showing the event-level Data/MC scale factor (SF) as a function of leading jet- $\eta$ with total error and the contributions of the different systematics considered. . . . .	109
6.1	The estimated $S/\sqrt{B}$ at $18.9 \text{ fb}^{-1}$ for 4 different MV2c10 operating points (OP). $S$ is estimated using a SSM $Z'$ -boson and $B$ is estimated using a $18.9 \text{ fb}^{-1}$ subset of 2 $b$ -tag category data. The <i>Full16+15_HighMass</i> data-set event selection has been applied. Three different mass points are considered and the mass windows used to estimate $S$ and $B$ for each mass point are shown in the table [88]. . . . .	120
6.2	A summary of the key event selections applied in the di- $b$ -jet analysis for each of the data-sets considered. For full details refer to the text. . . . .	122
7.1	The dijet fit function equations. The fit functions are named by the number of free parameters used. $p_i$ are the free parameters of the fit function . . . . .	127
8.1	A table summarising the signal systematic uncertainties used in the <i>Summer16+15</i> data-set. Jet Energy Scale (JES), Jet Energy Resolution (JER) and $b$ -Jet Energy Scale ( $b$ JES) are uncertainties on the dijet invariant mass of a simulated event, whilst $b$ -tagging, PDF and luminosity uncertainties are uncertainties on the simulated event weight. . . . .	146

## **Chapter 1**

# **Introductory Material**

Lorem ipsum dolor sit amet, consectetuer adipiscing elit. Etiam lobortis facilisis sem. Nullam nec mi et neque pharetra sollicitudin. Praesent imperdiet mi nec ante. Donec ullamcorper, felis non sodales commodo, lectus velit ultrices augue, a dignissim nibh lectus placerat pede. Vivamus nunc nunc, molestie ut, ultricies vel, semper in, velit. Ut porttitor. Praesent in sapien. Lorem ipsum dolor sit amet, consectetuer adipiscing elit. Duis fringilla tristique neque. Sed interdum libero ut metus. Pellentesque placerat. Nam rutrum augue a leo. Morbi sed elit sit amet ante lobortis sollicitudin. Praesent blandit blandit mauris. Praesent lectus tellus, aliquet aliquam, luctus a, egestas a, turpis. Mauris lacinia lorem sit amet ipsum. Nunc quis urna dictum turpis accumsan semper.

## Chapter 2

# An Incomplete Theory

One of the great questions that humans have always tried to answer is what are the fundamental building blocks of the universe and what are the rules that govern them? Attempts at answering this question have ranged from the philosophical approach of ‘*atomism*’ by the ancient Greeks [1] to the discovery of atomic structure by Ernest Rutherford [2].

The current best answer to this question is the ‘*Standard Model of Particle Physics*’, a mathematical description of a finite set of fundamental particles and their interactions. The Standard Model’s ability to describe data is formidable and as such it is the foundation of the field of Particle Physics. However, it is known that this is not a complete theory and there must be a deeper underlying theory that lies beyond the Standard Model.

This chapter firstly aims to describe the Standard Model and its key predictions with respect to the analyses presented in this thesis. Section 2.1 briefly describes the Standard Model and Section 2.2 outlines the QCD description of jet formation and dijet production in proton-proton collisions. Then, Section 2.3 will discuss Beyond the Standard Model (BSM) physics; specifically the problems in the Standard Model that require BSM physics and proposed BSM models that predict resonances preferentially decaying to one or two  $b$ -quarks.

## 2.1 The Standard Model

The Standard Model is a quantum field theory, meaning that the theory describes a finite set of particles and their interactions in terms of a set of fields. The end product of the Standard Model is a prediction of what will happen when any two particles in nature interact; which in the context of a collider experiment means predicting what is the cross-section of any given interaction.

Section 2.1.1 contains a description of the particles that make up the Standard Model and Section 2.1.2 contains a description of the types of interactions between the particles, known as forces.

### 2.1.1 Particles

There are 18 fundamental particles in the Standard Model, where fundamental means that they are not composed of other constituent particles. These particles are grouped into three families with similar properties; known as quarks, leptons and bosons. Details on the particles in the Standard Model is taken from [3], where a full description can be found.

- **Quarks:** Quarks are fermions that interact with the strong force; a description of the strong force is in the next section. There are 6 different types of quarks, known as flavours, arranged in 3 generations. Table 2.1 summarises the flavours of quark and their key properties. For each quark there is also an anti-quark, which has identical mass and spin, but opposite charge and quantum numbers.

Quark Flavour	Symbol	Charge	Spin	Mass [GeV]
Up	$u$	$+\frac{2}{3}$	$\frac{1}{2}$	0.002
Down	$d$	$-\frac{1}{3}$	$\frac{1}{2}$	0.005
Charm	$c$	$+\frac{2}{3}$	$\frac{1}{2}$	1.3
Strange	$s$	$-\frac{1}{3}$	$\frac{1}{2}$	0.096
Top	$t$	$+\frac{2}{3}$	$\frac{1}{2}$	173
Bottom	$b$	$-\frac{1}{3}$	$\frac{1}{2}$	4.2

**Table 2.1:** The key properties of the 6 flavours of quark in the Standard Model, organised into the three generations of quarks.

- **Leptons:** Leptons are fermions that, unlike the quarks, do not interact with the strong force. There are 6 different types of leptons, arranged into 3 generations, each containing a charge -1 particle and a charge 0 neutrino. Table 2.2 summarises the leptons and their key properties. Neutrinos masses are not well known, but they are known to be non-zero and the sum of the masses of the three flavours of neutrino is less than a few eV [4], hence are negligible compared to the other particles of the Standard Model. For each lepton there is also an anti-lepton.

Lepton	Symbol	Charge	Spin	Mass [GeV]
Electron	$e$	-1	$\frac{1}{2}$	$5.1 \times 10^{-4}$
Electron Neutrino	$\nu_e$	0	$\frac{1}{2}$	-
Muon	$\mu$	-1	$\frac{1}{2}$	0.11
Muon Neutrino	$\nu_\mu$	0	$\frac{1}{2}$	-
Tau	$\tau$	-1	$\frac{1}{2}$	1.8
Tau Neutrino	$\nu_\tau$	0	$\frac{1}{2}$	-

**Table 2.2:** The 6 types of lepton in the Standard Model and their key properties, organised into the three generations of leptons. Neutrino masses are not well known.

- **Bosons:** There are a set of integer-spin particles in the Standard Model, known as bosons. The bosons of the Standard Model act as the mediators of the forces that will be described below. Table 2.3 summarises the bosons and their key properties.

Boson	Symbol	Charge	Spin	Mass [GeV]
Photon	$\gamma$	0	1	0
W-boson	$W^\pm$	$\pm 1$	1	80
Z-boson	$Z_0$	0	1	91
Gluon	$g$	0	1	0
Higgs Boson	$H$	0	0	125

**Table 2.3:** The key properties of the bosons of the Standard Model.

### 2.1.2 Forces

The Standard Model combines three key theories in a  $SU(3) \times SU(2) \times U(1)$  gauge symmetry. The first key theory is the electro-weak theory [5]; this theory is based on mixing within the symmetry group  $SU(2) \times U(1)$  leading to three distinct interaction types grouped into two forces: the electro-magnetic and weak forces. The second is Quantum Chromodynamics (QCD) [6] which describes the strong force. Finally, the Brout-Englert-Higgs Mechanism [7, 8] describes the origin of mass in the Standard Model.

The properties of each force are discussed below:

- **Electro-magnetic (EM):**

The EM force is an interaction between charged particles and is mediated by the photon. The strength of a force is often given in terms of the coupling constant,  $\alpha$ . In this case the EM coupling is proportional to the EM coupling constant,  $\alpha_{EM}$ , multiplied by the product of the charges of the two particles, where  $\alpha_{EM} \sim 1/137$ .

- **Weak Force:**

The weak force is composed of the two remaining interactions from electro-weak theory; the neutral current interaction and the charged current interaction.

The neutral current interaction is mediated by the  $Z_0$  boson, has a universal interaction to all fermions, and does not allow flavour changing interactions.

The charged current interaction is mediated by the  $W^+$  and  $W^-$  boson, has a universal interaction with all fermions, and flavour changing interactions are allowed. In the quark sector, the charged current interaction couples with weak eigenstates of fermions rather than their flavour eigenstates, allowing for interactions that change the generation of the quark's flavour. The relative amplitudes of each flavour changing interaction is described by the CKM matrix; the values of this matrix highly suppresses generational changing interactions involving the 3rd generation of quarks. Both interactions of the weak force are much weaker than the EM force due to the large masses of the mediating particles ( $\text{Weak}/\text{EM} \sim 10^{-4}$ ).

- **Strong Force:**

Quantum Chromodynamics (QCD) is a theory based on a  $SU(3)$  gauge symmetry that

describes the strong force. The strong force is mediated by the gluon and interacts with particles that have colour charge; which are quarks and gluons. The fact that the gluon has colour charge means that the gluon is self interacting. The  $SU(3)$  symmetry results in 3 colour charges: known as red, green and blue. An anti-quark has colour charge anti-red, anti-blue or anti-green. A colour neutral object can be formed if all three colour charges are present (i.e. in a baryon containing three quarks) or if a colour and the corresponding anti-colour is present (i.e. in a meson that contains  $q\bar{q}$ ). QCD is important in terms of understanding hadronic jet formation and the production of the largest background in a di- $b$ -jet search, so further discussion of QCD is found in Section 2.2.

- **Higgs Mechanism:** The Higgs mechanism <sup>1</sup> introduces an extra scalar field to the Standard Model with a Higgs potential given by the so-called ‘Mexican-hat potential’. This allows for spontaneous symmetry breaking which gives mass to the bosons of the Standard Model. In addition, a Yukawa coupling term between the scalar field and the fermions gives rise to the mass of the fermions <sup>2</sup>. A final prediction of the Higgs mechanism is the existence of a spin-0 boson, known as the Higgs boson. The first observation of a Higgs boson like object by the ATLAS [9] and CMS [10] experiments in 2012 appears to confirm the Higgs mechanism, which is seen as a great triumph of the Standard Model.

## 2.2 QCD: Hadronic Jet Formation and Dijet Production

As described above Quantum Chromodynamics (QCD) is a theory that describes the strong interaction between quarks and gluons. QCD therefore describes two elements that are critical to the analysis being presented in this thesis; specifically the formation of hadronic jets and the production of dijet events through QCD in proton-proton collisions, which will be the dominant background in the analysis presented in this thesis.

This section will firstly describe renormalisation of QCD, which is important for understanding how QCD works, and will then describe the process of hadronic jet formation and dijet production in hadron collisions. Quarks and gluons can often fill similar roles in hadronic jet formation and dijet production, hence I will refer to them collectively as ‘partons’ in this section.

---

<sup>1</sup>Also known as the Higgs-Englert-Brout mechanism

<sup>2</sup>With the exception of the neutrinos, whose mass is not described by the Standard Model

### 2.2.1 Renormalisation and the Running of $\alpha_S$

For any calculation in QCD, or indeed any quantum field theory, one must consider the higher-order loop diagrams; for example a simple gluon propagator has additional first-order loops as shown in Figure 2.1. The summation over all higher-order loops leads to divergences in calculations of scattering events in QCD.

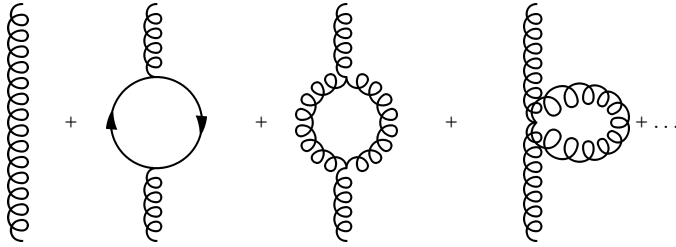


**Figure 2.1:** A schematic showing the gluon propagator with the additional first order loops [11].

To avoid these divergences, there is a well accepted mathematical tool, known as renormalisation, where one effectively re-scales the fields in the Lagrangian. Renormalisation is done such that the divergences are removed and one can perform calculations of QCD in a perturbative expansion. This leads to a dependence of the strong coupling constant,  $\alpha_S$ , on the renormalisation scale used,  $\mu_R$ , an effect known as the running of  $\alpha_S$ . To get an effective strength of the strong interaction in any given process, one sets the value of  $\mu_R$  to be the scale of the momentum transfer  $Q$  of the process. The running of  $\alpha_S$  can be measured through experimental observation; Figure 2.2 shows the measured values of  $\alpha_S$  as a function of the energy scale,  $Q$ , in a range of experiments.

There are three features of Figure 2.2 that can be noted. Firstly, the size of  $\alpha_S$  is generally large compared to  $\alpha_{EM}$ ; this means that, depending on the energy scale, the strong force is typically stronger than the EM force by one or two orders of magnitude. Secondly, at high-energies/low-distance scales the strong force becomes relatively weak, this phenomenon is known as '*asymptotic freedom*'. At these energy scales, perturbative expansions of QCD are possible. Finally, at low-energies/large-distance scales the strong force is exceptionally strong. As a result, if two interacting quarks become separated by a large distance then it becomes energetically favourable to pair-produce  $q\bar{q}$  pairs from the vacuum until a colour neutral object can be formed. Therefore quarks are not observed in isolation,

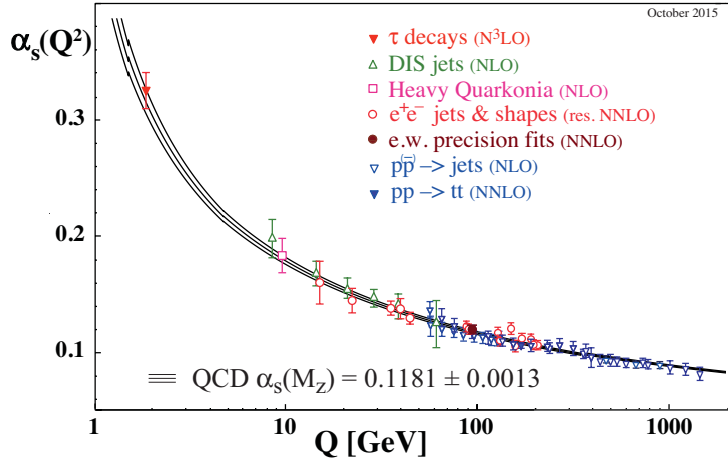


**Figure 2.2:** Summary of measurements of  $\alpha_s$  as a function of the energy scale  $Q$ . The respective degree of QCD perturbation theory used in the extraction of  $\alpha_s$  is indicated in brackets (NLO: next-to-leading order; NNLO: next-to-next-to leading order; res. NNLO: NNLO matched with resummed next-to-leading logs; N3LO: next-to-NNLO) [6].

but instead quarks form colour neutral hadrons; this feature of QCD is known as ‘*confinement*’.

### 2.2.2 Hadronic Jet Formation

It is common in hadronic colliders that a high-momentum quark or gluon will be produced in the final-state<sup>3</sup>. However, due to the effect of quark confinement described above, an isolated quark or gluon will not be observed. Instead a stream of energetic, collimated hadrons will be formed, known as a hadronic jet. Hadronic jet formation occurs through two distinct processes; parton-shower and hadronisation.

- **Parton Shower:**

The high-energy final-state quark or gluon has a finite probability of splitting into a quark-gluon or quark-quark pair respectively. The resulting quarks and gluons will also undergo splitting to form more partons, which in turn can split. This process continues to form the parton shower. Due to relativistic effects, each splitting will generally be at a small opening angle in the lab-frame and as such the partons will be highly collimated in the direction of the initial parton. The parton shower process occurs at high energy such that the value of  $\alpha_s$  is small and thus perturbative expansions of QCD can be used to perform calculations. However, at each step of the splitting the energy of the partons

---

<sup>3</sup>an example of this is dijet production, as will be described in Section 2.2.3.

decreases and thus the value of  $\alpha_S$  increases.

- **Hadronisation:**

When the energy scale becomes small<sup>4</sup>,  $\alpha_S$  becomes large such that the dominant QCD effect is quark confinement. Therefore,  $q\bar{q}$  pairs are produced until the quarks resulting from the parton shower can form hadrons. The hadrons are colour neutral objects, meaning that stable hadrons that do not interact through QCD will be formed<sup>5</sup>. The hadronisation process occurs at large values of  $\alpha_S$  so cannot be calculated using perturbative expansions; models such as the string model [12] and the cluster model [13] are used to simulate hadronisation.

The end result of the hadronisation process is a set of collimated stable hadrons, known as a hadronic jet, which can be observed in an experiment. Note that our understanding of how one goes from an initial parton to a hadronic jet is model dependant, for example there is a choice of hadronisation model. Hence, in experiment we remove this dependence by defining a jet in terms of observables, such that the experimental results are model-independent and results can be reinterpreted when improved models become available<sup>6</sup>. The details of the experimental definition of a hadronic jet is discussed in Section 4.2.

### 2.2.3 Dijet Production in $pp$ Collisions

Dijet production is one of the most common process that occurs in any hadron collider. The first step of dijet production in  $pp$  colliders is the two protons interacting through QCD to give two quarks or gluons in the final state; the frequency of this interaction is described by the hadronic cross-section,  $\sigma_{had}$ . The free partons will then form hadronic jets through the processes described in Section 2.2.2, which can be observed. Figure 2.3 shows the Feynman diagram of dijet production in a proton-proton collision through the  $qg \rightarrow qg$  channel.

---

<sup>4</sup>This is generally defined as small relative to the hadronic scale,  $\Lambda$ , which is typically a few hundred MeV

<sup>5</sup>Some unstable hadrons, such as a  $\Delta^{++}$ , may be initially formed in the process but these will decay rapidly through the strong interaction. In addition, some hadrons might not be stable under the weak interaction, such as a Kaon, but the time-scale of their decays will be much larger.

<sup>6</sup>A good explanation of why model-independent jets is desirable is found here [14]

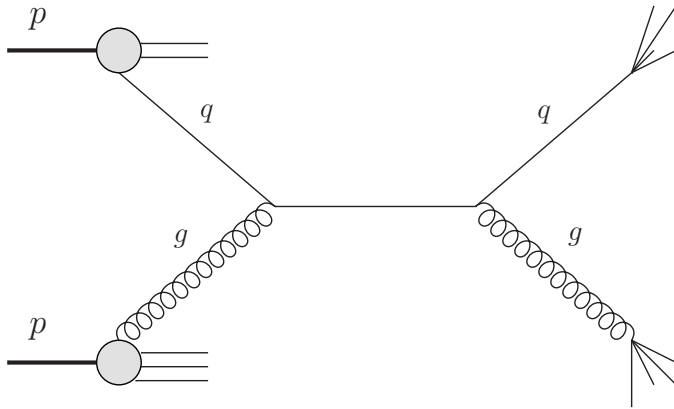


**Figure 2.3:** A Feynman diagram showing dijet production in a proton-proton collision through the  $qg \rightarrow qg$  channel. Adapted from [15].

### 2.2.3.1 Factorisation

To calculate the hadronic cross-section,  $\sigma_{had}$ , in a proton-proton collision, two elements are separated out in a process called factorisation.

The first element is the parton-level cross-section,  $\hat{\sigma}$ , which is the cross-section of two partons from the proton ( $p_i$  and  $p_j$ ) scattering to give two final state partons ( $p_k$  and  $p_l$ ). This is effectively the central part of the Feynman diagram in Figure 2.3.

The second element is the Parton Density Functions (PDFs),  $F_i(x_i)$ , which give the number density of a specific parton,  $p_i$ , with momentum fraction,  $x_i$ , in a proton. Momentum fraction is defined as the fraction of the proton's total momentum that the parton is carrying,  $x = p_{\text{parton}}/p_{\text{proton}}$ . The number density affects the overall cross-section, as it changes the probability that a specific parton can form the initial parton propagators. This part of the interaction is indicated by the circles in the top and bottom left of the Feynman diagram in Figure 2.3.

The elements are combined to calculate  $\sigma_{had}$ :

$$\sigma_{had} = \sum_{i,j,k,l} \int dx_i dx_j F_i(x_i, Q^2) F_j(x_j, Q^2) \hat{\sigma}(p_i, p_j \rightarrow p_k p_l) \quad (2.1)$$

where there is an integral over all possible values of momentum fractions  $x_i$  and  $x_j$ , a sum over all possible initial partons from the two protons labelled  $i$  and  $j$ , and a sum over all

possible final-state partons labelled by  $k$  and  $l$ <sup>7</sup>.  $Q^2$  is the energy scale of the collision.

With the two elements separated we can discuss each separately.

### 2.2.3.2 Parton-level Cross-Section

To describe the parton-level cross-section we must first define a few variables. The first is the invariant mass of the outgoing partons,  $m_{kl}$ , which is given in terms of the four-momentum of the two partons;

$$m_{kl}^2 = (p_k^\mu + p_l^\mu)^2 \quad (2.2)$$

Then there are two related angular variables,  $y^*$  and  $\theta^*$ , defined in terms of the rapidities of the outgoing partons,  $y_k$  and  $y_l$ ;

$$y^* = \left( \frac{y_k - y_l}{2} \right), \quad (2.3)$$

$$\cos(\theta^*) = \tanh(y^*) \quad (2.4)$$

Finally the Mandelstam variables, generally used to describe a 2→2 particle scatter event, are defined as

$$\hat{s} = m_{kl}^2, \quad \hat{t} = -\hat{s}(1 - \cos \theta^*), \quad \hat{u} = -\hat{s}(1 + \cos \theta^*) \quad (2.5)$$

The parton-level cross-section of incoming partons  $i$  and  $j$  scattering to give outgoing partons  $k$  and  $l$  is given in terms of the variables  $\theta^*$  and  $m_{kl}$  [16];

$$\frac{d\hat{\sigma}(p_i, p_j \rightarrow p_k p_l)}{dm_{kl} d\cos \theta^*} = \frac{\pi \alpha_s}{m_{kl}} S(ij \rightarrow kl) \frac{1}{1 + \delta_{kl}} \quad (2.6)$$

Where  $S(ij \rightarrow kl)$  gives the process dependant kinematics of a  $ij \rightarrow kl$  parton scatter.  $S(ij \rightarrow kl)$  for each process is given in Table 2.4.

---

<sup>7</sup>The final state sums do not include top-quarks because, as will be discussed in Section 2.2.4, they do not form regular jets. In addition, due to its heavy mass, the top-quark is heavily suppressed in the PDFs so can be ignored in the sum over initial partons.

Subprocess	$\mathcal{S}(ij \rightarrow kl) = \frac{\hat{s}^2}{\pi \alpha_s^2} \frac{d\hat{\sigma}}{dt}(ij \rightarrow kl)$
$q_1 q_2 \rightarrow q_1 q_2$	$\frac{4}{9} \frac{\hat{s}^2 + \hat{u}^2}{\hat{t}^2}$
$q_1 \bar{q}_2 \rightarrow q_1 \bar{q}_2$	$\frac{4}{9} \frac{\hat{s}^2 + \hat{u}^2}{\hat{t}^2}$
$qq \rightarrow qq$	$\frac{4}{9} \left( \frac{\hat{s}^2 + \hat{u}^2}{\hat{t}^2} + \frac{\hat{s}^2 + \hat{t}^2}{\hat{u}^2} \right) - \frac{8}{27} \frac{\hat{s}^2}{\hat{u}\hat{t}}$
$q_1 \bar{q}_1 \rightarrow q_2 \bar{q}_2$	$\frac{4}{9} \frac{\hat{t}^2 + \hat{u}^2}{\hat{s}^2}$
$q\bar{q} \rightarrow q\bar{q}$	$\frac{4}{9} \left( \frac{\hat{s}^2 + \hat{u}^2}{\hat{t}^2} + \frac{\hat{s}^2 + \hat{t}^2}{\hat{u}^2} \right) - \frac{8}{27} \frac{\hat{u}^2}{\hat{s}\hat{t}}$
$q\bar{q} \rightarrow gg$	$\frac{32}{27} \frac{\hat{t}^2 + \hat{u}^2}{\hat{t}\hat{u}} - \frac{8}{3} \frac{\hat{t}^2 + \hat{u}^2}{\hat{s}^2}$
$gg \rightarrow q\bar{q}$	$\frac{1}{6} \frac{\hat{t}^2 + \hat{u}^2}{\hat{t}\hat{u}} - \frac{3}{8} \frac{\hat{t}^2 + \hat{u}^2}{\hat{s}^2}$
$gq \rightarrow gq$	$-\frac{4}{9} \frac{\hat{s}^2 + \hat{u}^2}{\hat{s}\hat{u}} + \frac{\hat{u}^2 + \hat{s}^2}{\hat{t}^2}$
$gg \rightarrow gg$	$\frac{9}{2} \left( 3 - \frac{\hat{t}\hat{u}}{\hat{s}^2} - \frac{\hat{s}\hat{u}}{\hat{t}^2} - \frac{\hat{s}\hat{t}}{\hat{u}^2} \right)$

**Table 2.4:** A table showing  $S(ij \rightarrow kl)$ , the process dependant part of the parton cross-section, for all possible processes. The indices refer to quark flavour, if no indices are used then the same flavour is used for all quarks in that process. Taken from Table 1 of [16].

### 2.2.3.3 Parton Density Functions

A naive model of the proton contains two up-quarks and a down-quark, known as valence quarks, each carrying  $\frac{1}{3}$  of the proton's momentum. However, QCD interactions within the proton mean that gluons can be emitted from the valence quarks and  $q\bar{q}$  pairs can be produced from the emitted gluons. This means that, in reality, the proton is made up of the three valence quarks, typically carrying a large fraction of the proton's momentum, in addition to a sea of quarks and gluons from QCD effects, that will typically carry a lower fraction of the proton's momentum.

Parton Density Functions (PDFs) give the number density of a specific parton  $p_i$  in a proton  $P_i$  for a given momentum fraction  $x_i$  and energy scale,  $Q$ . Due to the large value of  $\alpha_S$  in the proton, QCD cannot be considered in perturbative expansions and as such the PDFs cannot be calculated directly. Instead the PDFs can be measured by combining a range of experimental scattering results. In particular, strong constraints on the PDFs come from deep inelastic scattering using  $ep$  colliders, such as HERA [17]; the strong constraints are due, in part, to there only being one parton in the collision allowing direct access to the PDFs in a cross-section measurement.

Figure 2.5 shows the  $xF(x, Q^2)$  for a  $Q^2$  of 10 and  $10^4$  GeV $^2$  from the MMHT2014 PDF set [18]. The various coloured lines represent the PDF for each of the different partons.

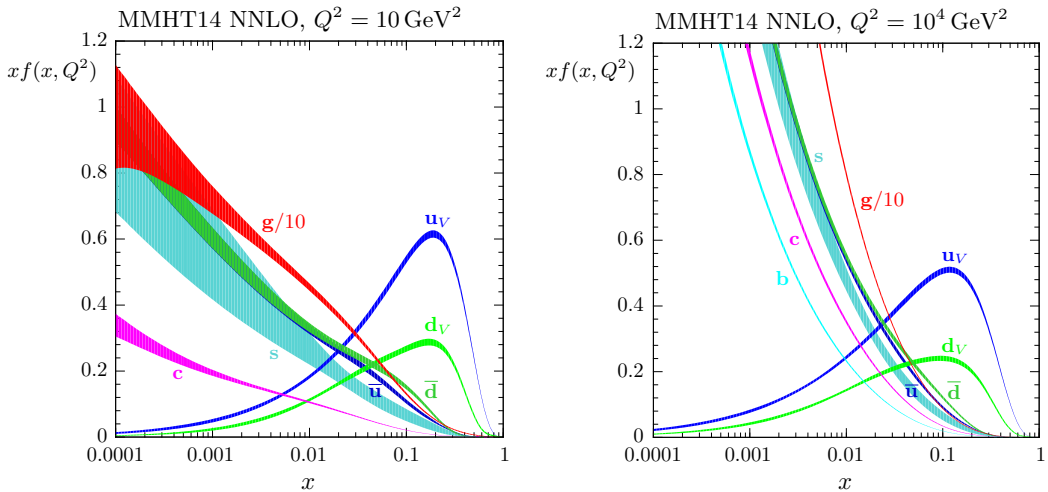


**Table 2.5:** MMHT2014 NNLO PDFs at  $Q^2 = 10$  GeV $^2$  and  $Q^2 = 10^4$  GeV $^2$ , with associated 68% confidence-level uncertainty bands [18].

One can note that as  $x$  increases the values of the PDF for the sea quarks and gluons will fall smoothly; this is because it is energetically unfavourable to emit a high momentum gluon or  $q\bar{q}$  pair. The fall in the PDFs with respect to  $x$  is particularly notable for the gluon which is the dominant contribution at large values of  $Q^2$ .

The PDFs of the valence quarks,  $u_v$  and  $d_v$ , have a peak value around  $x \sim \frac{1}{3}$ , and then fall off rapidly at higher  $x$ . If one considered the proton in the initial naive model of the proton then we find the PDFs of valence quarks as delta peaks at exactly  $\frac{1}{3}$  with amplitude of  $\frac{2}{3}$  and  $\frac{1}{3}$  for the  $u$  and  $d$  quark respectively; however, QCD interactions have smeared this

peak to what is observed.

### 2.2.3.4 Features of the Hadronic Cross-section

There are four important features that one can qualitatively describe about the dijet hadronic cross-section from the two factorised elements shown in Section 2.2.3.2 and 2.2.3.3. These important features will have significance when forming the di- $b$ -jet search analysis strategy in Chapters ??*Background estimation chapter* and ??*Event selection chapter*.

- **Large cross-section :**

The strong coupling constant  $\alpha_s$  is much larger than the other forces, meaning that the dijet cross-section is large. As a result dijet production through QCD is one of the most common events at hadron colliders and will be the strongly dominant background in any di- $b$ -jet search.

- **Behaviour with respect to  $m_{kl}$  :**

It can be seen that the hadronic cross-section causes a smooth and monotonically decreasing spectrum with respect to  $m_{kl}$  as a result of three factors. Firstly, the cross section has a  $1/m_{kl}$  term. Secondly, as shown in Section 2.2.1,  $\alpha_s$  will smoothly decrease with increasing  $Q$ , which in this case is correlated with  $m_{kl}$ . Finally, as  $m_{kl}$  increases then the momentum fraction of the proton,  $x$ , required to create the dijet event will also increase. As shown in Figure 2.5, the parton density functions are generally falling with respect to  $x$ , which will lead to falling behaviour in the hadronic cross-section.

- **Behaviour with respect to  $y^*$  :**

In all but one of the  $S(ij \rightarrow kl)$  terms shown in Table 2.4, we see that there is a  $1/\hat{t}$  term, which originates from the t-channel Feynman diagram. This term will become large when  $\cos \theta^* \rightarrow 1$  causing the dijet cross-section to peak at large values of  $y^*$ .

- **Flavour Preference:**

Table 2.4 shows that all the processes that produce heavy flavour quarks ( $c$  or  $b$ ), with the exception of  $q_1\bar{q}_1 \rightarrow q_2\bar{q}_2$  and  $gg \rightarrow q\bar{q}$ , require a heavy flavour quark to be one of the initial partons. However, Figure 2.5 shows the heavy flavour quarks are suppressed in the PDFs relative to the other partons. Therefore, dijet events will be dominated by jets initiated by gluons or light-quarks ( $u, d$  or  $s$ ).

Finally, it should be noted that the above description of the dijet cross-section is not a full description; I have only considered the tree-level diagrams, but one needs to consider higher-orders of QCD to give a complete description of dijet production. Related to that issue is the occurrence of initial state and final state radiation, known as ISR and FSR respectively. ISR is when an additional parton is radiated off the incoming parton and FSR is when an additional parton is radiated off the outgoing parton to form a separate jet. This can lead to additional jets in an event, creating a multi-jet event.

In addition, there is also the Underlying Event (UE) which effectively comprises of the remnants of the proton not used in the hard-scatter. The UE will mostly be hadronic activity and as a result can lead to additional jets in the event, again creating a multi-jet event.

#### 2.2.4 A Special Case: $t\bar{t}$

The top-quark is a special case when discussing the formation of jets from quarks, due to two properties of the top quark which are distinctive. Firstly, due to the large suppression of decays from the 3rd generation in the CKM matrix, the top quark decays to a  $b$ -quark and a  $W$ -boson with a branching ratio of close to 1. Secondly, the top quark is much heavier than the bottom quark meaning that the decay to a  $b$ -quark is very energetically favourable. Therefore, the top-quark decays on a shorter time-scale than parton shower process resulting in two separate objects; the  $W$ -boson and the hadronic jet.

As in dijet production,  $t\bar{t}$  pairs can be pair-produced in proton-proton collisions through QCD interactions. The two top quarks will decay into two  $W$ -bosons and two jets containing  $b$ -quarks. One mode of  $t\bar{t}$  decay is when one  $W$ -boson decays into a  $l^+ \nu_l$  pair and the other into a  $l^- \bar{\nu}_l$  pair. This is known as a di-lepton  $t\bar{t}$  event, a Feynman diagram showing an example of a di-lepton  $t\bar{t}$  event is shown in Figure 2.4<sup>8</sup>.

Di-lepton  $t\bar{t}$  forms a distinct experimental signature. In particular, the case of opposite flavour di-lepton  $t\bar{t}$ , where the two leptons have different flavours, is very distinct because this has been caused by two separate weak-decays which would typically be suppressed, but here the large mass of the top overcomes this suppression. In addition we have two jets formed from  $b$ -quarks, which can be observed. The distinct signature of di-lepton  $t\bar{t}$

---

<sup>8</sup>This figure shows the  $q\bar{q}$  mode of  $t\bar{t}$  production. It should be noted that the  $gg$  mode is the dominant at the LHC

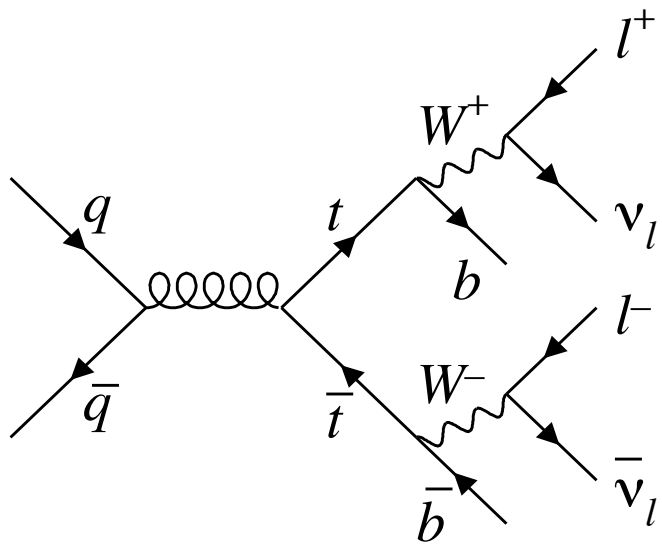


**Figure 2.4:** A Feynman diagram showing an example of a di-lepton  $t\bar{t}$  event [19].

events and the fact that the top-quark nearly always decays to a  $b$ -quark means that this decay topology is often used to obtain a pure sample of jets containing  $b$ -quarks, such as in Section 4.3.4 and 5.3.

## 2.3 Beyond the Standard Model

The preceding sections of this chapter described the Standard Model and some of its successes, such as the prediction of the Higgs boson and the ability to describe complex phenomena such as dijet production.

However, the Standard Model is known to be an incomplete picture of the universe; in this section I will discuss some of the key deficiencies of the Standard Model demonstrating that Beyond Standard Model (BSM) physics is required. I will then discuss some proposed BSM models that motivate the analyses shown in this thesis.

### 2.3.1 Motivations for Beyond the Standard Model Physics

The motivations for BSM physics listed in this section describe only a subset of deficiencies of the Standard Model, with a focus on the most important missing parts and those that motivate models searched for in this thesis.

#### 2.3.1.1 Gravity

When listing forces in Section 2.1.2, we made no reference to gravity. This is because our description of gravity, Einstein’s General Theory of Relativity, has not been successfully merged with the Standard Model in a so-called ‘Quantum Theory of Gravity’. It is a clear inadequacy of the Standard Model that there is no explanation of gravity

#### 2.3.1.2 Dark Matter

Astronomers are able to make observations of distant galaxies and stars to study their dynamics in terms of both Standard Model processes and, due to the large masses of galaxies, gravitational interactions. This has meant that astrophysicists have made a remarkable observation that 80% of the universe’s matter must be so-called ‘Dark Matter’ [20]. Dark Matter are particles not described by the Standard Model, so is clear evidence of Beyond Standard Model physics. It is known that Dark Matter must interact weakly with the Standard Model, otherwise we would have already observed it through interactions with Standard Model particles, and that Dark Matter must be massive, otherwise it would not interact through gravity.

The evidence for Dark Matter comes from many separate astronomical observations: such as studies of galaxy rotation curves, colliding clusters of galaxies known as bullet clusters, and the cosmic microwave background. A wider summary of the evidence for Dark Matter can be found here [21].

Furthermore, it is believed that the Dark Matter couples to the Standard Model; the evidence for such a statement stems from the observed relative abundance of Dark Matter particles in the universe. The most common method of explaining the abundance argues that in the early and hot universe Dark Matter and Standard Model particles freely interacted such that they were in thermal equilibrium. As the universe expanded and cooled this interaction was suppressed and the number density of Dark Matter was fixed at the value we observe today [22]. As a result this means that there may be some yet unknown mechanism that couples to both Dark Matter and Standard Model particles; this mechanism is referred to as a Dark Matter mediator.

### 2.3.1.3 Hierarchy Problem

The Hierarchy problem is the fact that the energy scale of electro-weak breaking, ( $M_{EW} \sim 100$  GeV), is much smaller than the energy scale of gravity, known as the Plank scale ( $M_{Plank} \sim 10^{19}$  GeV). This means that the energy scale of the Standard Model is very far from the energy scale of the next known interaction, gravity.

The Hierarchy problem leads to complications in theoretical calculations, such as the that of the Higgs boson mass. When calculating the Higgs boson mass one must consider radiative contributions from additional loop diagrams, similar to what was done for the gluon propagator in Section 2.2.1. However, these contributions are found to be of the order  $\delta m_H^2 \sim \frac{1}{16\pi^2} M_{Plank}^2$ , orders of magnitude larger than the observed mass of the Higgs boson. This means that some mechanism must either cancel the contributions or reduce their size. Whilst the free parameters of the Standard Model can be chosen such that these different contributions approximately cancel out, such fine-tuning of the parameters is hard to believe without some underlying explanation.

Instead, there are two solutions typically proposed to stabilise the effect of the loop corrections. Firstly, one can introduce BSM physics such that the Standard Model contributions

are cancelled by the BSM contributions. Secondly, one can introduce some BSM physics at a new energy scale such that the loop diagram contributions are cut off at  $\delta m_H^2 \sim \frac{1}{16\pi^2} M_{BSM}^2$ . If the BSM physics is on the TeV scale then this would reduce to size of the contributions to the scale of the Higgs boson's mass, giving some prior belief that new physics could be found at this energy scale.

### 2.3.1.4 Quarks Generational Structure

The quarks of the Standard Model have a well ordered generational symmetry. However the generational symmetry is not perfect; each generation is heavier than the previous one and within the generations quarks have different masses. In particular, the third generation of quarks is somewhat special; the top quark is much heavier than the bottom quark and is the heaviest particle of the Standard Model.

There is no good explanation of why there is generational structure in the Standard Model, why the mass hierarchy is unsymmetric or why the third generation has one quark with such a large mass. The generational structure could be a result of some underlying broken symmetry which forms a part of a deeper theory of Particle Physics. Any deeper theory explaining the generational structure could contain observable BSM particles, and, given the special nature of the third generation, the BSM particles could couple strongest with the third generation of quarks.

Unlike the case of Dark Matter, the generational structure of quarks and the special nature of the third generation is not concrete evidence of BSM physics. But it does mean that there are motivations to be particularly interested in searches for particles decaying to the third generation of quarks.

### 2.3.2 Beyond Standard Model Theories

The previous section discussed a list of deficiencies of the Standard Model, which makes us confident that Beyond the Standard Model physics must exist. This leads us to ask what the new theory of physics could be and, crucially for an experimentalist, how can one obtain evidence of such a theory.

Many proposed theories of BSM physics include the addition of a new particle and, in particular, the special nature of the third generation<sup>9</sup> means that some models of BSM predict new particles that preferentially decay to one or two  $b$ -quarks. Hence, the observation of such a resonance would provide evidence of BSM physics. Further to this, the Hierarchy Problem provides motivation to believe that any new physics may be found at the TeV scale.

Two such models that predict resonances with preferential decays to  $b$ -quarks are discussed below. These are used as ‘benchmark models’ in the analyses presented in this thesis, where a benchmark model is a plausible signal model that is used to form and optimise a search strategy.

#### 2.3.2.1 $Z'$ Boson

One of the most simple additions to the Standard model is that of a  $U(1)'$  gauge symmetry which would result in an additional spin-1 boson, known as the  $Z'$  boson. An additional  $U(1)'$  symmetry appears in many different BSM models and is therefore a well motivated BSM extension [23]. The  $Z'$  boson can decay to a pair of  $b$ -quarks, as shown in Figure 2.5.

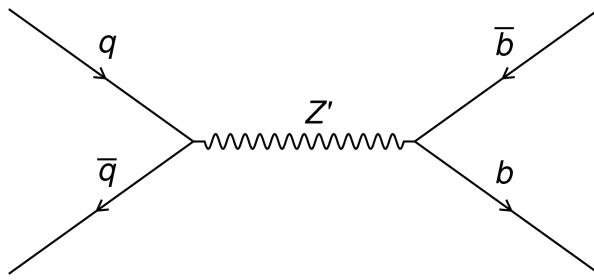


**Figure 2.5:** The leading-order Feynman diagram of the process  $q\bar{q} \rightarrow Z' \rightarrow b\bar{b}$ .

---

<sup>9</sup>Discussed in Section 2.3.1.4

In this thesis we will consider three different models predicting a  $Z'$  boson with different couplings. The first is known as the Sequential Standard Model (SSM)  $Z'$  in which the couplings of the new  $Z'$  boson are set to match those of the Standard Model, leading to universal coupling to all fermions. The strongest limits on the SSM  $Z'$  boson at the TeV scale are set by searching for a  $Z'$  boson decaying to lepton pairs [24]<sup>10</sup>. In addition, we also consider a leptophobic model where the  $Z'$  boson does not couple to the lepton sector but has universal coupling to each of the quarks [25], this model is therefore not strongly constrained by di-lepton searches.

In the final model considered the  $Z'$  boson acts as a Dark Matter mediator which can couple to both the Dark Matter sector and the Standard Model quark sector [26]; the motivation for such a model was discussed in Section 2.3.1.2. This model introduces an additional  $U(1)'$  symmetry and a Dirac fermion Dark Matter particle that only interacts through the new gauge group. The resulting  $Z'$  boson couples with the DM fermion and the Standard Model quark sector with coupling  $g_\chi$  and  $g_q$ , respectively, and is leptophobic so does not couple with the lepton sector.

It is worth noting in the models considered the  $Z'$  boson does not preferentially decay to  $b$ -quarks but rather with the same branching ratio as the other quarks. However, this can still be considered as preferential decay to  $b$ -quarks with respect to the dijet background, which is dominated by gluons and quarks from the first two generations, as discussed in Section 2.2.3. Furthermore, there exists  $Z'$  models that do not couple to all generations equally [27], such that a  $Z'$  boson preferentially decaying to  $b$ -quarks is possible.

### 2.3.2.2 Excited Third-Generation Quark

To explain the generational and mass structure of the quark sector, discussed in Section 2.3.1.4, quark compositeness models describe quarks, not as fundamental particles, but instead constructed of other fundamental particles. One consequence of quark compositeness models is the prediction of excited quarks,  $q^*$ , which can be observed as heavy resonances.

In particular we consider an excited 3rd generation quark, the  $b^*$  quark. The dominant

---

<sup>10</sup>This is due to the fact that a di-lepton signature is distinct to the large QCD dijet backgrounds produced in  $pp$  collisions

decay mode of a  $b^*$  quark is to  $bg$  with a branching ratio of 85% while the remaining decay modes are to  $Wt$ ,  $bZ$  and  $b\gamma$  with branching ratios of 10%, 4.5% and 0.5% respectively<sup>11</sup>. A Feynman diagram showing the dominant production and decay mode of a  $b^*$  quark is shown in Figure 2.6.

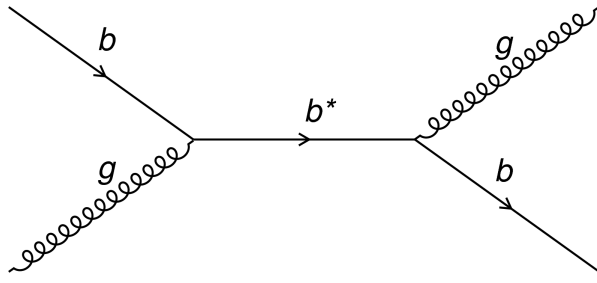


**Figure 2.6:** The leading-order Feynman diagram of the process  $bg \rightarrow b^* \rightarrow bg$

### 2.3.2.3 Model Independence

The two benchmark models demonstrate that searching for particles decaying to one or two  $b$ -quarks is well motivated. However, it is important to note that the prior belief in any specific model of BSM is small. This is because there are many BSM theories proposed and there is little evidence to prefer one model over another. In addition, one must also consider that the true theory may not have been anticipated, such that experiments might be able to see evidence of something truly unexpected.

Therefore, one should construct searches for BSM to be as model independent as possible, rather than optimising specifically for any one model in particular. In our case we want to search for any particle that is decaying to one or two  $b$ -quarks, in a way such we are sensitive to as many BSM theoretical models as possible and allow for the unexpected gifts that nature might throw up.

---

<sup>11</sup>Using the assumptions outlined in [28].

## Chapter 3

# The ATLAS Detector

### 3.1 The Large Hadron Collider

High-energy particle colliders have been an essential tool in high-energy physics research for over 50 years, with a rich history of discovering new particles as each generation of collider pushes the energy frontier; including the discovery of the Z and W bosons using the Super Proton Synchotron at CERN in 1983 [29, 30, 31, 32] and the discovery of the top-quark at the Tevatron in 1995 [33, 34].

The Large Hadron Collider (LHC) is the highest energy collider ever built, operated by the *Conseil Européen pour la Recherche Nucléaire (CERN)*. Lying in a tunnel 100 m beneath the Swiss/French border near Geneva, the LHC is a 27 km circumference ring of superconducting magnets and accelerating structures, which accelerate beams of protons to a maximum energy of 6.5 TeV. These proton beams are collided in four different locations on the LHC ring and around each collision point a different detector is constructed to observe these collisions; one such of these detectors is ATLAS.

#### 3.1.1 LHC running conditions in 2015 and 2016

Since May 2015 the LHC has been colliding bunches of protons at a center-of-mass energy of 13 TeV, the highest energy collisions ever obtained by a particle collider<sup>1</sup>. In 2015 and 2016 the LHC produced pp collisions with a bunch spacing of 25 ns<sup>2</sup> and an average number

---

<sup>1</sup>The period of data-taking from 2015 is known as Run-2.

<sup>2</sup>A small amount of data in 2015 was collected with a bunch spacing of 50 ns

of collisions per bunch-crossing ( $\langle \mu \rangle$ ) of 23.7. Figure 3.1 shows the total luminosity delivered by the LHC and recorded by ATLAS against date in 2015 and 2016, showing that a luminosity of  $39.5 \text{ fb}^{-1}$  was recorded by ATLAS in 2015 and 2016 combined [35].

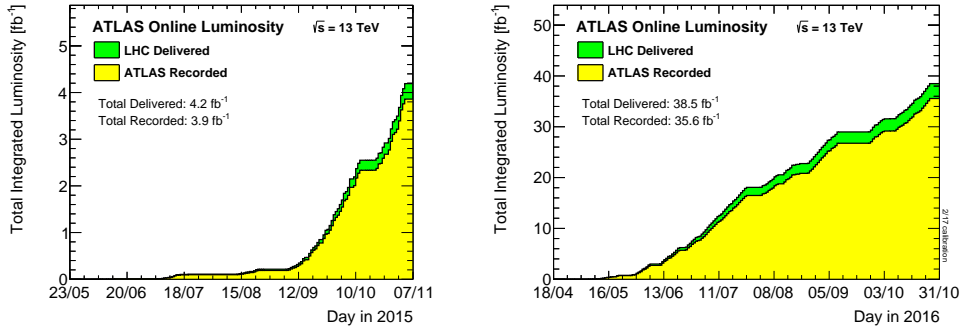


**Figure 3.1:** Cumulative luminosity versus time delivered to (green) and recorded by ATLAS (yellow) during stable beams for pp collisions at 13 TeV centre-of-mass energy in (a) 2015 and (b) 2016 [35].

## 3.2 ATLAS Detector Description

The ATLAS (**A** Toroidal **L**arge **H**adron **C**ollider **A**pparatuS) detector design, construction and performance has been described in detail previously [36, 37, 38], so what follows in this chapter is a general description of the detector with a focus on the needs of the analysis that is being presented. The ATLAS detector is effectively a large closed cylindrical detector, made up of four key components which sit in concentric rings around the interaction point, where the proton bunches collide. These components are the inner detector, calorimeters, muon spectrometer and the magnets; each of which are described in further detail below. This design is used as each sub-detector measures different quantities and interacts differently to the various range of particles that ATLAS is required to observe, meaning the ATLAS detector is able to identify and measure the key properties of particles that pass through its volume. Figure 3.2 shows a cut-away schematic of the detector and Figure 3.3 shows a slice of the detector in the plane perpendicular to the beam-pipe, overlaid are simplified illustrations how the detector can respond to a range of particles [39].

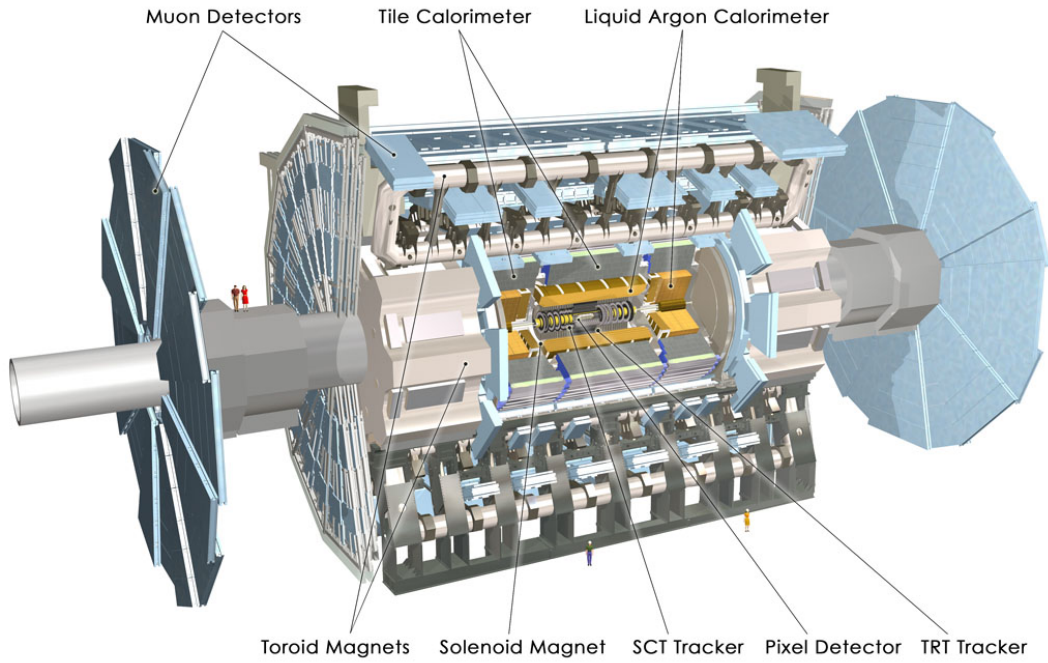


**Figure 3.2:** A cut-away schematic of the ATLAS detector [36].

### 3.2.1 ATLAS Co-ordinate System

Firstly, to describe the detail of the ATLAS detector there must be a description of the co-ordinate system that is used. ATLAS uses a right-handed coordinate system, in which the origin lies at the interaction point. The  $x$ -axis points to the centre of the LHC ring parallel to the surface of the earth, the  $y$ -axis points towards the surface of the earth and the  $z$ -axis runs along the beam-pipe, pointing anti-clockwise along the LHC beam-pipe. The azimuthal angle,  $\phi$ , is defined right-handedly around the  $z$ -axis starting at the  $x$ -axis.

The polar angle,  $\theta$ , is defined as the angle measured from the  $z$ -axis, such that along the  $z$ -axis corresponds to  $\theta = 0$  and anti-aligned with the  $z$ -axis corresponds to  $\theta = \pi$ . However, to define the angular direction with respect to the  $z$ -axis the ATLAS co-ordinate system uses pseudo-rapidity,  $\eta$ , instead of using  $\theta$ , for reasons that will be outlined below.  $\eta$  is defined as a function of  $\theta$ :

$$\eta = -\ln \left[ \tan \left( \frac{\theta}{2} \right) \right] \quad (3.1)$$

Thus,  $\eta = 0$  corresponds to a particle travelling perpendicular to the beam-pipe, where a positive value of  $\eta$  corresponds to a particle travelling with a tilt towards the  $z$ -axis. The quantity is called pseudo-rapidity as in the massless limit ( $\lim_{E \rightarrow |\vec{p}|}$ ) it can be shown that  $\eta$

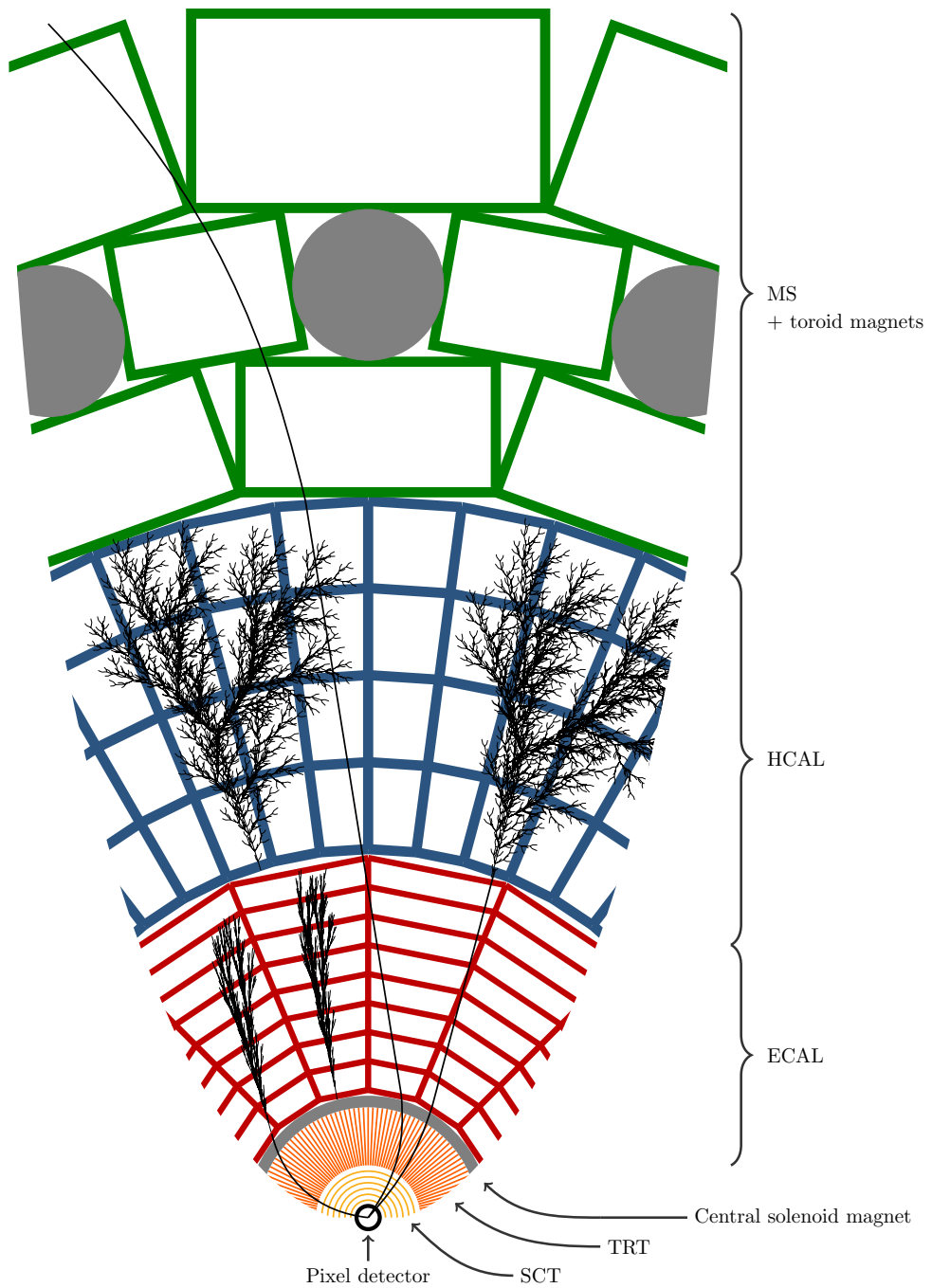


**Figure 3.3:** A visualisation of the ATLAS detector and the various sub-detectors. The view is taken as a slice in a plane perpendicular to the beam-pipe, showing the radial range from the beam-pipe to the edge of the detector. Overlaid are simplified illustrations of how various types of particles interact with the ATLAS detector; specifically from left to right the particles are an electron, a chargeless hadron (e.g. a neutron), a photon, a muon and a charged hadron (e.g. proton). The sub-detector components are not to scale [39].

converges to rapidity,  $y$ , where rapidity is defined as,

$$y = \frac{1}{2} \ln \left( \frac{E + p_z}{E - p_z} \right) \quad (3.2)$$

A key property of rapidity is that the differences in rapidity,  $\Delta y$ , are invariant against Lorentz boosts along the  $z$ -axis. Thus,  $\eta$  is the final variable chosen in the ATLAS co-ordinate system due to the relation of  $\eta$  with both  $\theta$  and  $y$  and the above mentioned property of  $\Delta y$ . One final quantity commonly used within ATLAS is the variable  $\Delta R$ , which is defined as

$$\Delta R = \sqrt{\Delta\eta^2 + \Delta\phi^2} \quad (3.3)$$

$\Delta R$  represents an angular separation between two vectors within the ATLAS co-ordinate system.

Now that we have discussed the ATLAS co-ordinate system, we can provide a description of the components of the ATLAS detector.

### 3.2.2 Inner Detector

The Inner Detector (ID), the innermost sub-detector on ATLAS, measures the trajectory of charged particles passing through the detector. The ID is constructed from many concentric layers of detector, and as a charged particle passes through the detector each of the layers provides a position measurement, known as a hit. Then using the hits from the many layers the trajectory of the particle can be determined; the measured trajectory is known as a track. The ID is immersed in a 2 T magnetic field which bends the particle's trajectories; from the sign and magnitude of the track's curvature the charge and momentum of the particle can be inferred. The ID is made of three main component parts; the pixel detector, the Semi-Conductor Tracker (SCT) and the Transition Radiation Tracker (TRT), as visualised in Figure 3.4. The ID consists of the barrel, which are made up of cylinders surrounding the beam-pipe to cover low absolute values of  $\eta$ , and the end-caps, which lie perpendicular to beam-pipe on either end of the barrel to cover large values of absolute  $\eta$ : here the description focuses on the barrel as this covers the  $\eta$  range considered by the analysis.

The innermost component of the ID is the silicon pixel detector; in the barrel this detector consists of 4 high-granularity layers of silicon based pixel modules surrounding

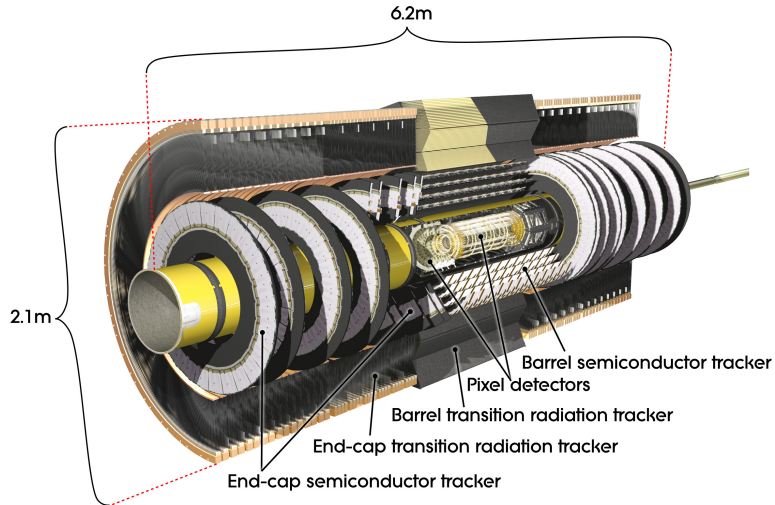


**Figure 3.4:** A cut-away schematic of the ATLAS Inner Detector (ID) [36].

the beam pipe, covering a range of  $-2.5 < \eta < 2.5$  and a radial distance of 33 mm to 122.5 mm [40, 41]. The high-granularity of the pixel layers, allows for high precision measurements, with an intrinsic resolution of approximately resolution of  $\sim 10\text{ }\mu\text{m}$  in  $R - \phi$  plane and  $\sim 115\text{ }\mu\text{m}$  in the z-direction.

Moving radial outwards the next component of the ID is the Semi-Conductor Tracker; which, in the barrel, comprises of 4 cylindrical layers of silicon micro-strips covering a range of  $-2.5 < \eta < 2.5$  and a radial distance of 299 mm to 514 mm. The SCT has an intrinsic resolution of  $\sim 17\text{ }\mu\text{m}$  in  $R - \phi$  plane and  $\sim 580\text{ }\mu\text{m}$  in the z-direction.

The outermost component of the ID is the Transition Radiation Tracker (TRT) constructed of many 4 mm radius tubes filled with xenon. As a charged particle passes through the gas, it will cause ionisation allowing a measurement of its position using drift-time. In the barrel, each tube provides a measurement in the  $R - \phi$  plane with an intrinsic resolution of  $130\text{ }\mu\text{m}$  and the TRT will typically provide 36 hits per track. In addition to a position measurement, due to the choice of the material between the tubes, a particle passing through the detector will radiate photons at an intensity inversely correlated to the mass of that particle, providing additional information for particle identification.

The trajectory, momentum and charge measurements provided by the Inner Detector are essential for particle identification in ATLAS. In particular, the high precision measurements close to the beam-line allow for vertex reconstruction, which is essential for

identification of tracks coming from B or C hadrons, and hence the identification of  $b$ -jets. This process, known as  $b$ -tagging, is discussed further in Section 4.3(*object definition and selection*) and is important within the context of this analysis.

### 3.2.3 Calorimeters

The ATLAS calorimeter, located on the outside of the magnet solenoid surrounding the ID, is designed to provide an energy measurement of the traversing particles. Accurate energy measurements are essential for a good resolution of the mediator mass reconstructed from its decay products, which is important within the context of the analysis being presented in this thesis.

The calorimeter at ATLAS is made up of two different systems that are built in concentric rings; the inner-most is the Electromagnetic Calorimeter system (ECAL), which is used to measure electromagnetic objects such as photons and electrons. Outside of that is the Hadronic Calorimeter system (HCAL), designed to provide an energy measurement of hadronic material. The HCAL is built from the Tile and Hadronic Endcap calorimeters. Both the ECAL and HCAL have barrel and end-cap components to make energy measurements at a large range of  $\eta$  values. Figure 3.5 shows a cut-away of the ATLAS calorimeter.

Below I provide a more detailed description of the calorimeter components; however, the principle behind each detector is common so is described first. The calorimeters at ATLAS are sampling calorimeters, which means they consist of alternating layers of absorber and active material. The role of the absorber layer is to force the particle, whose energy we want to measure, to emit secondary particles. These secondary particles will again emit further particles and so on meaning a “particle cascade” is formed. The role of the active material layer is to measure the energy of the many resulting particles from the cascade, known as the cascade particles. The ATLAS detector is built such that the initial particle will cascade within the volume of the calorimeter system and then, from a measurement of the energy of all the cascade particles, the energy of the initial particle can be inferred.

#### 3.2.3.1 Electromagnetic Calorimeter (ECAL)

For the electromagnetic interaction, at energies  $\sim \geq 1$  GeV the particle cascade process is mainly caused by two processes; bremsstrahlung, ( $e^{+/-} \rightarrow e^{+/-} + \gamma$ ) and pair production

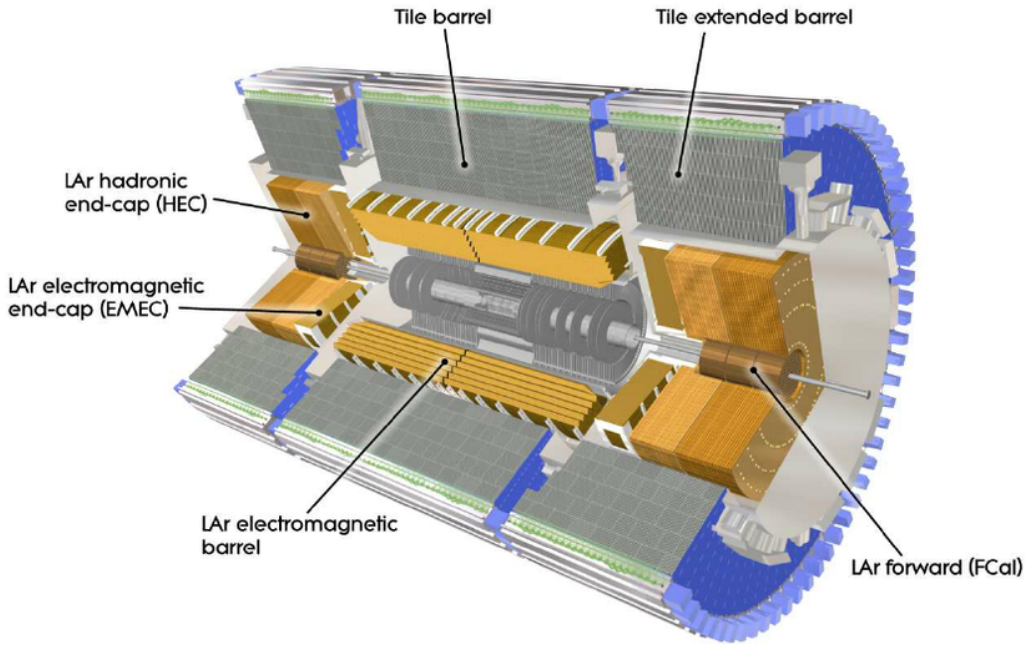


**Figure 3.5:** A cut-away schematic of the ATLAS calorimeter system [36].

$(\gamma \rightarrow e^+ + e^-)$ . The electromagnetic calorimeter at ATLAS is known as the Liquid Argon (LAr) calorimeter. The absorber material used in the LAr calorimeter is lead, due to its large density of charged particles (high Z) which increases the rate of the cascade processes. The active material is liquid argon; when a cascade particle passes through the liquid argon it causes ionisation, and the released electrons are captured using an electric field. The number of released electrons is proportional to the energy of the cascade particle, meaning that the energy of the cascade particle can be measured.

As discussed above the LAr is split up into two sections; the barrel section covers a region of  $|\eta| < 1.475$  and two end-cap components cover  $1.375 < |\eta| < 3.2$ . The depth of an electromagnetic calorimeter is often expressed in terms of the radiation length,  $X_0$ , which is the distance that an electron's energy reduces by a factor of  $e^{-1}$  through bremsstrahlung, or 7/9 of the mean free path for a photon to pair produce electrons. It is worth noting that this quantity is strongly material dependant; a high-Z material, such as lead, has a shorter  $X_0$ . The LAr calorimeter has a depth of  $> 22 X_0$  in the barrel and  $> 24 X_0$  in the end-caps, meaning that almost all of the particle shower from a high-energy photon or electron can be contained within electromagnetic calorimeter.

### 3.2.3.2 Hadronic Calorimeter (HCAL)

If a particle can also interact through strong interactions, such as the components of a hadronic jet, then the particle cascade is a more complicated process. A hadronic cascade processes is dominated by processes such as ionisation, nuclear spallation and neutron generation [42, 11]. For a chargeless hadron, for example a neutron, strong processes, such as spallation, are the only processes that contribute to its cascade. During these hadronic cascade processes many  $\pi_0$  mesons are made, which can decay to a pair of photons and thus form electromagnetic cascade as described above.

For hadronic interactions, the size of detector is measured by the interaction length,  $\lambda$ , defined as the distance required to reduce the number of relativistic hadrons by  $e^{-1}$ . This means that by the end of the LAr calorimeter there is  $2.3 \lambda$  of active material in the barrel, so the full hadronic shower cannot be captured by the LAr calorimeter alone. For a full measurement of the hadronic energy, the Hadronic Calorimeter system (HCAL) is required.

The Tile Calorimeter is constructed from absorber layers of steel and active material layers of scintillating tiles, and has a depth of  $7.4 \lambda$ , meaning the majority of the hadronic shower can be captured by either the LAr calorimeter or the Tile calorimeter. The Tile Calorimeter is split up into the barrel and the extended barrel components; the barrel covers the region  $|\eta| < 1.0$  and the extended barrel covers the region  $0.8 < |\eta| < 1.7$ .

To cover the more forward regions there are two more calorimeter detectors. The Hadronic Endcap Calorimeter (HEC) is housed in two large wheels at either end of the ATLAS detector and covers a region of  $1.5 < \eta < 3.2$ . The HEC is a sampling calorimeter built using copper as the absorber layers and liquid argon as the active material and has a depth of  $\sim 12 \lambda$ . In addition the Forward Calorimeter (FCAL) covers the very forward region of  $3.1 < \eta < 4.9$ , which is outside the range considered within this analysis. It is constructed from absorber layers of copper (for EM interactions) and tungsten (for hadronic interactions) with liquid argon for the active material layers.

Table 3.1 shows the key parameters of the ATLAS calorimeter system, including the ECAL and HCAL. The table outlines the coverage in  $\eta$ , the granularity in  $\eta$ - $\phi$  space and the number of readouts of each component of the ATLAS calorimeter system.

		<b>Barrel</b>		<b>End-cap</b>			
		<b>EM calorimeter</b>					
		Number of layers and $ \eta $ coverage					
Presampler	1		$ \eta  < 1.52$	1	$1.5 <  \eta  < 1.8$		
Calorimeter	3		$ \eta  < 1.35$	2	$1.375 <  \eta  < 1.5$		
	2		$1.35 <  \eta  < 1.475$	3	$1.5 <  \eta  < 2.5$		
		Granularity $\Delta\eta \times \Delta\phi$ versus $ \eta $					
Presampler	$0.025 \times 0.1$		$ \eta  < 1.52$	$0.025 \times 0.1$	$1.5 <  \eta  < 1.8$		
Calorimeter 1st layer	$0.025/8 \times 0.1$		$ \eta  < 1.40$	$0.050 \times 0.1$	$1.375 <  \eta  < 1.425$		
	$0.025 \times 0.025$		$1.40 <  \eta  < 1.475$	$0.025 \times 0.1$	$1.425 <  \eta  < 1.5$		
				$0.025/8 \times 0.1$	$1.5 <  \eta  < 1.8$		
				$0.025/6 \times 0.1$	$1.8 <  \eta  < 2.0$		
				$0.025/4 \times 0.1$	$2.0 <  \eta  < 2.4$		
				$0.025 \times 0.1$	$2.4 <  \eta  < 2.5$		
				$0.1 \times 0.1$	$2.5 <  \eta  < 3.2$		
Calorimeter 2nd layer	$0.025 \times 0.025$		$ \eta  < 1.40$	$0.050 \times 0.025$	$1.375 <  \eta  < 1.425$		
	$0.075 \times 0.025$		$1.40 <  \eta  < 1.475$	$0.025 \times 0.025$	$1.425 <  \eta  < 2.5$		
Calorimeter 3rd layer	$0.050 \times 0.025$		$ \eta  < 1.35$	$0.050 \times 0.025$	$1.5 <  \eta  < 2.5$		
		Number of readout channels					
Presampler	7808			1536 (both sides)			
Calorimeter	101760			62208 (both sides)			
<b>LAr hadronic end-cap</b>							
$ \eta $ coverage				$1.5 <  \eta  < 3.2$			
Number of layers				4			
Granularity $\Delta\eta \times \Delta\phi$				$0.1 \times 0.1$	$1.5 <  \eta  < 2.5$		
				$0.2 \times 0.2$	$2.5 <  \eta  < 3.2$		
Readout channels				5632 (both sides)			
<b>LAr forward calorimeter</b>							
$ \eta $ coverage				$3.1 <  \eta  < 4.9$			
Number of layers				3			
Granularity $\Delta x \times \Delta y$ (cm)				FCal1: $3.0 \times 2.6$ FCal1: ~ four times finer	$3.15 <  \eta  < 4.30$ $3.10 <  \eta  < 3.15,$ $4.30 <  \eta  < 4.83$		
				FCal2: $3.3 \times 4.2$ FCal2: ~ four times finer	$3.24 <  \eta  < 4.50$ $3.20 <  \eta  < 3.24,$ $4.50 <  \eta  < 4.81$		
				FCal3: $5.4 \times 4.7$ FCal3: ~ four times finer	$3.32 <  \eta  < 4.60$ $3.29 <  \eta  < 3.32,$ $4.60 <  \eta  < 4.75$		
Readout channels				3524 (both sides)			
<b>Scintillator tile calorimeter</b>							
	Barrel			Extended barrel			
$ \eta $ coverage	$ \eta  < 1.0$			$0.8 <  \eta  < 1.7$			
Number of layers	3			3			
Granularity $\Delta\eta \times \Delta\phi$	$0.1 \times 0.1$			$0.1 \times 0.1$			
Last layer	$0.2 \times 0.1$			$0.2 \times 0.1$			
Readout channels	5760			4092 (both sides)			

**Table 3.1:** The key spatial coverage, granularity and readout parameters of the ATLAS calorimeter [36].

Another important point about the ATLAS calorimeter is that it is a non-compensating calorimeter; that is to say that the response of the detector to an electromagnetic particle (such as an electron) is larger than the response of a hadronic particle (for example a pion). The reason for this is some energy is lost in hadronic cascade process; mainly due to

the energy required to release nucleons from calorimeter nuclei during spallation, but also from the recoil energy given to the calorimeter nuclei and neutrinos created during strong processes that can escape the calorimeter [43, 44]. To account for the fact that the ATLAS calorimeter is non-compensation, calorimeters are calibrated to the EM-scale, which means that the initial energy measurement of a calorimeter assumes that the particle EM-interacting. Then for a hadronic object a jet energy scale correction is applied in the jet calibration processs, which is described further in Section 4.2.3.

### 3.2.4 Muon Spectrometer

The only standard model particle visible to ATLAS which can pass through the calorimeter is the muon; hence to identify and obtain the momentum of muons an additional detector, the Muon Spectrometer (MS), is used. The MS is a detector which surrounds the hadronic calorimeter, measuring the momentum of muons by observing the curvature of their trajectories in magnetic fields. Trajectories are determined using muon position measurements from multiple layers of detectors, analogous to what has been described for the inner detector.

In the barrel region ( $|\eta| < 1.4$ ) the large barrel toroid provides the magnetic field, in the end-cap region ( $1.6 < |\eta| < 2.7$ ) the two smaller end-cap magnets provide the magnetic field and finally in the transition region ( $1.4 < |\eta| < 1.6$ ) both sets of magnets contribute to the magnetic field. A further description of the magnets used in ATLAS is found in the next section.

Muon chambers are the detectors tasked with providing the muon position measurements required to reconstruct muon tracks. The muon chambers come in two types; trigger and precision. The trigger muon chambers provide a quick position measurement in 3-dimensions which can be used to identify muons tracks in the trigger. The trigger muon chambers cover a range  $|\eta| < 2.0$ ; consisting of Resistive Plate Chambers (RPCs) in the barrel and Thin Gap Chambers (TGCs) in the end-cap regions. The precision muon chambers provide a precise measurement of the muon position co-ordinates in the  $R - z$  plane, the plane in which track curvature occurs in the muon spectrometer, allowing for precise measurements of the muon track- $p_T$ . In the barrel region, precision muon chambers are arranged in three concentric cylindrical layers of chambers formed around the beam-pipe,

whilst in the transition and end-cap regions there are three layers of chambers either side of the barrel lying in disks perpendicular to the beam-pipe. In the region  $|\eta| < 2.0$ , the precision muon chambers are made from Monitored Drift Tubes (MDTs), whilst at large pseudo-rapidities ( $2.0 < |\eta| < 2.7$ ), Cathode Strip Chambers (CSCs) are used.

There is an additional use of the muon spectrometer that relates to high-energy jets. Whilst for most jets their shower is fully contained within the calorimeter there are some jets, particularly at high- $p_T$ , where a non-negligible fraction of energy from the shower goes beyond the calorimeter. This effect, known as ‘punch-through’, is accounted for using energy deposits in the muon spectrometer.

### 3.2.5 Magnets

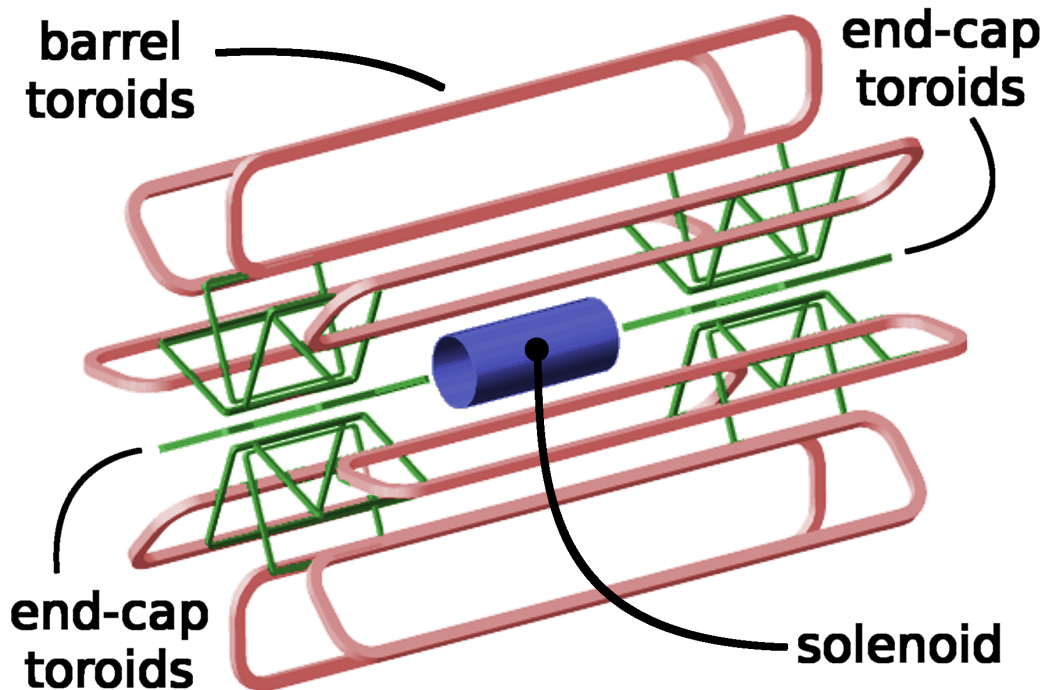


**Figure 3.6:** The layout of the ATLAS magnets [45].

In ATLAS magnetic fields are important for obtaining the momentum and charge of particles from their observed trajectories in the ID and Muon Spectrometer. ATLAS is made up of four large superconducting magnets; the inner solenoid which surrounds the inner detector and provides a 2 T magnetic field within the ID. The barrel toroid magnet provides a magnetic field of up to 2.5 T in the central regions of the muon spectrometer

and the two end-cap toroid magnets which produce a magnetic field of up to 3.5 T in the forward regions of the MS. Figure 3.6 shows the layout of the magnets in ATLAS [45].

### 3.3 Trigger

In 2015 and 2016, the LHC has been colliding proton beams with a spacing of 25 ns, meaning that the ATLAS experiment has been taking data at a rate of 40 MHz. However, due to the large computing resources required to process and store each event, it is not possible to record all this data for use in an analysis. To resolve this problem, the ATLAS experiment uses a trigger system to reduce the event rate by selecting the events of interest that contain high- $p_T$  physics objects, which indicate that a hard scatter has occurred in that event.

The ATLAS trigger-system has two levels; the first level trigger (L1) and the higher level trigger (HLT) [46]. Figure 3.7 shows a schematic outlining the trigger used in Run-2 [47].

The first level trigger (L1) is hardware based which reduces the rate from 40 MHz to 100 kHz within a time window of 2.2  $\mu$ s. The L1 trigger uses custom electronics to rapidly process information directly from the calorimeter and the muon spectrometer, searching for high- $p_T$  muon tracks and large calorimeter deposits. The information is then passed to the central trigger which uses a set of pre-defined conditions to decide if a L1 trigger accept is given and thus events are passed on to the next step of triggering. At the same time Regions of Interests (ROIs) are constructed around the objects that have fired the L1 trigger, which are passed on to the HLT.

The next step is the HLT, a software based trigger, which further reduces the event rate to 1 kHz within a time window of 0.2 s. The HLT uses the information from the full detector to perform a more complete reconstruction of the physics objects within the event, the most time consuming reconstruction algorithms only being run only within the ROIs taken from L1. The more complex event analysis allowed within the software-based trigger includes track reconstruction and therefore allows for  $b$ -jet identification. If the content of the event reconstruction passes a pre-set criteria, a HLT accept is issued meaning that the events are passed on for processing and storage.

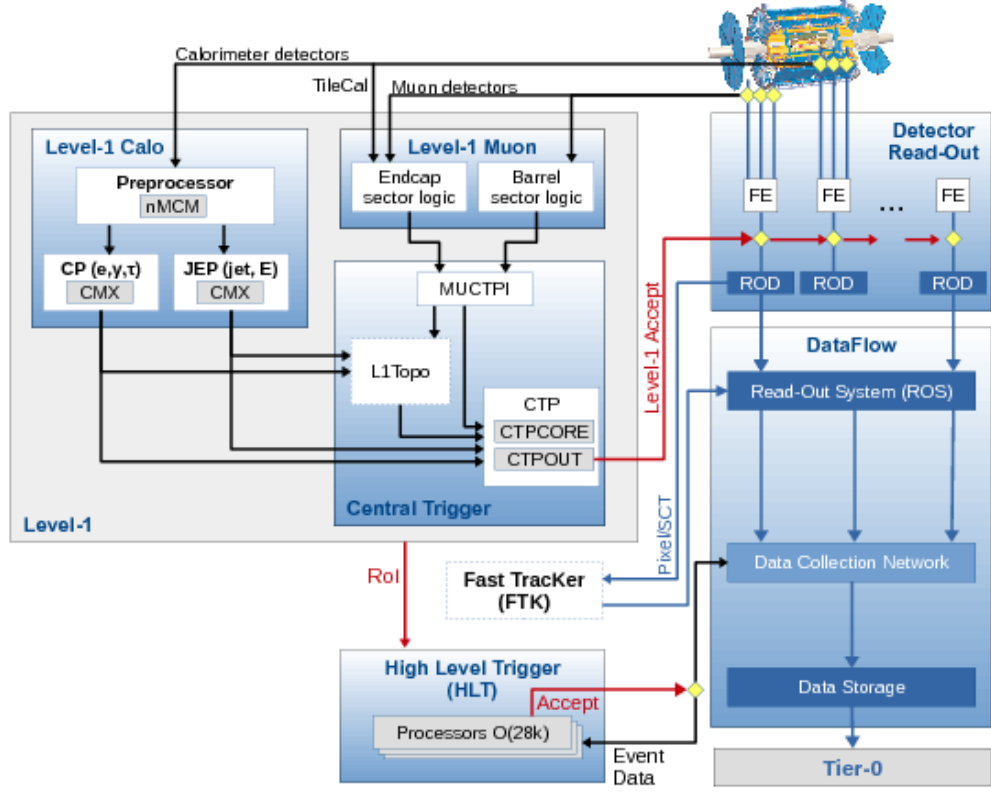


**Figure 3.7:** A schematic of the ATLAS trigger and data-acquisition system in Run-2, with a focus on the components required for triggering [46].

A further description of triggers used in the analysis, with a particular focus on the  $b$ -jet trigger performance can be found in ??(*b*-jet trigger chapter).

## Chapter 4

# Object Definition and Reconstruction

The previous chapter described how the ATLAS detector collects information on final state particles produced in  $pp$  collisions in the form of, for example, hits in the Inner Detector and Muon Spectrometer or energy deposits in the calorimeter. This chapter defines physics objects, which are observables that allow us to study the hard-scatter processes and form the basis of the analyses in future chapters. This chapter will describe how, using the information provided by the ATLAS detector, each physics object is identified and their 4-momentums and trajectories reconstructed.

Specifically this chapter will focus on physics objects important to the analyses in this thesis: tracks are described in Section 4.1, jets in Section 4.2,  $b$ -jets in Section 4.3, and electrons and muons in Section 4.4. Finally, Section 4.5 will briefly describe some further physics objects widely used in the ATLAS physics program outside of the analyses being presented here.

### 4.1 Tracks

The ATLAS detector is able to reconstruct the trajectory of charged particles produced in the proton-proton collision as they pass through the Inner Detector; the reconstructed trajectories are known as tracks. Track reconstruction is essential in a number of important areas of ATLAS analyses: for example; primary vertex reconstruction, identification of  $b$ -jets (Section 4.3) and the identification and reconstruction of electrons and muons (Section 4.4).

Track reconstruction uses hits from the Pixel detector, SCT and TRT which are de-

scribed in Section 3.2.2. The track reconstruction is performed using an ‘inside-out’ approach, which entails using the higher precision Pixel and SCT hits initially before adding in the TRT hits to improve track quality. The tracking reconstruction procedure [48] follows these steps:

- **Clustering:**<sup>1</sup> Neighbouring hits in a layer of the Pixel or SCT detector are converted into a 3D ‘space-point’ that represents the point where the charged particle traversed the active material of the ID. In the Pixel detector one cluster of hits can form a space-point, whilst in the SCT hits from both sides of a strip layer are required to create a 3D space-point.
- **Track Seeding:** Track seeds are formed from three space-points in consecutive layers of the Inner Detector that are consistent with the trajectory of a particle with  $p_T > 500$  MeV.
- **Track Candidates:** From the track seeds, track candidates are built by iteratively adding space-points from the remaining Pixel and SCT detector layers using an combinatorial Kalman filter [49]. There can be multiple track candidates per seed.
- **Track selection / Ambiguity resolving:** Each track candidate is assigned a ‘track-score’ that is based a number of variables of the track candidate; the  $p_T$ ,  $\eta$ ,  $\chi^2$  fit and the hit pattern. The hit pattern refers to the number of Pixel or SCT hits, the number of holes (missing hits where one was expected) and the quality of the hits. Track candidates must also pass some track quality requirements, that are similarly based on the track candidate’s  $p_T$ ,  $\eta$  and the hit pattern. The self-consistent set of track candidates that have the highest ‘track-score’ and that pass track quality requirements are then selected. Exact details of the track-scoring, track requirements and selection algorithm is described in [48].
- **Add TRT Information:** Track candidates from the previous step are extrapolated into the TRT and all hits within 10 mm are added. The track candidates are then refitted using Pixel, SCT and TRT hits to make use of the full tracking detector.

The outputs of the above track reconstruction process will be referred to as tracks in the remainder of this thesis. Also it is important to note that, as discussed in Section 3.2.2, the tracks are curved by a known magnetic field in the Inner Detector, therefore the tracks contain information on the charge and the momentum of the particles whose trajectory they are describing.

---

<sup>1</sup>In the associated reference this step is referred to as ‘clusterization’, but here I will use clustering for consistency with the English language.

## 4.2 Jets

If a collision results in a free quark or gluon in its final state then a stream of high-energy hadrons is created, which is known as a hadronic jet. The underlying processes in hadronic jet formation can be summarised as follows; firstly the free quark/gluon will radiate additional gluons and quarks in a process known as the parton shower, these gluons and quarks will then undergo hadronisation to form hadrons which are the constituents of the hadronic jet. A more detailed description of the parton shower and hadronisation process can be found in Section [QCD theory description] Not written yet LM fix. The components of the hadronic jet deposit energy in the cells of the ATLAS calorimeter, through the processes described in Section 3.2.3, such that the ATLAS calorimeter has an energy and positional measurement of the components of the hadronic jet. The process of parton shower, hadronisation and energy deposition in the calorimeter, as described above, is illustrated in Figure 4.1.

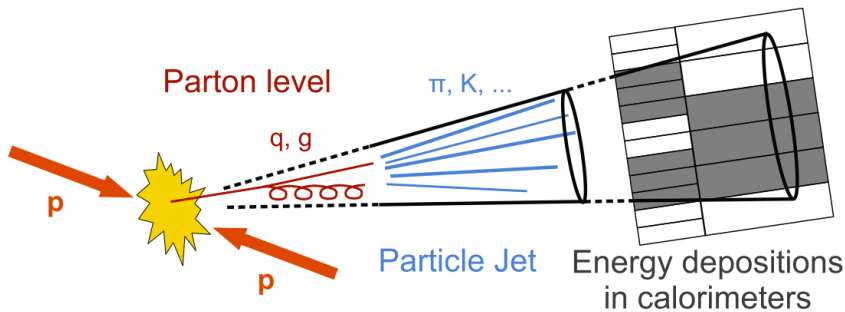


**Figure 4.1:** A schematic illustrating the formation of hadronic jets and the resulting observed energy deposits in the calorimeter system [50].

This section contains a description of the procedure utilised by ATLAS to go from energy deposits in calorimeter cells to well defined and calibrated hadronic jets. This procedure can be split up into three separate steps that are described in the following sections; firstly topoclusters are formed as described in Section 4.2.1, then jets are formed from topoclusters using reclustering algorithms as described in Section 4.2.2 and finally Section 4.2.3 and Section 4.2.4 describes how the jets are calibrated and the relevant jet energy uncertainties are derived.

In this section the formation of hadronic jets constructed from calorimeter cells is

described, as this is the only jet object used in the context of the analyses presented in this thesis. However, it is worth noting, that there are other types of jets used at ATLAS; for example hadronic jets can also be constructed from tracks formed in the Inner Detector, a technique that has been useful in dense environments [51].

### 4.2.1 Hadronic Topocluster Reconstruction

The first step of jet building at ATLAS is the formation of 3D clusters, known as topoclusters, from groups of energy deposits in neighbouring calorimeter cells [52]. The calorimeter cells can be from either the EM or hadronic calorimeter systems, which have a granularity given in Table 3.1. The algorithm employed makes use of the variable “cell signal significance” defined as,

$$S_{\text{cell}} = \frac{E_{\text{cell}}}{\sigma_{\text{noise,cell}}} \quad (4.1)$$

where  $E_{\text{cell}}$  is the energy deposited in a cell and  $\sigma_{\text{noise,cell}}$  is the uncertainty due to noise in that cell. The sources of noise in a calorimeter cell are described in Section **LM fix, need to have a noise section somewhere....**. A large value of  $S_{\text{cell}}$  ( $> 1$ ) indicates that the energy deposit is likely due to a particle depositing energy in the calorimeter rather than noise within the calorimeter.

Using the value of  $S_{\text{cell}}$ , each calorimeter cell is labelled as follows

- If  $|S_{\text{cell}}| > 4$ : the cell is labelled a **seed** cell.
- If  $|S_{\text{cell}}| > 2$ : the cell is labelled a **growth** cell.
- If  $|S_{\text{cell}}| > 0$ : the cell is labelled a **boundary** cell.

Then the algorithms builds topoclusters as in the following steps,

1. A seed cell forms the centre of a new topocluster.
2. Neighbouring seed cells are added together to form one topocluster seed.
3. Then, growth cells neighbouring the topocluster are added.
4. Finally, boundary cells neighbouring the topocluster are added.

Figure 4.2 illustrates an example of where the algorithm would form a topocluster and an example where it wouldn’t.

The topoclusters are treated as massless objects, such that the four-momentum of each deposit can be calculated using the sum of energy deposited in the topoclusters and the  $\eta - \phi$  position of the topocluster. The constructed topoclusters and their four-momentums are then used as the inputs to the next step of jet reconstruction.

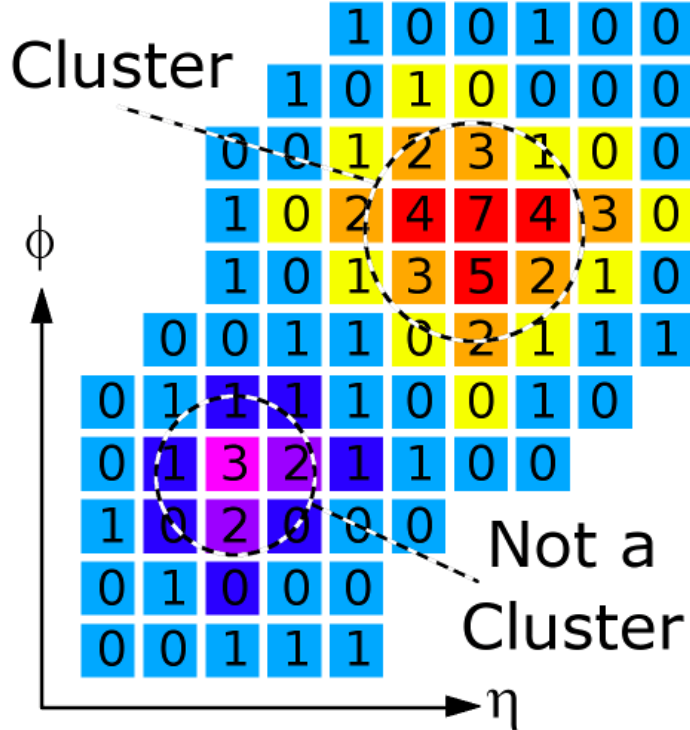


**Figure 4.2:** A schematic illustrating the algorithm used to form a topocluster. The numbers on the grid represent  $|S_{\text{cell}}|$  and the colours represent the cell label [45].

### 4.2.2 Jet Reconstruction

The next step in the process is to form jets from the topoclusters described in the previous section. To do this a jet reconstruction algorithm is defined, that uses the location and energy of the topoclusters in an event to form a set of jets. Each jet formed by the algorithm has a well defined four-momentum and set of constituents. Jet reconstruction algorithms are used to define jets as this means that jets are experimentally well-defined model-independent observables, which is required if measurements using jets are to be re-usable by the wider particle physics community. A detailed discussion of jet reconstruction algorithms and their related issues is found in [53]; as such this section provides a summary relevant to the analyses being presented in this thesis.

ATLAS analyses use a type of jet reconstruction algorithms known as sequential recombination algorithms, which selectively add together the calorimeter topoclusters to form the jet; these are specifically the  $k_t$ , anti- $k_t$  and Cambridge-Aachen (CA) algorithms.

The three algorithms use a set of four-momentums (clusters), which are initially the topoclusters formed in the calorimeter. One then introduces an inter-jet distance between clusters  $i$  and  $j$  defined as,

$$d_{ij} = \min[(p_{Ti})^a, (p_{Tj})^a] \left( \frac{\Delta R_{ij}}{R} \right)^2, \quad \Delta R_{ij} = \sqrt{(y_i - y_j)^2 + (\phi_i - \phi_j)^2} \quad (4.2)$$

and a particle-beam distance for cluster  $i$  defined as,

$$d_{iB} = (p_{Ti})^a \quad (4.3)$$

where  $y$  is rapidity (as defined in Section 3.2.1),  $\phi$  is azimuthal angle,  $p_T$  is transverse momentum (component of momentum perpendicular to the beam-pipe of colliding particles) and  $p_z$  is the component of momentum that is parallel to the beam-pipe of colliding particles.  $R$  is the jet width parameter, a free parameter of the algorithm. The parameter  $a$  in Eq. (4.2) and (4.3) takes the value  $a = 2$  for the  $k_t$  algorithm,  $a = -2$  for the anti- $k_t$  algorithm and  $a = 0$  for the Cambridge-Aachen algorithm.

The inter-jet and particle-beam distances are not physical distances as such, but can instead be thought of as dimensionful measures of how likely it is that clusters  $i$  and  $j$  represent clusters caused by hadrons from the same jet. If the inter-jet distance for a pair of clusters is smaller than the particle-beam distances for the two clusters ( $d_{ij} < d_{iB}$ ) then it is likely that the two clusters are from the same jet. In contrast, if  $d_{ij} > d_{iB}$  then it is unlikely that the two clusters are from the same jet.

The algorithm then proceeds using the following steps:

1. Calculate  $d_{ij}$  and  $d_{iB}$  for all combinations of clusters.
2. Find the minimum of the  $d_{ij}$  and  $d_{iB}$ .
3. If the minimum is a  $d_{ij}$  combine cluster  $i$  and  $j$  to form a new cluster and return to step 1.
4. If the minimum is a  $d_{iB}$  then call cluster  $i$  a final-state jet, remove it from the set and

return to step 1.

5. Stop when all clusters have been declared as jets.

The final jet has a four-momentum equal to the addition of all the topoclusters assigned to that jet. It can now be seen that the jet width parameter,  $R$ , effectively gives the scale of the width of a reconstructed jet. This is because when  $\Delta R_{ij} > R$  for a pair of clusters,  $d_{iB} < d_{ij}$  for the cluster with the smaller value of  $p_T$ , and thus the algorithm will not merge the two clusters.

The sequential reclustering algorithms described above are used as they satisfy two important theoretically motivated criteria: infrared and collinear safety. Infrared safety requires that the jet reconstruction algorithm result should be invariant against soft gluon emission <sup>2</sup> and collinear safety requires that the jet reconstruction algorithm result should be invariant against a parton splitting into two partons with small angular separation. These conditions are desirable as if the jet reconstruction algorithm is infrared or collinear unsafe, two different sets of jets could be formed from identical hard-scatter processes due to an additional emission process in the parton shower. The sequential reclustering algorithms described above are infrared and collinear safe. <sup>3</sup>.

Anti- $k_T$  is the jet reconstruction algorithm used for the analyses being presented in this thesis, which is typical of analyses at ATLAS. This is because the anti- $k_T$  algorithm provides regular jet shapes around the centre of the jet, due to the fact that the algorithm reconstructs the high- $p_T$  core of the jets first and then adds in the lower  $p_T$  suburbs in later steps. Figure 4.3 shows the jets formed by the Cambridge-Aachen,  $k_T$  and anti- $k_T$  algorithm using the same set of input clusters; this illustrates that anti- $k_T$  algorithm creates more regular jet shapes than the other sequential-reclustering algorithms. Further to this, the value of the jet width parameter is chosen as  $R=0.4$ , which is consistent with the values suggested for gluon/quark jets in Section 5 of [53] and is the standard value used in ATLAS analyses.

---

<sup>2</sup>Soft means a low momentum

<sup>3</sup>Cone-based algorithms jet reconstruction algorithms used at some previous collider experiments, such as UA2 [54], do not satisfy this infrared and collinear safety.

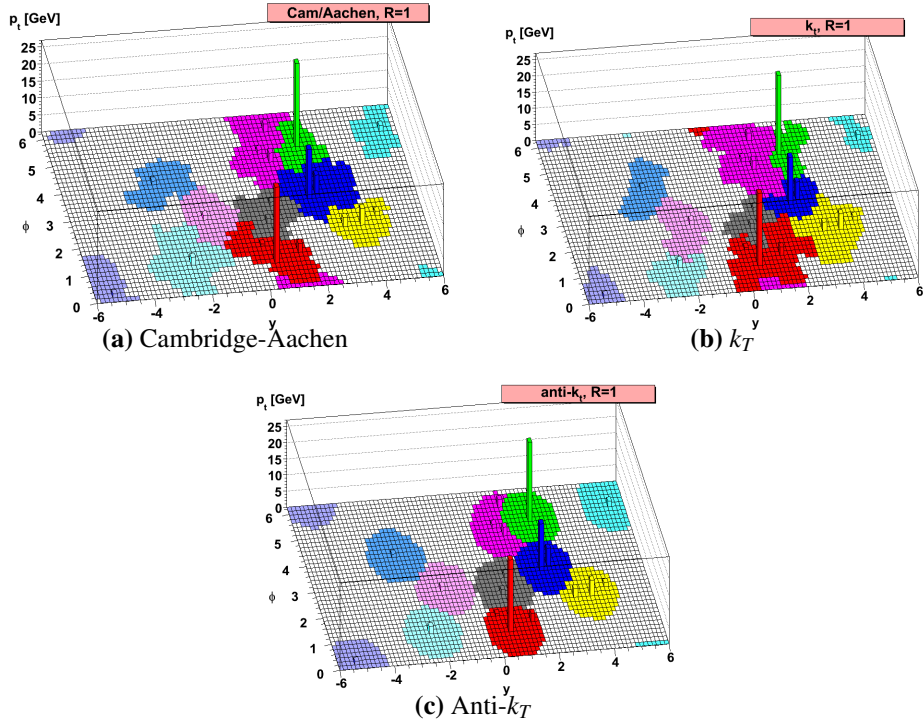


**Figure 4.3:** A comparison of the jets formed using the (a) Cambridge-Aachen, (b)  $k_T$  and (c) anti- $k_T$  algorithm from the same simulated event. The constituent clusters of each of the jets formed is indicated using various colours [55].

### 4.2.3 Jet Calibration

The jets initially formed by the jet reclustering algorithms from the topoclusters will not represent the energy of the parton that initiated the parton shower (known as the initial parton) and as such will not give an accurate dijet mass reconstruction which is required for the analyses presented in this thesis. As a result, a hadronic jet calibration is required to map the initial reconstructed jet to a more representative calibrated jet that can be used in an analysis.

The key factors for the unrepresentative hadronic jet energy measurement are [11, 56]:

- **Jet energy scale:** As discussed in Section 3.2.3.2, the ATLAS calorimeter is non-compensating which means that the calorimeter response is different for an EM-object and a hadronic object. The calorimeter response is calibrated at the EM-scale such that the energy measurements from a calorimeter cell are correct for an EM-object; as a result the initial energy measurement for a hadronic jet will be incorrect. To account for

this a correction is required to take the jet energy measurement from the EM-scale to the hadronic-scale.

- **Dead Material:** The hadronic jet may overlap with an unresponsive region of the detector, resulting in some energy deposits being incorrectly measured.
- **Leakage:** Some energy from the jet will be distributed outside the angular acceptance of the calorimeter whilst some energy will pass through the calorimeter in a process known as ‘punch-through’, as discussed in Section 3.2.4.
- **Reconstruction Issues:** There are two issues with jet reconstruction that require correction: firstly, some energy deposits coming from the initial parton may not be constructed as topoclusters due to the cell signal significance thresholds required in topocluster formation. Secondly, some topoclusters that should be clustered to the jet may not included in the reconstructed jet or included in a different jet instead.
- **Pile-up:** Energy from collisions other than the hard-scatter collision can also be included by the reclustering algorithm. This includes in-time and out-of-time pile-up. A definition of pile-up can be found in Section []. **LM Fix: Need a description of pile-up, probably in LHC running conditions**

As a result of the factors listed above a correction to the jets must be applied; which is done using the procedure described in [57]. An executive summary of the procedure is found below.

An important input of applying a calibration is deciding what one is correcting with respect to. The truth initial parton seems at first like a good choice, however this correction depends strongly on the theoretical modelling of the parton shower and hadronisation process, hence, this would mean that the calibrated jets are not model-independent. Instead, in ATLAS jets are corrected with respect to a ‘truth jet’; where a truth jet is defined as a jet formed by running the anti- $k_T$  algorithm on the set of stable truth particles in a simulated event. A stable particle is required to have a lifetime  $c\tau > 10$  mm and muons, neutrinos, and particles from pile-up collisions are ignored. Truth jets are well-defined and model-independent objects representing the jets that would have been reconstructed if one had a perfect detector; therefore they are a good choice for jet corrections.

The calibration process uses Monte-Carlo simulation and data to correct reconstructed

jets using a number of steps; starting from the jets initially formed from the EM-scale topoclusters. These steps are outlined in Figure 4.4.

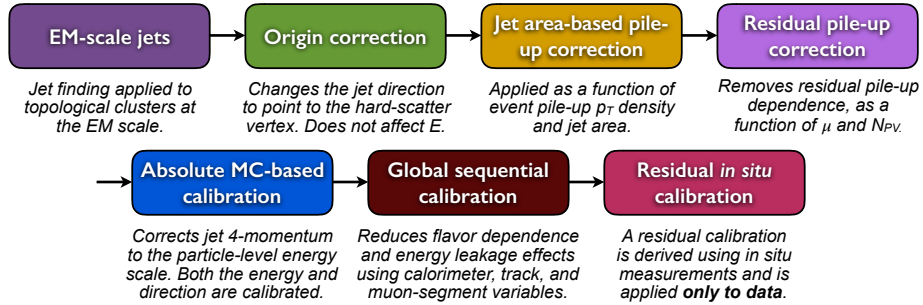


**Figure 4.4:** Calibration stages for the EM+JES calibration scheme [57].

To discuss each step in a little more detail:

- **Origin Correction:** This step changes the direction of the jets such that the four-momentum points to the hard-scatter primary vertex rather than the centre of the detector. This calculation conserves the jet energy.
- **Jet Area-Based Pile-up Correction:** This step removes unwanted energy contributions from pile-up. This correction subtracts the area of the jet,  $A$ , multiplied by the average energy density due to pile-up,  $\rho$ .
- **Residual Pile-up Correction:** This step further reduces effects from pile-up utilising the linear dependence of pile-up effects on the number of primary vertices,  $N_{PV}$  and the mean number of additional  $pp$  collisions per bunch crossing of the event,  $\mu$ .
- **Absolute JES Correction:** This step corrects the jet four-momentum from the EM-scale, at which they were initially formed, to the hadronic-scale, which is defined in terms of the truth jets in simulation. This correction is derived using truth jets and reconstructed detector-level jets in dijet Monte-Carlo events.
- **Global Sequential Calibration:** This step uses information from the calorimeter, muon spectrometer and track-based variables to refine the reconstructed energy and reduce the overall uncertainties.
- **In-situ calibration:** All previous steps in this calibration have been done using simulation to correct detector-level jets to truth jets. This step accounts for any differences between simulation and data. This step uses events containing a jet to be calibrated and a

well-measured reference objects, including photons, Z bosons, and calibrated jets. Then conservation of momentum gives us information on the true  $p_T$  of the jet to be calibrated. One can calculate a double ratio with respect to jet- $p_T$ ;

$$\text{Correction} = \frac{1}{R(p_T, \eta)} = \frac{\langle p_T^{\text{jet}} / p_T^{\text{ref}} \rangle_{\text{MC}}}{\langle p_T^{\text{jet}} / p_T^{\text{ref}} \rangle_{\text{Data}}} \quad (4.4)$$

which is applied as a correction to jet  $p_T$  in data; this correction is not applied in simulation.

This calibration scheme is known as an EM+JES, as the topoclusters are at the EM-scale. Here, I should note that there are other schemes used for calibrating jets at ATLAS, for example some analyses [58] correct each topocluster to the hadronic scale before clustering the jet, in a scheme called Local Cluster Weighted (LCW) [52]. EM+JES is generally used in ATLAS analyses as it is a simpler calibration scheme than LCW, but provides similar results.

The end result of the processes described in this section is a jet, reconstructed from EM-scale topoclusters using an anti- $k_T$  algorithm with a jet width parameter  $R=0.4$ , which has been calibrated using simulation and a data-driven in-situ step. The result of this process is what is known as an anti- $k_T$   $R=0.4$  EM+JES jet, and is the definition for a jet in this thesis.

#### 4.2.4 Jet Energy Uncertainties

All measurements have uncertainties, and this section investigates the uncertainties of jet energy measurement. Jet energy measurements separate the associated uncertainties into two components; jet energy resolution and jet energy scale.

Jet energy resolution (JER) is defined as  $\sigma(E)/E$ , and JER uncertainties come from an imperfect simulation of detector resolution in Monte-Carlo simulation. This uncertainty is measured using an in-situ technique from the balancing of jets in 8 TeV collision data which is extrapolated for 13 TeV data; the final uncertainty accounts for this extrapolation. Figure 4.5 shows the fractional JER uncertainty as a function of jet- $p_T$  and jet- $\eta$ . Full details on the derivation of this uncertainty can be found in [56] and [59].

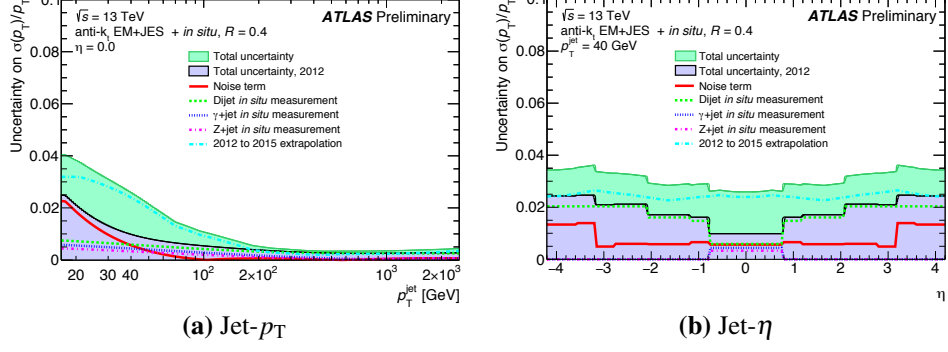


**Figure 4.5:** The fractional jet energy resolution uncertainty as a function of jet- $p_T$  and  $\eta$ . The total uncertainty is shown as are the contributions from the various sources of uncertainty [56].

Jet energy scale (JES) uncertainties arise from the calibration procedure to correct jets from the EM-scale to the hadronic-scale, outline above. 80 separate uncertainties are derived to cover each step of the calibration, the dominant uncertainties arise from the data-driven in-situ step [57]. Figure 4.6 shows the fractional JES uncertainty as a function of jet- $p_T$  and jet- $\eta$ .

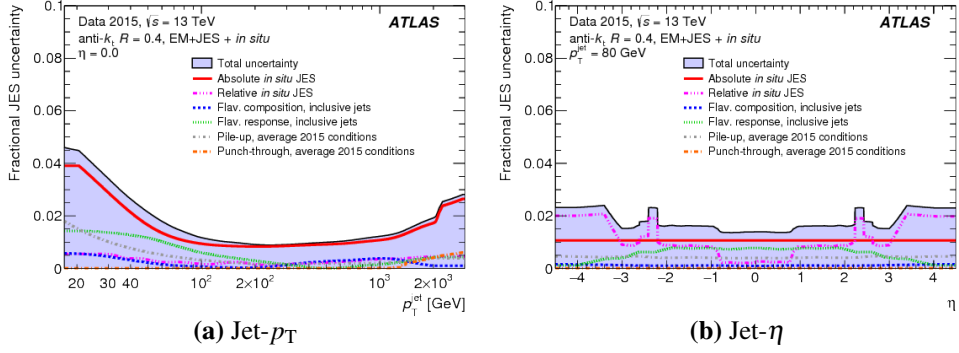


**Figure 4.6:** The fractional jet energy scale uncertainty as a function of jet- $p_T$  and  $\eta$ . The total uncertainty is shown as are the contributions from the various sources of uncertainty [57].

## 4.3 *b*-Jets

Hadronic jets, described in Section 4.2, can be further categorised into three separate categories based on the flavour of the constituent quarks. *b*-jets are defined as jets containing one or more *b*-hadrons, *c*-jets are defined as jets containing one or more *c*-hadrons but no *b*-hadrons and finally light-flavoured jets comprise of only light hadrons (formed of *u*, *d* and *s* quarks). A description of how this definition is practically used in simulation is given in Section 4.3.1.

The identification of *b*-jets, known as *b*-tagging, is an essential tool in a range of ATLAS collaboration results; for example analyses studying the  $t\bar{t}$  final state [60]<sup>4</sup> and the first direct evidence of the Higgs boson coupling to the quark-sector [51]. In the same sense, identification of *b*-jets is an essential part of the analysis being presented here; by selecting *b*-jets we increase our sensitivity to BSM models that decay to 1 or 2 *b*-jets in their final state. **LM Fix, link to where I explain why this is good, maybe Intro.**

The process of *b*-tagging at ATLAS in Run-2 has been previously described in great detail [61, 62], so what follows is a summary of the key features of the process.

### 4.3.1 Assigning a Flavour Label

In simulation, the particle-level truth information is known, and hence a truth flavour label of a jet can be defined. Flavour is assigned to jets by matching truth-level heavy-hadrons with  $p_T > 5 \text{ GeV}$  and  $\Delta R < 0.3$  between the hadron and the jet. If a *b*-hadron is matched to a jet, the jet is then declared a *b*-jet; this process is then repeated for *c*-hadrons and then  $\tau$  leptons. If no match between *b*, *c* or  $\tau$  is achieved then the jet is assigned as a light-flavour jet. The matching is exclusive, which means that each particle is only assigned to one jet. This definition of truth flavour in simulation is used generally within this thesis.

### 4.3.2 Baseline *b*-tagging Algorithms

To identify *b*-jets, *b*-tagging algorithms utilise the long lifetimes of the heavy-hadrons that decay through the flavour changing weak interaction. A hadron containing a *b*-quark has a lifetime  $\sim 1.6 \text{ ps}$  [3]. A *b*-jet decay chain will typically contain two of these flavour

---

<sup>4</sup>Section 5.3 contains an analysis utilising *b*-tagging in the  $t\bar{t}$  final state.

changing interactions, as at the quark level, the *b*-quark contained in the jet will decay to a *c*-quark, which will then decay into a *u* or *d* quark. The lifetimes of the heavy flavour hadrons means that they will decay a measurable distance from the primary vertex, the point where the hard-scatter collision occurs; for example a  $B_0$  meson with a  $p_T$  of  $x$  GeV will travel approximately  $x/10$  mm. Hence, the flavour of a jet can be inferred from the presence of particles that originate from a point offset from the primary vertex.

In practice this is performed using the topology of tracks and properties of the jets, which have been described in Section 4.1 and 4.2 respectively. To utilise tracks and jets in tandem one must associate the tracks to the jets, which is performed by requiring small angular separation  $\Delta R$  between the two objects. The maximum value of  $\Delta R$  for association varies as a function of the jet- $p_T$ , resulting in a narrower cone for high- $p_T$  jets which are more collimated. At 20 GeV, it is 0.45 while for more energetic jets with a pT of 150 GeV the cut is 0.26. Tracks are exclusively matched, meaning each track is only associated with one jet, chosen using the smallest value of  $\Delta R$ .

There are three base *b*-tagging algorithms utilised to produce discriminating variables [62], which are described in the next three sections. The variables are then combined in a multi-variate algorithm which is described in Section 4.3.3. Figure 4.7 shows a schematic illustrating how tracks are used by the three *b*-tagging algorithms to identify a *b*-jet, the details of this figure are referred to in the following three sections.

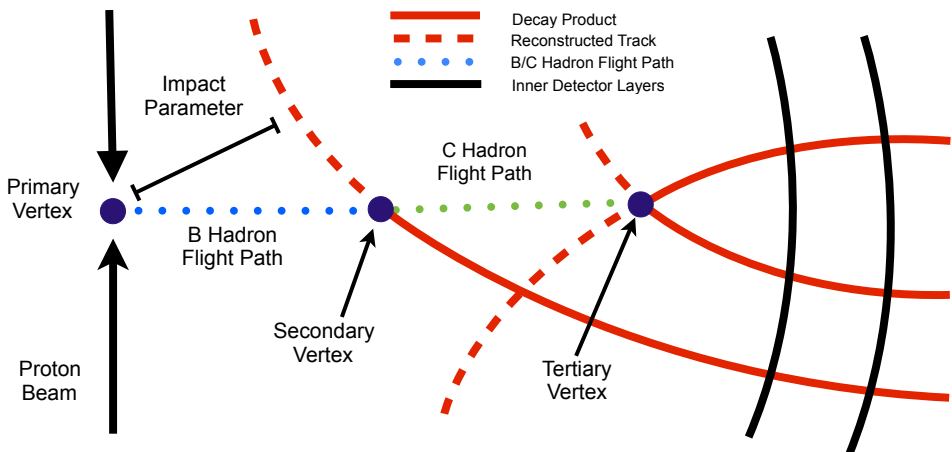


**Figure 4.7:** A diagram to illustrate the key features of a *b*-jet that are utilised by the base *b*-tagging algorithms.

### 4.3.2.1 Impact parameter based

The IP3D algorithm is utilises the impact parameter, which is defined as the shortest distance between a specific track and the primary vertex. A track corresponding to a particle coming from the offset decay vertex of a heavy-hadron is likely to have a large impact parameter, meaning that the distribution of track impact parameter is different for each of the jet-flavours. The impact parameter of a track coming from the decay of a heavy hadron is indicated in Figure 4.7. In this algorithm, for all tracks associated to a jet, the impact parameter is calculated in both the transverse (perpendicular to beam-line) and longitudinal (parallel to beam-line) direction, which are referred to as  $d_0$  and  $z_0$ . Then the IP3D algorithm calculates a likelihood of the jet having a specific flavour, based on the distributions of the impact parameters ( $d_0, z_0$ ) and their significances ( $d_0/\sigma_{d0}$  and  $z_0/\sigma_{z0}$ ) for tracks within the jet. Another similar algorithm, IP2D, also calculates the jet flavour likelihood from just the transverse distributions, ( $d_0$  and  $d_0$  significance), which is more robust to pile-up, as tracks from pile-up jets are likely to have a large  $z_0$  significance value.

### 4.3.2.2 Secondary vertex

The SV1 algorithm aims to reconstruct a secondary vertex of two or more intersecting tracks, corresponding to the decay of a heavy-flavour hadron; the secondary vertex within a *b*-jet's decay chain is illustrated in Figure 4.7. The SV1 algorithm then calculates many variables that are associated with properties of the reconstructed secondary vertex that show flavour discrimination; some example variables are the vertex invariant mass, which will be larger for *b*-jets due to the heavy mass of the *b*-hadron<sup>5</sup>, the distance in the transverse plane between the primary vertex and the secondary vertex, which will be larger for *b*-jets due to the long lifetime of the *b*-hadron, and the number of tracks at the secondary vertex, which will be larger for reliable secondary vertices.

### 4.3.2.3 Jet Fitter

The JetFitter algorithm (JF) attempts to reconstruct the full decay chain of the *b*-hadron into a charmed-hadron and then into light-hadrons. This is done by assuming that all vertices lie on a common *b*-flight axis, and then constructing vertices from the intersection of one or

---

<sup>5</sup>Mass of a  $B_0$ -meson  $\sim 5$  GeV which is the most common *B*-hadron in a *b*-jet [3].

more tracks and the flight axis. The aim of this is to reconstruct the secondary and tertiary vertices which correspond to the decays of the *b*-hadron and charmed-hadron, as illustrated in Figure 4.7. Similar to SV1, the JetFitter algorithm then calculates a number of flavour discriminating variables: for example vertex mass and number of vertices with two or more tracks.

### 4.3.3 Multi-Variate *b*-tagging Algorithm

The three base algorithms are combined in a boosted decision tree (BDT), a machine-learning technique for combining the many flavour-discriminating variables, resulting in an algorithm that is known as MV2. As shown in Figure 4.8, MV2 combines the likelihood output of IP3D and IP2D with the discriminating variables of SV1 and JF discussed in the preceding sections, resulting in an output between -1 and 1, where 1 indicates that the jet is very likely to be a *b*-jet and -1 indicates the inverse.

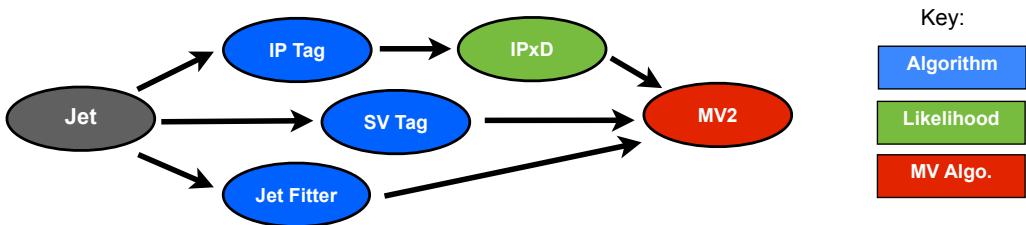


**Figure 4.8:** A diagram illustrating how three base flavour tagging algorithms are combined in the MV2 algorithm.

The BDT is trained using a simulated sample of  $t\bar{t}$  events that will contain a mix of *b*-, *c*- and light-jets as well as a sample containing a  $Z'$  boson decaying to *b*-quarks to increase statistics in the high jet- $p_T$  region. The training makes use of the truth flavour labels assigned to jets using the process described in Section 4.3.1. A training sample with known truth labels is required as this allows the BDT to be optimised such that it uses the complex correlations between the input variables to allow for high *b*-jet efficiencies whilst still obtaining a large *c*- and light-jet rejection. Subtly different algorithms can be obtained using samples containing different fractions of light and *c*-jets, the fraction of *c*-jets used is labelled in the algorithm name; for example the MV2c10 algorithm has been trained on a sample containing 10% charm-jets, which gives strong light- and *c*-rejection.

A cut is then applied to this MV2 output in order to select jets that are likely to *b*-jets. The choice of cut will vary the *b*-jet efficiency, light-jet rejection and *c*-jet rejection, where

*b*-jet efficiency is defined as the probability of accepting a true *b*-jet, light-jet rejection is defined as 1 divided by the probability of accepting a true light-jet, and a similar definition applies for *c*-jet rejection. Figure 4.9 shows the *b*-jet efficiency against (a) light and (b) *c*-jet rejection of the MV2 algorithm for a continuous range of cuts. The different lines show the performance of the algorithm in the 2015 configuration [61] and in the 2016 configuration [62] where a range of different fraction of *c*-jets are used in the training; 2016 MV2c10 is the configuration used generally in this thesis as recommended in [62].

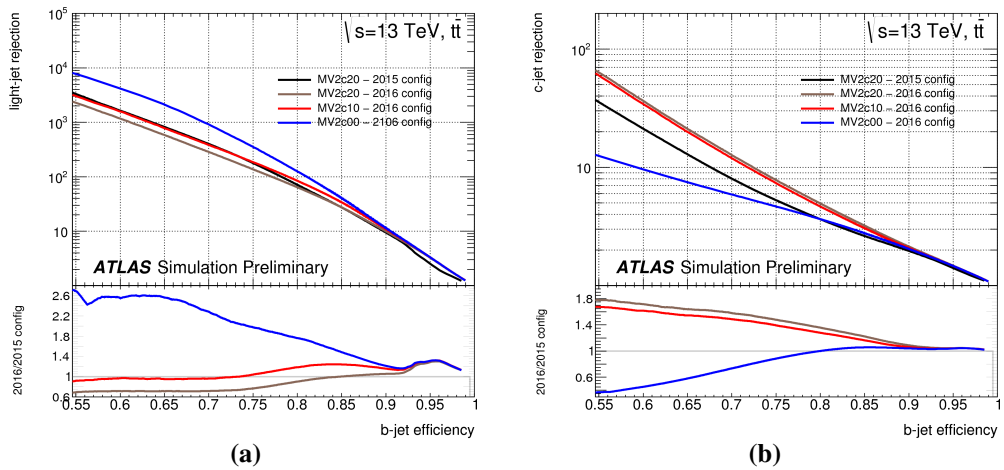


**Figure 4.9:** The expected *b*-jet efficiency of *b*-tagging algorithm, MV2, with respect to (a) light-jet and (b) *c*-jet rejection in simulated  $t\bar{t}$  events. The various lines show the performance of the algorithm for different configurations and training setups [62].

ATLAS has a set of common pre-set cuts used, known as operating points, such that work required to calibrate *b*-tagging in each analysis is shared. Looser operating points have a relatively low cut on MV2 output, meaning that the *b*-jet efficiency is higher at the cost of worse light- and *c*-jet rejections, and the inverse is true for tighter operating points. Table 4.1 shows the list of fixed cut operating points that are used in ATLAS with a given cut on MV2c10 output; shown with the corresponding benchmark *b*-jet efficiency, *c*-jet rejection, light-jet rejection and  $\tau$  rejection.<sup>6</sup>

---

<sup>6</sup>In this thesis only the fixed-cut operating points shown above will be used, however, there also exists a set of flat efficiency operating points where the MV2 cut depends on jet- $p_T$

MV2 Cut Value	<i>b</i> -jet efficiency [%]	<i>c</i> -jet rejection	Light-jet rejection	$\tau$ rejection
0.9349	60	34	1538	184
0.8244	70	12	381	55
0.6459	77	6	134	22
0.1758	85	3.1	33	8.2

**Table 4.1:** The Mv2c10 *b*-tagging algorithm operating points; with the corresponding *b*-jet efficiency, *c*-jet rejection, light-jet rejection and  $\tau$  rejection. This table is taken from reference [62].

### 4.3.4 Calibration and Uncertainties

As with any part of a measurement, the process of *b*-tagging must be calibrated using data. *b*-tagging calibration is performed using a pure sample of *b*-jets extracted from di-lepton  $t\bar{t}$  events using the probability distribution function method [63, 64]. With the pure *b*-jet sample one can calculate the *b*-jet efficiency,  $\epsilon_{b\text{Tag}}$ , defined as:

$$\epsilon_{b\text{Tag}} = \frac{N(\text{*b*-tagged true *b*-jets})}{N(\text{True *b*-jets})} \quad (4.5)$$

where *b*-tagged means above the cut on the MV2 output for a given operating point. By measuring  $\epsilon_{b\text{Tag}}$  in both data and in Monte-Carlo simulation one can derive a correction to simulation, known as a data/MC scale factor ( $SF_{b\text{Tag}}$ ), defined as:

$$SF_{b\text{Tag}} = \epsilon_{b\text{Tag}}^{\text{Data}} / \epsilon_{b\text{Tag}}^{\text{MC}} \quad (4.6)$$

Uncertainties are derived for the scale factors to account for factors such as uncertainties in the modelling of the backgrounds in simulation and uncertainties in the modelling of the detector response to electrons, muons and jets. The dominant uncertainty comes from modelling of  $t\bar{t}$  in simulation. Figure 4.10 shows the data/MC scale factor measured in 2015 and 2016 data as a function of jet  $p_T$ . The scale factor is consistent with unity within uncertainties everywhere, showing that *b*-tagging is generally well-modelled in simulation.

The *b*-tagging calibration using di-lepton  $t\bar{t}$  events described above is unable to measure a data/MC scale factor for jets with  $p_T$  greater than 300 GeV, due to low data statistics in the high- $p_T$  region. Thus, the measured scale factors are extrapolated to cover the high jet- $p_T$  region, and that this extrapolation procedure introduces additional uncertainties [65]. The extrapolation and uncertainty is calculated from simulated events by considering vari-

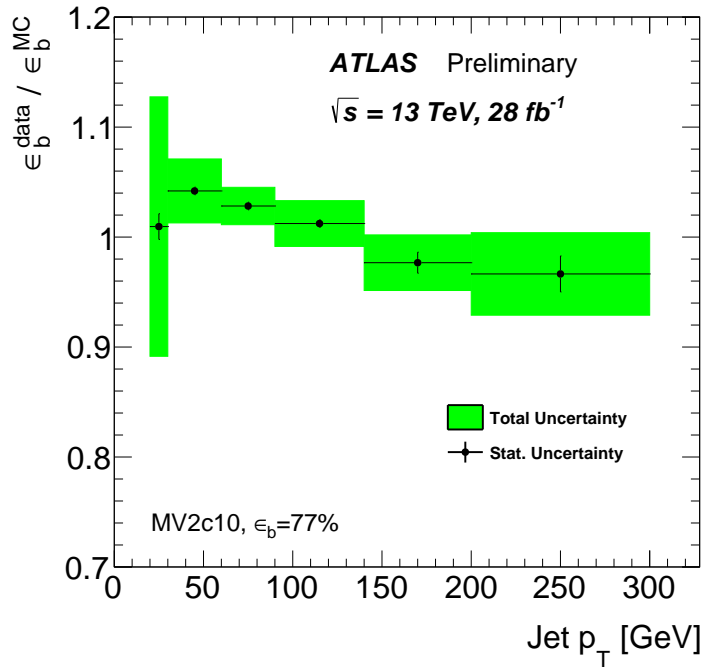


**Figure 4.10:** Ratio of b-tagging efficiency in data and Monte Carlo for the MV2c10 b-tagging algorithm at the 77% working point as a function of jet- $p_T$ , extracted using di-lepton  $t\bar{t}$  events. Statistical uncertainties (black lines) and total uncertainties (green shaded region) are shown [64].

ations on the quantities affecting the *b*-tagging performance such as the resolution of the impact parameter, quality of reconstructed tracks, description of the detector material, and number of tracks per jet. The dominant effect on the uncertainty when extrapolating to the high jet- $p_T$  region is related to the different tagging efficiencies when varying the track impact parameters. **Question for AK; this paragraph inspired from flag tag recommendation on a twiki; reference is internal. :/**

### 4.3.5 *b*-Jet Energy Scale

In Sections 4.2.3 and 4.2.4 it was described that one must apply a correction to correct the energy of a jet from the detector-level to the true particle-level jet energy and this correction had an associated uncertainty. For *b*-jets this correction may be different to light jets due to differences in the parton shower and hadronisation processes for a *b*-jet; for example during the decay of the *b*-hadron muons and neutrinos are produced which will not deposit all/any of their energy in the calorimeter which could affect the scale of the correction. This effect is known as the *b*-jet energy scale (*b*JES) and is accounted for with an additional uncertainty.

The *b*JES uncertainty is derived and validated in data by comparing the measured jet energy with respect to an independent well calibrated object, in this case tracks, as described in Appendix H of [66]. We perform this comparison for *b*-jets and inclusive jets for a dijet sample in simulation and data, where a *b*-jet means it has been *b*-tagged at the 85% operating point and inclusive means no requirement on *b*-tagging has been applied. To do the track-jet comparison tracks are associated to jets using ghost association. Ghost association re-runs the jet clustering algorithm used to form the jets in an event, using tracks with  $p_T$  manually set to 0 as inputs in addition to the usual calorimeter topoclusters. As the tracks have  $p_T$  set to 0, the jet reconstruction algorithm will form the same jets as before, except that tracks will now be associated to the various jets.

The measured jet- $p_T$  is compared to the sum of the tracks associated to the jet,  $\Sigma p_T^{trk}$  using the observable,  $r_{trk}$ , defined as

$$r_{trk} = \Sigma p_T^{trk} / p_T^{jet} \quad (4.7)$$

One can split up the expected value of the observable  $r_{trk}$  into three components.

$$\langle r_{trk} \rangle = \langle \frac{\Sigma p_T^{trk,truth}}{\Sigma p_T^{trk,reco}} \rangle \langle \frac{p_T^{jet,truth}}{\Sigma p_T^{trk,truth}} \rangle \langle \frac{p_T^{jet,reco}}{p_T^{jet,truth}} \rangle \quad (4.8)$$

The first term describes the track energy response which, as tracks are calibrated, has been measured in data and simulation. The second term is the mean charged fraction of the jet,  $\langle f_{charge} \rangle$ , which will be estimated from simulation. The third term is the jet energy response, which is the jet energy scale correction that we are interested in measuring.

The systematic uncertainties that cover the measurement of  $r_{trk}$  arise from the jet and  $b$ -jet modelling in simulation (referred to as fragmentation),  $b$ -tagging calibration, jet resolution and tracking efficiency. In addition, an uncertainty to cover a bias observed in  $\langle f_{charge} \rangle$  for  $b$ -tagged jets relative to inclusive jets is added to the relative systematic uncertainty. The uncertainty on the  $r_{trk}$  measurement are used as the  $b$ JES uncertainty, which varies between 1-4% depending on jet- $p_T$ . Figure 4.11 shows the derived total  $b$ JES uncertainty with respect to jet- $p_T$ , the components that contribute to the uncertainty are also shown.

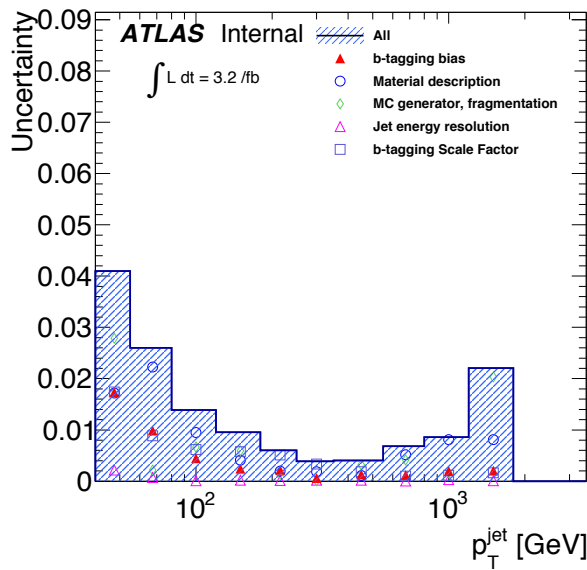


**Figure 4.11:** The total fractional  $b$ JES uncertainty shown with the various contributions [66].

Then one can test the derived  $b$ JES uncertainties in data using a double ratio approach. The first ratio compares the observable in data and Monte-Carlo;

$$R_{trk} = r_{trk}^{Data} / r_{trk}^{MC} \quad (4.9)$$

And then the double ratio,  $R'_{trk}$  compares the  $R_{trk}$  for  $b$ -jets and inclusive jets;

$$R'_{trk} = R_{trk}^{b-jet} / R_{trk}^{incl.} \quad (4.10)$$

The double-ratio approach means that many of the uncertainties unrelated to  $b$ JES are can-

celled in the ratios.

Figure 4.12 shows the double ratio  $R'_{trk}$  with the *b*JES uncertainty applied. The ratio is almost consistent with unity within uncertainties validating our *b*JES uncertainty in data.

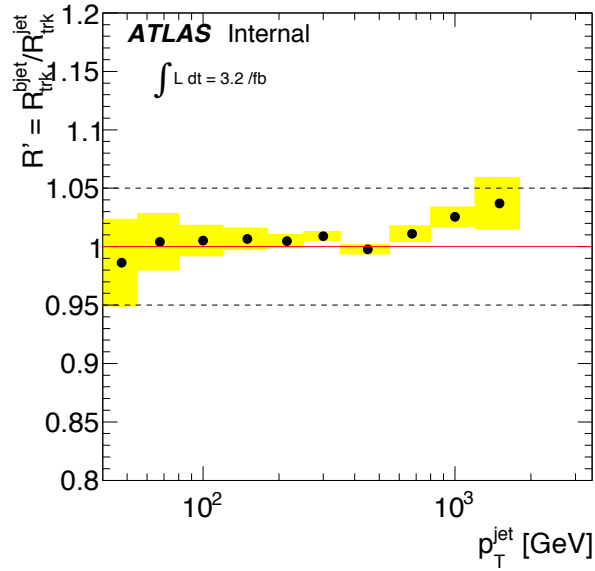


**Figure 4.12:** The validation of the *b*JES uncertainty in data using the double-ratio  $R'_{trk}$  [66].

## 4.4 Electrons and Muons

Reconstruction of electrons and muons is important for a number of analyses at ATLAS; including the selection of di-lepton  $t\bar{t}$  events which are used in the calibration of  $b$ -tagging and the  $b$ -jet trigger, described in Sections 4.3.4 and 5.3 respectively. As these objects are not used in the final analysis presented in this thesis, they are described below in less detail than has been given to jets and  $b$ -jets.

Electron<sup>7</sup> reconstruction at ATLAS [67] uses the matching of narrow clusters of energy deposits in the calorimeter to a track from the inner detector, from which the four-momentum of the electron can be determined. Information such as the calorimeter shower shape, properties of the matched track and TRT transition radiation (described in Section 3.2.2) allows for identification of electrons with respect to other physics objects described in this section. Three different operating points are provided for electron identification: which are, in order of increasing background rejection *Loose*, *Medium*, and *Tight*.

Muon<sup>8</sup> reconstruction at ATLAS uses muon tracks reconstructed using the Muon Spectrometer (MS) and tracks constructed by the Inner Detector (ID). There are several types of muon reconstruction techniques and different muon identification working points available [68].

Two of the techniques for reconstruction are combined muons and extrapolated muons. Combined muons are reconstructed by extrapolating muon tracks inwards to match tracks formed by the ID. Extrapolated muons are formed from muon tracks alone, with a loose requirement on the track pointing to the primary vertex; extrapolated muons are important in the range  $2.5 < \eta < 2.7$  for which there is no ID coverage. Again for reconstructed muons the four-momentum can be determined.

Four muon identification working points have been defined *Loose*, *Medium*, *Tight*, and *High- $p_T$* . Medium muons, as used in Section 5.3, are made up of combined and extrapolated muons that pass a quality criteria based on number of MS hits, track fit quality and, where relevant, compatibility between the ID and MS tracks.

---

<sup>7</sup>For the purposes of reconstruction positrons are included as a subset of electrons

<sup>8</sup>Similar to positrons, in reconstruction anti-muons are included as a subset of muons

## 4.5 Further objects

In the previous sections of this chapter all objects used in the analyses presented in this analysis have been described. However this is not an exhaustive list of the range of objects that ATLAS can reconstruct. In this section I will briefly outline some of the many other objects of interest that are used elsewhere in ATLAS analyses.

- **Photons:** Photons can be identified from using narrow clusters of energy deposits in the calorimeter similar to that of electrons, except with no track associated [69]. Information such as the calorimeter shower shape and TRT transition radiation allows for identification of electrons with respect to other physics objects, notably electrons.
- **Taus:** Taus, in their most common decay mode, can be identified and reconstructed using narrow calorimeter jets associated to a topologies of tracks that match their known decay chain [70].
- **Missing Transverse Momentum:** It is known that the momentum in the transverse plane is conserved, hence from the negative sum of the momentums of all reconstructed physics objects in an event one can determine the presence of missing transverse momentum (MET) [71]. MET can be used to identify the presence of particles that interact weakly with the ATLAS detector, such as neutrinos [51] or even dark matter [72].

## Chapter 5

# Triggering in the di-*b*-jet analysis

As described in Section 3.3, ATLAS does not have the resources to process and store all the data from the 40 MHz of collisions delivered by the LHC. To solve this problem the ATLAS trigger system performs the vital role of reducing the rate of data-taking to 1 kHz by selecting events containing a high- $p_T$  object.

As a result all analyses must chose a trigger strategy and understand the impact of this trigger on their analysis. In the di-*b*-jet analysis a single jet trigger is used for the high-mass channel and a double *b*-jet trigger for the low-mass channel. This chapter aims to provide a detailed description of the triggers used in this analysis, and as such is organised in the following manner; Section 5.1 provides a brief description of jet triggers as used in the high-mass channel and the limitations of this approach, Section 5.2 contains a description of *b*-jet triggers that are used in the low-mass channel and finally Section 5.3 presents the measurement of the *b*-jet trigger efficiency, an essential input of the low-mass channel.

## 5.1 Jet-Triggers

Jet-triggers are tasked with selecting events with one or more jets from the deposits in the ATLAS calorimeter system, this is one of most challenging triggers in any hadron-hadron collider due to the extremely high cross-sections of hadronic jet production [73]. In Run-2 the jet-triggers are used at both L1 and HLT level; each using different levels of information and different algorithms, so are described separately within this section.

### 5.1.1 Level 1

The L1 trigger is a hardware based trigger which accepts or rejects an event within  $2.2\,\mu\text{s}$ . The L1 jet-trigger receives trigger towers from the calorimeter; where a trigger tower is the measured energy deposit in a cell of the ECAL or HCAL of granularity  $0.1 \times 0.1$  in the  $\eta - \phi$  plane. In the L1 trigger hadronic jet algorithms search for a neighbouring group of  $4 \times 4$  trigger towers containing energy deposits above some pre-set threshold. Our analysis uses the L1 trigger known as `L1_J100`, which requires that at least one trigger tower group with an energy deposit of  $100\,\text{GeV}$  has been found. Other L1 triggers that search for multiple clusters are also possible to reduce the energy thresholds required. The L1 trigger then seeds the HLT trigger. It is also worth noting that at L1 there is no tracking information, meaning that electron and taus are also triggered on using similar techniques as hadronic jet algorithms, except using narrower groups of trigger towers.

### 5.1.2 HLT

The HLT trigger is a software based trigger which, due to the lower input rate and larger time window, is able to use more complex algorithms to reconstruct jets. At the HLT level jets are reconstructed using topoclusters (TCs) constructed from neighbouring cells selected using the cell's energy significance ( $E/\sigma$ ); TCs are seeded from cells with  $E/\sigma > 4$ , then neighbouring cells with  $E/\sigma > 2$  are added and finally all neighbouring cells around are also added. Jets are then reconstructed from the topoclusters; in this analysis jets have been reconstructed using the anti- $k_T$  algorithm with an  $R = 0.4$ <sup>1</sup>.

### 5.1.3 High-mass trigger selection

For the high-mass analysis the trigger `HLT_j380` is used, that is fired when a jet is found with a  $p_T > 380\,\text{GeV}$ . This is chosen as it is the lowest un-prescaled single jet-trigger; meaning that of triggers that accept every event passing a single jet criteria, this trigger has the lowest jet- $p_T$  threshold. Due to the exponential increase in jet production cross-section at low jet- $p_T$ , the  $p_T$  threshold is set to keep the acceptance rates low enough such that the HLT trigger is within its output rate budget of  $1\,\text{kHz}$ .

However, as will be discussed further in Section ??(sec:evtSel), this  $p_T$  threshold limits

---

<sup>1</sup>Section 4.2 (sec:obj-jets) defines these terms

the high-mass di-*b*-jet analysis to only select events with  $m_{jj} > 1.2$  TeV. Otherwise the  $m_{jj}$  range will enter a kinematic region where trigger acceptance is less than 1 in such a way that the QCD background is sculpted in a manner that the background modelling can not adapt to. To reach lower masses a different trigger strategy is required.

## 5.2 *b*-Jet Triggers

This analysis searches for pairs of *b*-jets, which, as described in Section 4.3(*sec:obj-bjets*), can be identified from the topology of tracks in the inner detector indicating that a *B*-hadron was within the jet. The same techniques can be used at the trigger level to reduce rates significantly<sup>2</sup> allowing a lower jet- $p_T$  threshold than was used by the single jet- $p_T$  trigger, and hence lower  $m_{jj}$  values to be accessed. *b*-jet triggers have been used in a range of previous ATLAS analyses including for searches for exotic particle decaying into a pair of Higgs bosons, which then decay to 4 *b*-jets [74].

### 5.2.1 General description

In 2016 data, the *b*-jet trigger configuration contains three steps [75], making use of the regions of interest (RoI) described by the jets found by the jet-trigger. Firstly, a ‘fast’-tracking algorithm is run in a super-RoI which is formed around all jets in the event which have  $E_T > 30$  GeV; these tracks are then used to identify the primary vertex in the event. Secondly, within each jet RoI precision tracking is run, with a constraint on the PV position from the first step. Finally, these tracks are the input to the multi-variate *b*-tagging algorithm described in Section 4.3.3(*sec:obj-bjets\_MV2*) to identify *b*-jets. There are several *b*-jet triggers available in the ATLAS trigger menu; with a variety of requirements on the jet multiplicity, number of tagged jets and *b*-tag operating point used. Figure 5.1 shows ROC curves representing the expected performance of the Run-2 *b*-jet trigger.

There are few subtleties worth commenting on the *b*-jet trigger configuration which affect decisions taken in this analysis. One is that on this figure there are two lines corresponding to different *b*-tagging algorithms used in *b*-jet trigger; IP3D+SV1 was used in 2015 data-taking, whilst the MV2c20 was used in 2016 data-taking. Another difference between 2015 and 2016 is the primary vertex finding algorithm used; 2016 data-taking em-

---

<sup>2</sup>It is known that the QCD background is dominated by light-jets, see Figure ??*Plot of background flav comp*

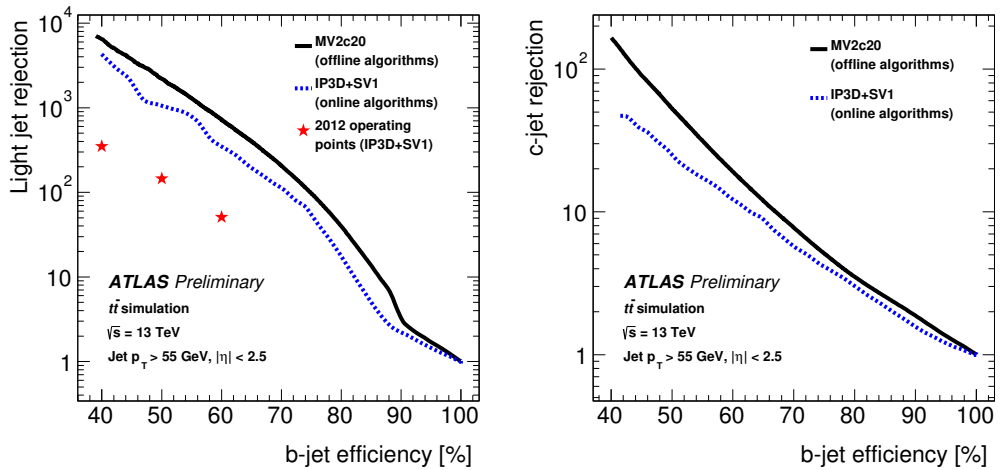


**Figure 5.1:** The expected *b*-jet efficiency of *b*-jet triggers with respect to (a) light-jet and (b) *c*-jet rejection in the case where the *b*-tagging algorithm used is MV2c20 (Black), IP3D+SV1 (Blue) and for the set-up used in Run-1 (red stars) [75].

ployed an algorithm based on offline primary vertex finding, known as `xPrmVtx`, whilst in 2015 an algorithm using a simpler histogram based approach was employed, known as `EFHist`.

Finally it is worth noting that there are differences between online and offline *b*-tagging that will have an impact on what is to follow. Firstly, coarser tracking information is available online, notably online tracks are not reconstructed from the whole range of the detector. Secondly, a slightly different training setup is used for the multi-variate algorithm, mainly that a different fraction of *c*-jets were present in the training sample; 10% were used offline and 20% were used online.

In this analysis a double *b*-jet trigger is used,

```
HLT_j150_bmv2c2060_split_j50_bmv2c2060_split
```

which triggers on two jets with  $p_T > 150$  and 50 GeV respectively, which have been *b*-tagged at the 60% efficiency working point.

## 5.3 Efficiency Measurement of the $b$ -Jet Trigger

Any part of the ATLAS detector framework needs to be understood and calibrated with data for use in an analysis; and this includes the trigger which can have a large impact on the analysis. In this section I discuss the strategy and results of the  $b$ -jet trigger efficiency measurement in 2016, which is an important input to the low-mass channel of the di- $b$ -jet analysis.

For clarity in this section I would like to make two definitions clear. Online refers to any algorithms run or objects reconstructed at the trigger level, offline refers to algorithms run after events have passed the trigger at the data-processing level.

### 5.3.1 Strategy

The  $b$ -jet trigger is always used in tandem with offline  $b$ -tagging which is calibrated independently of the  $b$ -trigger. As mentioned before, there are many differences between offline and online  $b$ -tagging. Hence, to do this measurement whilst making use of the offline  $b$ -tagging calibrations already available,  $b$ -jet trigger efficiency with respect to offline  $b$ -tagging,  $\epsilon_{bTrig}$ , is measured. This is defined as the number of offline-tagged true  $b$ -jets that match an online-tagged trigger-jet divided by the number of offline tagged  $b$ -jets that match a trigger jet. Or to put this in an equation;

$$\epsilon_{bTrig} = \frac{N(\text{Offline-tagged, online-tagged, true } b\text{-jets})}{N(\text{Offline-tagged, trigger-matched, true } b\text{-jets})} \quad (5.1)$$

This quantity can be interpreted as the probability that a true  $b$ -jet is tagged at the trigger-level, given that it there is a jet at the trigger level and that it would be  $b$ -tagged at the offline stage.

To measure  $\epsilon_{bTrig}$  a sample that has high  $b$ -jet purity is required, such that jets used to calculate this ratio are true  $b$ -jets. It is also necessary to trigger on this sample in such a way that there is no bias from using  $b$ -tagging online; or simply put the  $b$ -jet trigger cannot be used to select events. The sample used to fill these criteria is a di-lepton  $t\bar{t}$  sample containing a muon and an electron. Top-quarks decay to a  $W$ -boson and a  $b$ -quark with almost 100% branching ratio meaning that this sample provides a good source of  $b$ -quarks, but also the electron and muon give a distinct signature which allows us to select this process with good

purity and gives a non- $b$ -jet object to trigger on. The exact event selection is described below.

The  $b$ -jet trigger efficiency is determined in data and is compared to the efficiency found in a simulated  $t\bar{t}$  sample which is used to extrapolate the efficiency to higher jet- $p_T$  where the data-derived efficiency loses statistical precision. The efficiency in data, including the simulation based extrapolation, can then be compared to simulation to derive a Data/Monte-Carlo scale factor, which is used as the input to the analysis.

$\epsilon_{bTrig}$  and Data/Monte-Carlo scale factors are derived for all combinations of offline and online  $b$ -tagging working points. However, only the process for the 70% offline and 60% online working point is shown as this is set of working points used in this analysis.

### 5.3.2 Datasets

The data used for this analysis is the full 2016 ATLAS data-set. In addition to the usual data-quality requirements applied, as discussed in Section ?? a  $b$ -jet trigger aware Good Run List (GRL)<sup>3</sup> applies the requirement that the online beamspot  $z$ -position is within 2mm of the origin in Periods A-I of the data. This means that the data-set contains  $24.3 \text{ fb}^{-1}$  of data. A discussion of the requirement for this GRL is in Section 5.3.6.

For the simulated  $t\bar{t}$  sample, the generation is performed with a Powheg-Box v2 [76] generator with the CT10 PDF sets in the matrix element calculations. Also considered is a simulated single-top sample; electroweak t-channel, s-channel and  $Wt$ -channel single top-quark events are generated using the Powheg-Box v1 generator. This generator uses the 4-flavour scheme for the NLO matrix elements calculations together with the fixed four-flavour PDF set CT10f4. For both processes the parton shower, fragmentation, and the underlying event are simulated using Pythia6.428 [77] with the CTEQ6L1 [78] PDF sets and the corresponding Perugia 2012 tune (P2012) [79]. The top mass is set to 172.5 GeV. The EvtGen v1.2.0 program [80] is used for properties of the bottom and charm hadron decays.

---

<sup>3</sup>A GRL is effectively a list of lumi-blocks that pass certain data-quality requirements. As mentioned in the text a further discussion is held here in Section ??

### 5.3.3 Event Selection

A high-purity sample of  $b$ -jets is selected using a di-lepton  $t\bar{t}$  selection.

The event selection is summarised as follows:

- The event fired a single lepton bperf trigger which are:
  - HLT\_mu26\_imedium\_2j35\_bperf
  - HLT\_e26\_tight\_iloose\_2j35\_bperf
  - HLT\_e26\_lhtight\_iloose\_2j35\_bperf
- At least 1 medium muon:  $p_T > 25$  GeV, which has no jet within a  $\Delta R$  of 0.4.
- At least 1 medium electron:  $p_T > 25$  GeV.
- 2 offline  $b$ -tagged jets, defined as:
  - Offline  $R=0.4$  anti- $k_T$  jets.
  - $p_T > 35$  GeV and  $|\eta| < 2.5$ .
  - Offline  $b$ -tagged at the 85% operating point.
  - Jet must be matched to a trigger-jet.

Descriptions of the object-definitions of muons, electrons, jets and  $b$ -tagged can be found in Sections ??(sec:obj-muon), ??(sec:obj-elec), 4.2(sec:obj-jet) and 4.3(sec:obj-bjet) respectively. Online trigger jets are matched exclusively to offline jets using  $\Delta R$  matching, requiring for a match the jets must have  $\Delta R < 0.6$ .

The triggers used are bperf trigger, which are special triggers used in data-taking specifically for monitoring the  $b$ -jet trigger performance. They fire if a muon or an electron with  $p_T > 26$  GeV is reconstructed at the trigger level. The bperf triggers then run the online  $b$ -tagging algorithm on all trigger jets with  $|\eta| < 2.5$  and  $p_T > 35$  GeV without performing any cuts on the output of the multi-variate algorithm; ensuring there is no bias in the efficiency measurement.

### 5.3.4 The Initial Problem

To give context to the following section; the first discussion will be what was first observed when measuring the  $b$ -jet efficiency. To show the problems observed clearly, in this section the initial event selection is replicated; hence no  $b$ -jet trigger aware GRL is applied, offline jets are not required to match a trigger jet in the denominator and the triggers required are single lepton triggers without the additional  $b$ -perf functionality<sup>4</sup>. In addition, for this and the following two sections simulation refers to  $t\bar{t}$  only, but it will be shown later that the effect of single-top production is small so the conclusions here are still valid.

Figure 5.2 shows  $\varepsilon_{bTrig}$  against jet- $p_T$  and jet- $\eta$ ; the efficiency in data is substantially below the efficiency expected from simulation and shows a clear shape in jet- $\eta$  distributions. This substantial differences need to be investigated and understood.

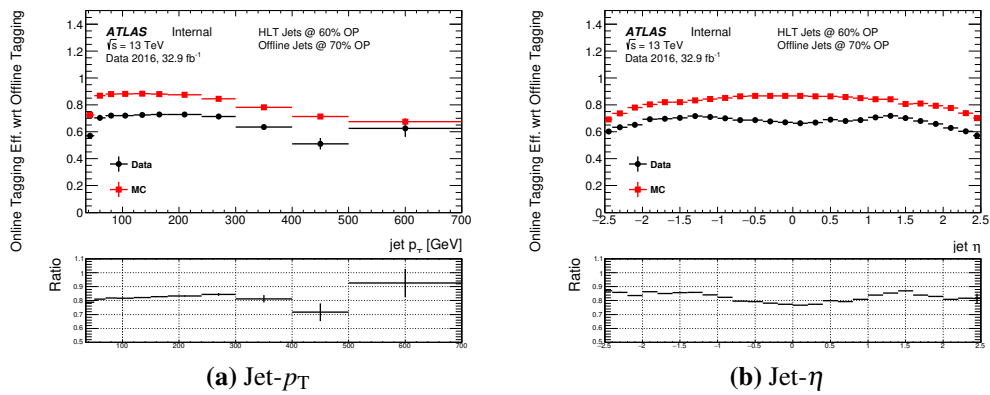


**Figure 5.2:** The 60%  $b$ -jet trigger efficiency with respect to an offline 70% operating point tag for Data (black) and simulation (red) against jet- $p_T$  (a) and jet- $\eta$  (b). The  $b$ -trigger aware GRL is not applied and trigger matching is not required.

### 5.3.5 Investigation

Given the disagreements between data and simulation shown above a number of cross-checks were performed to understand this discrepancy, including checking for performance dependence on period, detector performance, pile-up conditions and online beamspot position. In this section, I summarise the results of the investigation and our understanding of the  $b$ -trigger performance in 2016 data. For this, the set-up as described in 5.3.3 is used

---

<sup>4</sup>Specifically HLT\_mu26\_imedium, HLT\_e26\_tight\_iloose and HLT\_e26\_ltight\_iloose.

with the exception that the  $b$ -jet aware GRL is not applied to allow us to see the problems clearly.

The major problem that was discovered to be causing the large discrepancies was related to primary vertex finding. As described above, in 2016 data an algorithm known as `xPrmVtx` was used to find the primary vertex. It has since been uncovered that there was a bug in the code used to implement this algorithm; effectively different co-ordinates were used by different components of the code. Online tracks passed to `xPrmVtx` use position with respect to online beam-spot position, where the `xPrmVtx` algorithm assumed track position with respect to the origin. This means that when the online beamspot  $z$ -position is far from the origin, a dummy vertex with position at the origin is passed to the  $b$ -tagging algorithms. This leads to sub-optimal performance, as will be shown below. For ease of reading online beamspot  $z$ -position is henceforth referred to as  $z_{bs}^{online}$ .

The exact setup for the  $b$ -jet trigger has changed as data has been taken, to respond to performance issues as they are noticed and patches are applied. As such the relevant conditions of the  $b$ -jet trigger can be split into three regions of data-taking, which I will refer to as epochs. The effect of `xPrmVtx` returning a dummy vertex on  $b$ -jet trigger performance is different in each of these epochs, the details are summarised Table 5.1. As a result of these differences in trigger performance, each epoch is now considered independently.

Epoch	Runs	Periods	Effect if no <code>xPrmVtx</code> PV is found
1	296939- 300571, 300655	A,B(part)	An invalid vertex is passed to the online b-tagging
2	300600, 300784-308084	B(part),C,D,E,F,G,I,J	The $b$ -jet trigger is not fired
3	309331-311481	K,L	A back-up primary vertex finding algorithm is used.

**Table 5.1:** A table describing the effect of not finding a valid `xPrmVtx` primary vertex on different epochs of data.

Firstly let us consider Epoch 1; Figure 5.3(a) shows that efficiency against jet- $p_T$  is 80-90% of that in simulation, similar to that shown in the previous section. However, Fig-

ure 5.3(b) shows that  $\varepsilon_{b\text{Trig}}$  in Epoch 1 has a strong dependence of  $z_{bs}^{\text{online}}$ ; when  $z_{bs}^{\text{online}}$  is close to zero  $\varepsilon_{b\text{Trig}}$  in data and simulation are comparable<sup>5</sup> but as  $|z_{bs}^{\text{online}}|$  increases efficiency falls off steeply. To understand this performance the variable ‘vertex class’ is studied, which is defined as 0 when a valid `xPrmVtx` vertex is found and 1 if not. Figure 5.4(a) shows that when an `xPrmVtx` vertex is found  $\varepsilon_{b\text{Trig}}$  is reasonably high ( $\sim 0.8$ ) and is comparable between data and simulation (within 5%), whilst if no valid `xPrmVtx` vertex is found then efficiency is very low in both simulation and data. However, Figure 5.4(b) shows that a valid `xPrmVtx` vertex is found in simulation in  $> 99\%$  of the jets, whilst in data there is  $\sim 16\%$  of events where no valid `xPrmVtx` vertex is found. Hence, combining the information in Table 5.1, Figure 5.3 and Figure 5.4 it can be concluded that in Epoch 1 in events where the  $|z_{bs}^{\text{online}}|$  is far from 0 then `xPrmVx` returns an dummy vertex which results in a low  $\varepsilon_{b\text{Trig}}$ , explaining the data/simulation differences in Epoch 1.

---

<sup>5</sup>In simulation the  $z_{bs}^{\text{online}}$  is always set to zero.

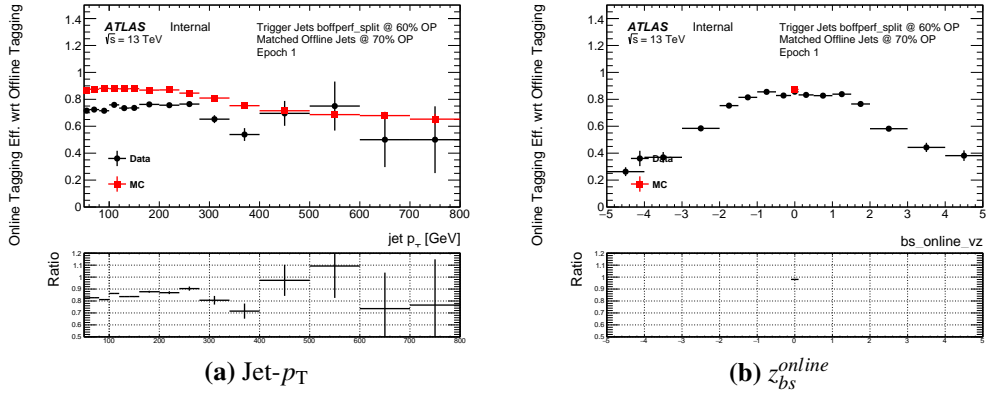


**Figure 5.3:** The 60%  $b$ -jet trigger efficiency with respect to an offline 70% operating point tag for data from Epoch 1 (black) and simulation (red) against jet- $p_T$  (a) and online beamspot  $z$ -position (b). The  $b$ -jet trigger aware GRL has not been applied.

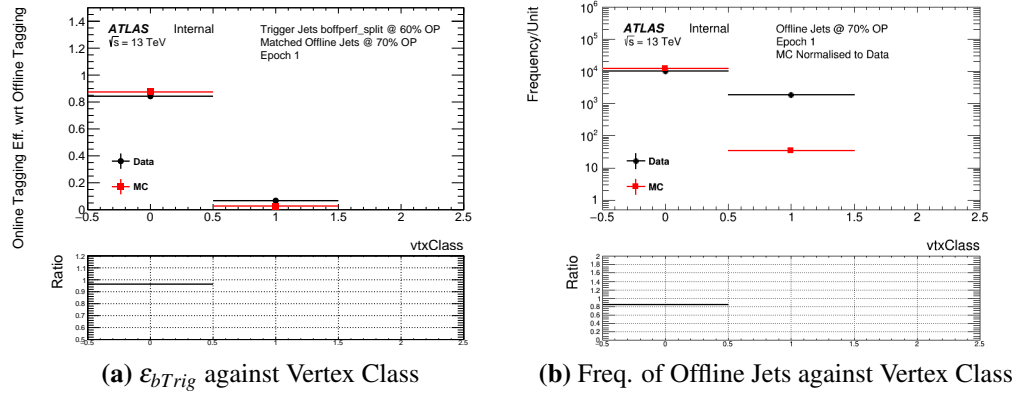


**Figure 5.4:** (a) The 60%  $b$ -jet trigger efficiency with respect to an offline 70% operating point tag and (b) the number of offline jets passing 70% operating point tag and matching a HLT trigger jet against vertex class for data from Epoch 1 (black) and simulation (red). The  $b$ -jet trigger aware GRL has not been applied.

In Epoch 2, there is a similar problem to Epoch 1, but there is a subtle difference which requires us to look at this region in a different way. As in Epoch 1, when  $z_{bs}^{online}$  is far from zero then a  $xPrmVtx$  PV is not found. However in Epoch 2 this means that the  $b$ -jet trigger was discovered to falsely terminate whilst processing the event, meaning that there are no online  $b$ -jets available in the event, and therefore the trigger will not fire. However, the additional complication compared to Epoch 1 is this means that the  $b$ -perf triggers used to measure the efficiency are also not fired when no valid  $xPrmVtx$  PV is available. Hence, measuring  $\epsilon_{bTrig}$  using the set-up as described will not capture the cases where a valid  $xPrmVtx$  PV is found and thus  $\epsilon_{bTrig}$  should be consistent in data and simulation; Figure 5.5 shows that the  $\epsilon_{bTrig}$  measured in data to be in agreement with

simulation within 5%.

For Epoch 2, in addition to measuring  $\varepsilon_{bTrig}$  it is necessary to also account for the cases when a false  $xPrmVtx$  PV is found. This is done by measuring the  $b$ -perf efficiency,  $\varepsilon_{bPerf}$ , the efficiency that there is a valid primary vertex in the event.  $\varepsilon_{bPerf}$  is calculated by dividing the number of events that pass the trigger `HLT_mu26_imedium_2j35_bperf` by the number that pass the trigger `HLT_mu26_imedium`, such that the denominator has no  $b$ -trigger dependency so is unaffected by  $xPrmVtx$  PV. This is an event level quantity and as such is measured with respect to other event level quantities, such as leading jet- $p_T$ . Figure 5.6 shows that:  $\varepsilon_{bPerf}$  has a data/simulation ratio of around 80% which is similar to that in Section 5.3.4 and  $\varepsilon_{bPerf}$  shows similar behaviour with respect to  $z_{bs}^{online}$  as observed in Epoch 1. Finally it is observed that  $\varepsilon_{bPerf}$  has a lower efficiency at smaller values of absolute leading jet- $\eta$ ; this is due to the fact that at high- $\eta$  tracks have a larger error on the longitudinal impact parameter,  $z_0$ , meaning that the mis-match of co-ordinates can in the  $xPrmVtx$  algorithm is covered by the errors, mitigating this issue. This effect must be accounted for in the final efficiency measurement.**This last two sentances are dodgy**

Epoch 3, when no  $xPrmVtx$  PV is found then a backup PV finding algorithm is used, known as `EFHist`, which finds the PV through a basic histogramming of the tracks, the simplicity of the algorithm means that a PV can be found as long as 1 track is present. Figure 5.7 shows  $\varepsilon_{bTrig}$  for Epoch 3 for jet- $p_T$ , jet- $\eta$ ,  $z_{bs}^{online}$  and vertex class (as defined above). In Epoch 3  $\varepsilon_{bTrig}$  measured in data is within 5% of simulation and there is no shape difference between the two with respect to jet- $\eta$ . In addition it is shown that in Epoch 3 there is no strong dependence on  $z_{bs}^{online}$ , and that efficiency in data is consistent if a valid  $xPrmVtx$  vertex or not (vertex class = 0 or 1 respectively). This demonstrates the success of the backup vertex approach.

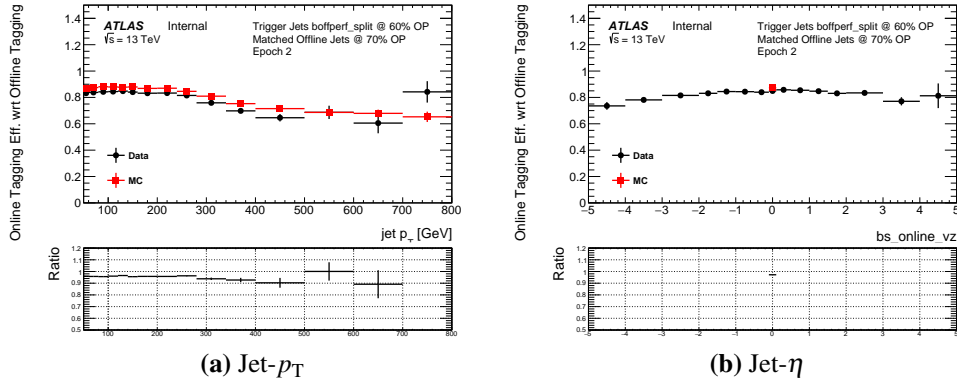


**Figure 5.5:** The 60%  $b$ -jet trigger efficiency with respect to an offline 70% operating point tag for data from epoch 2 (black) and simulation (red) against jet- $p_T$  (a), jet- $\eta$  (b) and online beamspot  $z$ -position (c).

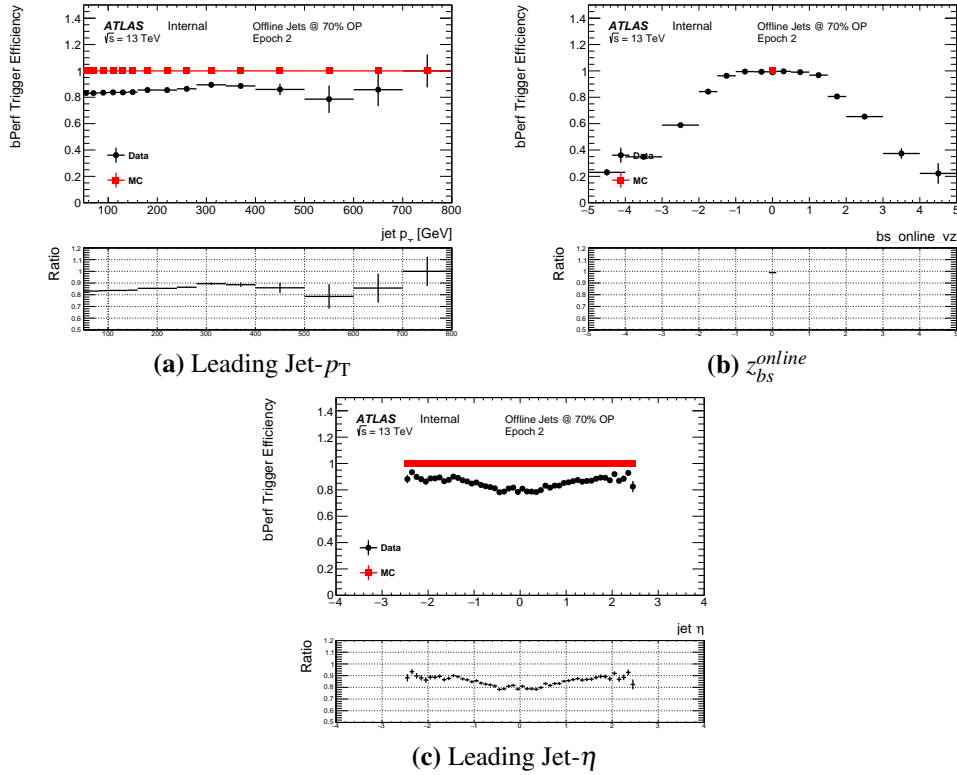


**Figure 5.6:**  $b$ -perf efficiency,  $\varepsilon_{bPerf}$ , for data from Epoch 2 (black) and simulation (red) against leading-jet  $p_T$  (a), online beamspot  $z$ -position (b) and leading jet- $\eta$  (c).

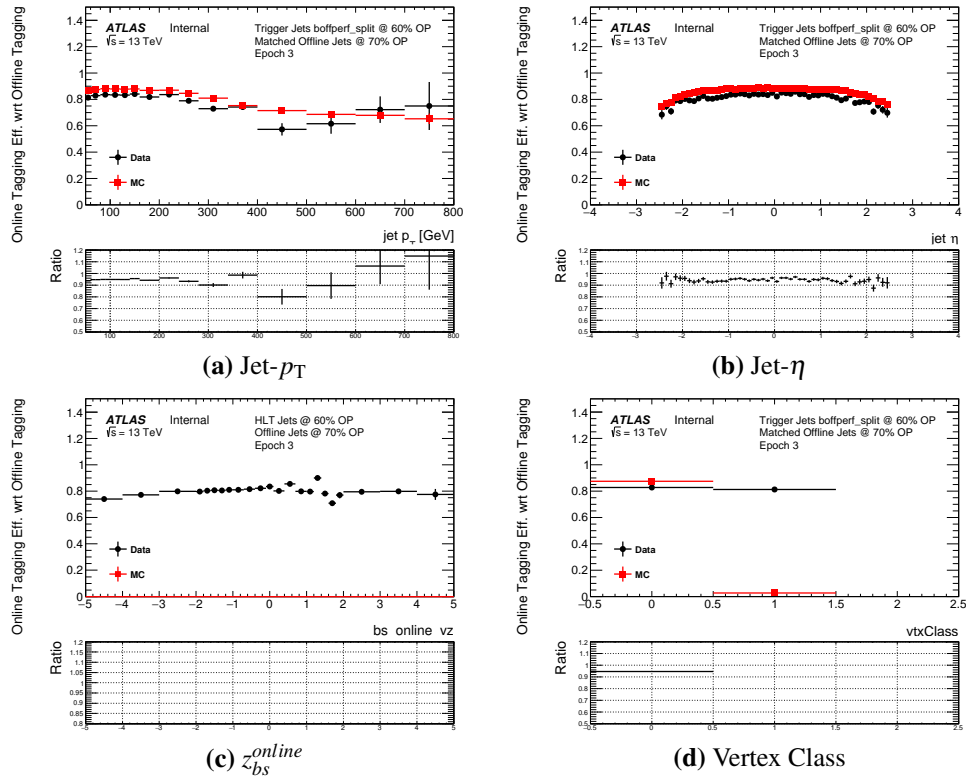


**Figure 5.7:** The 60%  $b$ -jet trigger efficiency with respect to an offline 70% operating point tag for data from Epoch 3 (black) and simulation (red) against (a) jet- $p_T$ , (b) jet- $\eta$ , (c) online beamspot  $z$ -position and (d) vertex class.

### 5.3.6 Solution: $b$ -Jet Trigger GRL

To summarise, in the previous section it is shown that at large values of absolute online beamspot  $z$ -position the measured  $\varepsilon_{bTrig}$  in Epoch 1 and  $\varepsilon_{bPerf}$  in Epoch 2 is lower in data than in MC, due to poor `xPrmVtx` PV finding performance. In Epoch 3 there is reasonable data/simulation agreement due to the use of a backup vertex finding algorithm.

The solution employed is to apply a  $b$ -jet trigger aware GRL that removes events with an absolute  $z_{bs}^{online}$  greater than 2mm in Epoch 1 and 2, such that the events with low efficiency are removed. The cost of this approach is the luminosity of our data-set is reduced, specifically the data-set falls from  $32.9 \text{ fb}^{-1}$  to  $24.3 \text{ fb}^{-1}$ . However there are three key reasons why use of a  $b$ -jet trigger GRL was chosen over simply applying an overall efficiency. Firstly, as there is no beamspot position distribution in simulation it is not clear that kinematics of events at high  $z_{bs}^{online}$  can be well understood and modelled; the sculpting of the efficiency with respect to jet- $\eta$  is an example of this. Secondly, the efficiencies are quite low at high beamspot  $z$ -position, so the loss in luminosity  $\times$  acceptance is relatively small and finally the use of a GRL means a more realistic estimate of the actual luminosity used in an analysis is used.

For the choice of which value of beamspot  $z$  position to use for in the GRL, it was required to select the widest cut where the efficiency had not significantly declined, such that as much luminosity as possible is retained while removing most of the affected region. This 2 mm cut was chosen from examining Figure 5.3(b) and Figure 5.6(b) and from studying a variety of cuts from 2 mm to 1 mm.

After the GRL is applied,  $\varepsilon_{bTrig}$  for Region 1 becomes approximately 90-95% of the efficiency measured in simulation, as shown in Figure 5.8, and  $\varepsilon_{bPerf}$  for Region 2 becomes approximately 95% of the efficiency measured in simulation, as shown in Figure 5.9.

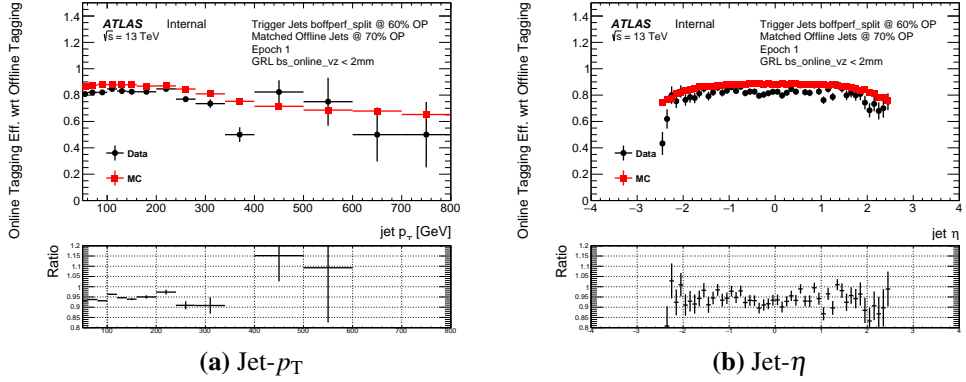


**Figure 5.8:** The 60%  $b$ -jet trigger efficiency with respect to an offline 70% operating point tag for data from Region 1 (black) and simulation (red) against jet- $p_T$  (a) and jet- $\eta$  (b). The  $b$ -jet trigger aware GRL has been applied.

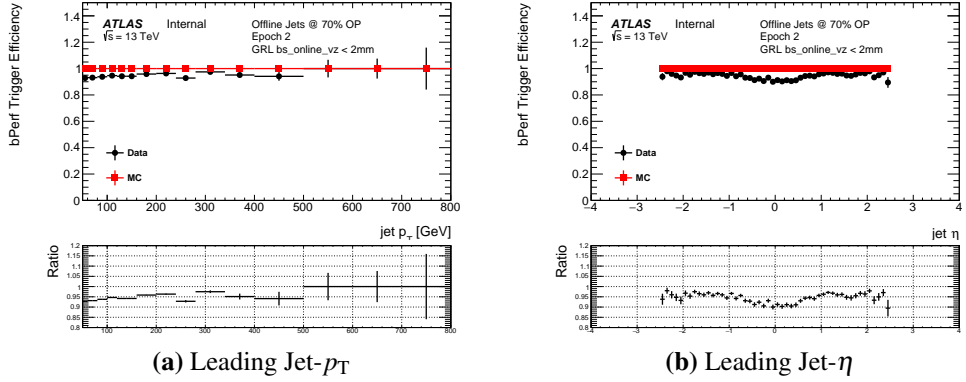


**Figure 5.9:**  $b$ -perf efficiency,  $\varepsilon_{b\text{Perf}}$ , for data from Region 2 (black) and simulation (red) against leading (a) jet- $p_T$  and (b) jet- $\eta$ . The  $b$ -jet trigger aware GRL has been applied.

Figures 5.10 and 5.11 shows measured  $\varepsilon_{b\text{Perf}}$  and  $\varepsilon_{b\text{Trig}}$  for the full 2016 data-set, combining Regions 1, 2 and 3, with the  $b$ -jet trigger aware GRL applied. This represents the raw observed data/simulation efficiencies when the full event selection has been applied.

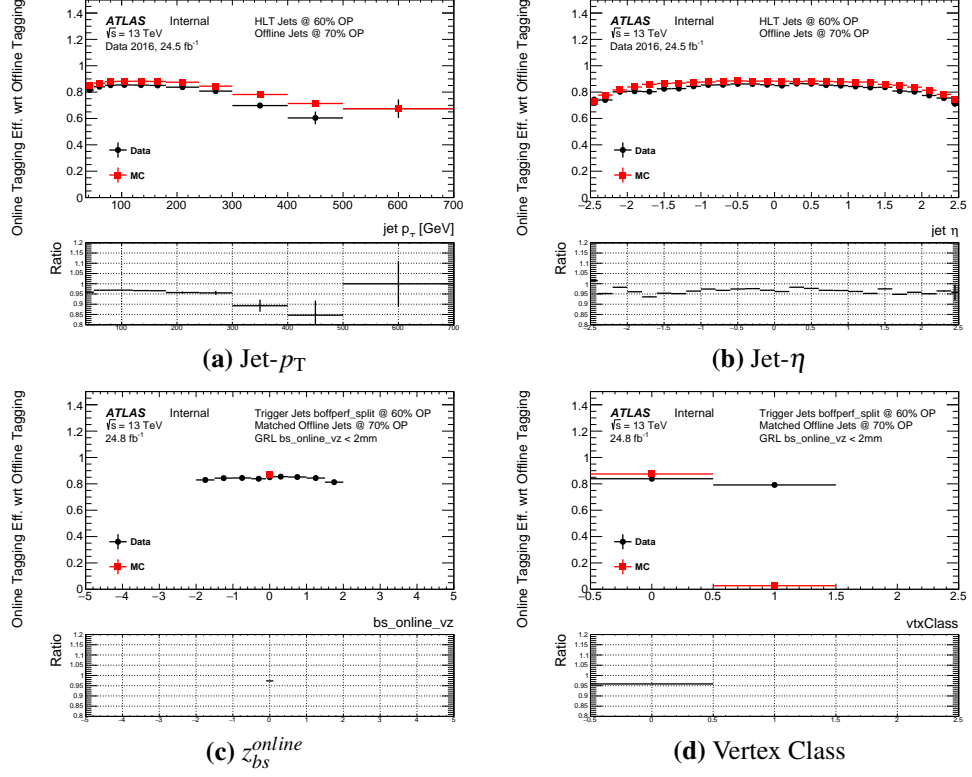


**Figure 5.10:** The 60%  $b$ -jet trigger efficiency with respect to an offline 70% operating point tag for the full 2016 data-set (black) and simulation (red) against jet- $p_T$  (a), jet- $\eta$  (b), online beamspot  $z$ -position (c) and vertex class (d).

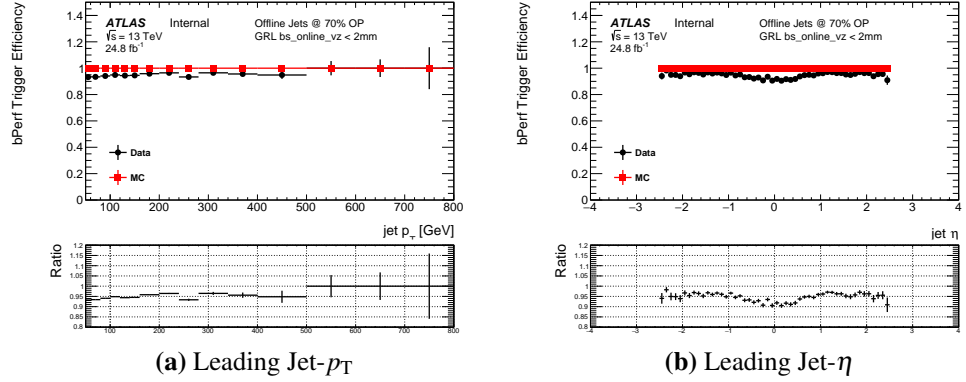


**Figure 5.11:**  $b$ -perf efficiency,  $\epsilon_{bPerf}$ , for the full 2016 data-set (black) and simulation (red) against (a) leading jet- $p_T$  and (b) jet- $\eta$ . The  $b$ -jet trigger aware GRL has been applied.

### 5.3.7 Efficiency Measurement and Systematic Derivation

In the previous two sections it has been shown that when applying a  $b$ -jet aware GRL, the  $b$ -jet trigger performance is understood and the data/simulation agreement is within 5%. In this section the measurement of data efficiency, data/simulation scale factors (SFs) and

associated systematics to account for the 5% are described.

As discussed above, there are two factors considered in this section. Firstly there is the  $\varepsilon_{bTrig}$  measurement that accounts for differences in online and offline  $b$ -tagging given that a valid primary vertex has been found. Sections 5.3.7.1 to 5.3.7.3 describes the derivation of a set of systematics and corrections to the raw measurement and Section 5.3.7.4 presents the final measurement, which is applied as a jet-level efficiency in the final analysis. Secondly, in Section 5.3.7.5, is a description the measurement of the  $\varepsilon_{bPerf}$  that accounts for the efficiency of finding a valid primary vertex and the relevant systematics, which is applied as an event level efficiency.

In this section describing the final measurement, the full 2016 data set is used, the simulated  $t\bar{t}$  sample includes single-top processes and the full event selection from Section 5.3.3 is applied.

### 5.3.7.1 Purity Error

It is known that despite the strict event selection there will inevitably be non  $b$ -jet contamination in our sample. To estimate the  $b$ -jet purity simulation is used, where the true flavour of the jet is available. Jets are categorised as true  $b$ -jets, meaning that a  $B$ -hadron was found within a cone of  $R = 0.4$ , or true non- $b$ -jets if not. Then distributions for inclusive jets to the truth matched  $b$ -jets in the simulation sample are compared. Figure 5.12 shows the  $b$ -jet purity for jet- $p_T$  and jet- $\eta$ ; showing that the  $b$ -jet purity is  $> 95\%$  up to jet- $p_T \sim 300$  GeV and  $> 90\%$  for higher values of jet- $p_T$ .

To estimate the effect of these impurities on the efficiency measurement simulation is again used. Firstly, the efficiency in our nominal inclusive simulation is compared to the efficiencies if only true- $b$ -jets or true non- $b$ -jets are selected, this is shown in Figure 5.13(a). The ratio is applied as a correction to the final efficiency measurement. Then any mismodelling of the  $b$ -jet fraction in simulation is also considered, to account for this the efficiency for the simulated inclusive sample is compared to the efficiency when the non  $b$ -jet content has been doubled, as shown in Figure 5.13(b). The maximum difference from the efficiency measured in the inclusive simulated sample and the cases where there is only true  $b$ -jets and where the non  $b$ -jet content has been doubled, shown in the two ratio plots in Figure 5.13,

is taken as a symmetric systematic.

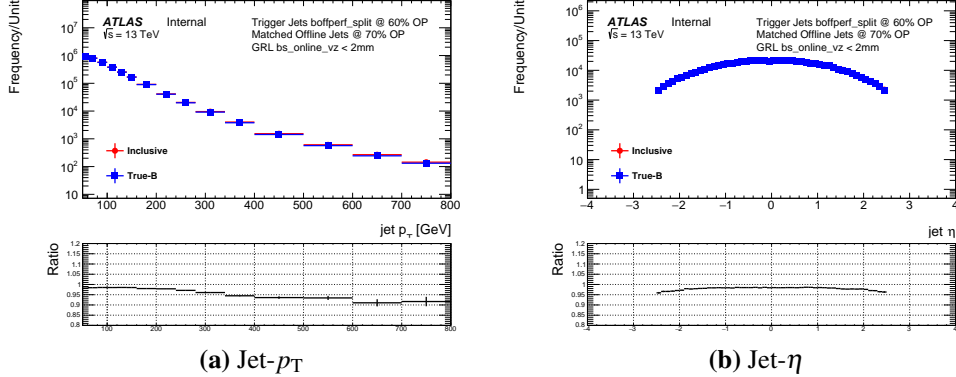


**Figure 5.12:** A comparison of offline jets tagged at the 70% operating point for inclusive jets (red) and truth-matched  $b$ -jets (blue) against jet- $p_T$  (a) and jet- $\eta$  (b) in a simulated  $t\bar{t}$  sample.

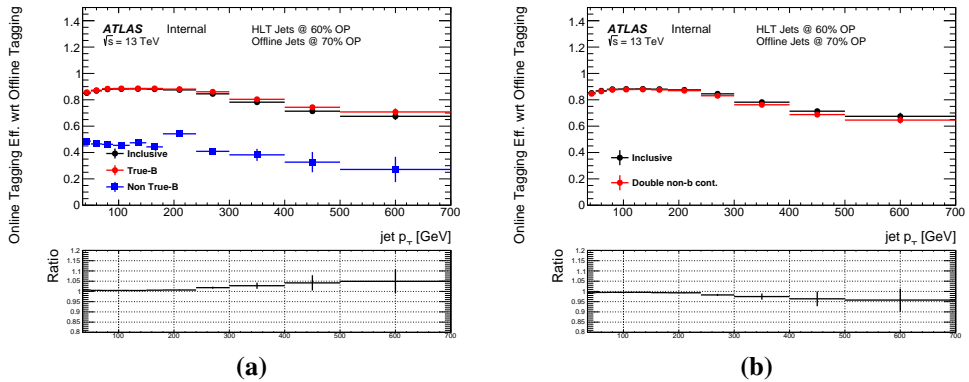


**Figure 5.13:** The 60%  $b$ -jet trigger efficiency with respect to an offline 70% operating point tag for inclusive jets (black) compared to truth matched  $b$ -jets and non  $b$ -jets (a) and the case where non  $b$ -jet content has been doubled (b) for a simulated  $t\bar{t}$  sample. The lower panel in both plots show the ratio to the inclusive efficiency.

### 5.3.7.2 Non- $b$ -jet trigger efficiency error

As one would expect and as shown in left plot of Figure 5.13, non  $b$ -jets (shown in blue) have a different  $b$ -jet trigger efficiency to that of  $b$ -jets. However the exact efficiency is not known well and could be miscalculated in simulation. To account for this uncertainty the nominal efficiency in simulation is compared to the cases where the non- $b$ -jet efficiency has been halved and doubled in simulation, as shown in Figure 5.14. When doubling the non- $b$ -jet trigger efficiency this is limited at the upper end to being no greater than the true  $b$ -jet trigger efficiency. The maximum bin-by-bin difference between the nominal and the two cases, as shown in the two ratio plots, is taken as a systematic.

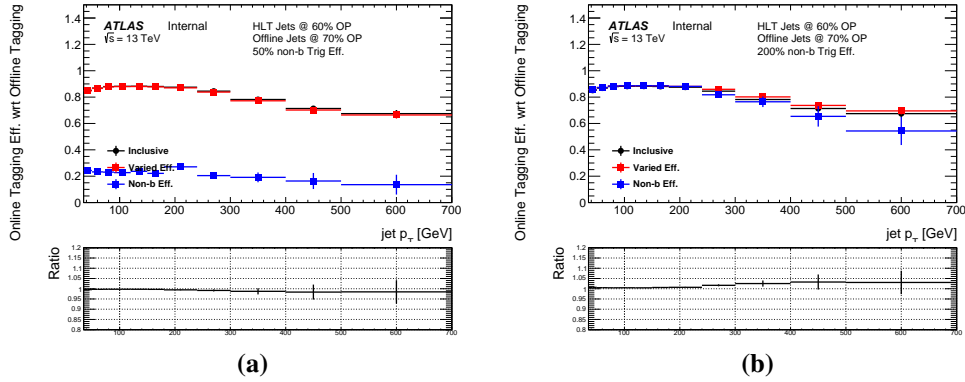


**Figure 5.14:** The 60%  $b$ -jet trigger efficiency with respect to an offline 70% operating point tag for nominal inclusive case (black) compared to varied inclusive case (red) and just non  $b$ -jets (blue) in the case where non  $b$ -jet efficiency has been halved (a) and doubled (b) for a simulated  $t\bar{t}$  sample. The lower panel in both plots show the ratio of the varied inclusive efficiency to the nominal inclusive efficiency.

### 5.3.7.3 High- $p_T$ extrapolation

Measuring  $b$ -jet trigger efficiency for high- $p_T$  jets is limited by the statistics in the simulated  $t\bar{t}$  sample, so the shape from simulation will be used to extrapolate the efficiency for jet- $p_T > 240 \text{ GeV}$ . The point from which to extrapolate from was chosen as this is when data statistic error starts to become large.

The procedure is made of two sequential fits (normalisation and correction) to the data/simulation ratio, which are used to create a “corrected simulation”  $\varepsilon_{bTrig}$  distribution. For jet- $pT > 240 \text{ GeV}$ , the corrected  $\varepsilon_{bTrig}$  is used in place of data when measuring the data  $\varepsilon_{bTrig}$  efficiency and when calculating data/MC scale factors. A final quadratic fit is used to assign a systematic.

In more detail:

- **Flat Normalisation Fit:**

The measured  $\varepsilon_{bTrig}$ , in both data and simulation are compared, and a horizontal fit is performed to the ratio of the two. The fit range is set at  $p_T > 50 \text{ GeV}$  to discount the first bin, which has a larger purity uncertainty. This is then used to normalise the simulated efficiency distribution to match data. This fit is shown in the lower plot of panel (a) in Figure 5.15. The error on the one parameter of this fit is taken as a systematic error.

- **Linear Correction Fit:**

The measured  $\varepsilon_{bTrig}$ , in both data and the normalised simulation are compared, and a linear fit is performed to the ratio of the two from jet- $p_T > 240$  GeV. This is then used to correct the simulated efficiency distribution to match data. This fit is shown in the lower plot of panel (b) in Figure 5.15. The simulated  $\varepsilon_{bTrig}$ , after both the normalisation and linear correction is referred to as the corrected simulation. To assign a systematic on the fit parameters, the slope of this fit is varied up and down within errors, whilst the point at which the fit crosses 1 is kept constant. The maximum difference between the nominal fit and the varied fits is taken as the error on the linear correction fit. Panel (c) of Figure 5.15 shows the data compared to the corrected simulation. The lower panel shows the ratio of the two, and the blue lines represent the errors on the linear correction fit.

- **Quadratic Systematic Fit:**

Finally to assess an error on the choice of a linear fit as the functional form above, a fit is performed to the data and corrected simulation ratio using a quadratic function. This ratio and the fit is shown in panel (d) of Figure 5.15. The difference of the fit from 1 is considered as the functional form error when assigning as systematic.

The systematic error on the extrapolation is defined as the error from normalisation fit added to the bin-by-bin maximum of the error from the linear correction fit and the error from the quadratic systematic fit. The errors on the high- $p_T$  extrapolation procedure are summarised in Table 5.2

Jet $p_T$ [GeV]	MC Extrapol. Error (%)	Norm Fit Err. (%)	Lin. Fit (%)	Quad. Fit (%)
240.0-300.0	0.8	0.0	0.8	0.3
300.0-400.0	4.0	0.0	2.9	4.0
400.0-500.0	5.6	0.0	5.6	1.7
500.0-700.0	18.0	0.0	9.6	18.0

**Table 5.2:** A table showing the systematic assigned for the high- $p_T$  extrapolation.

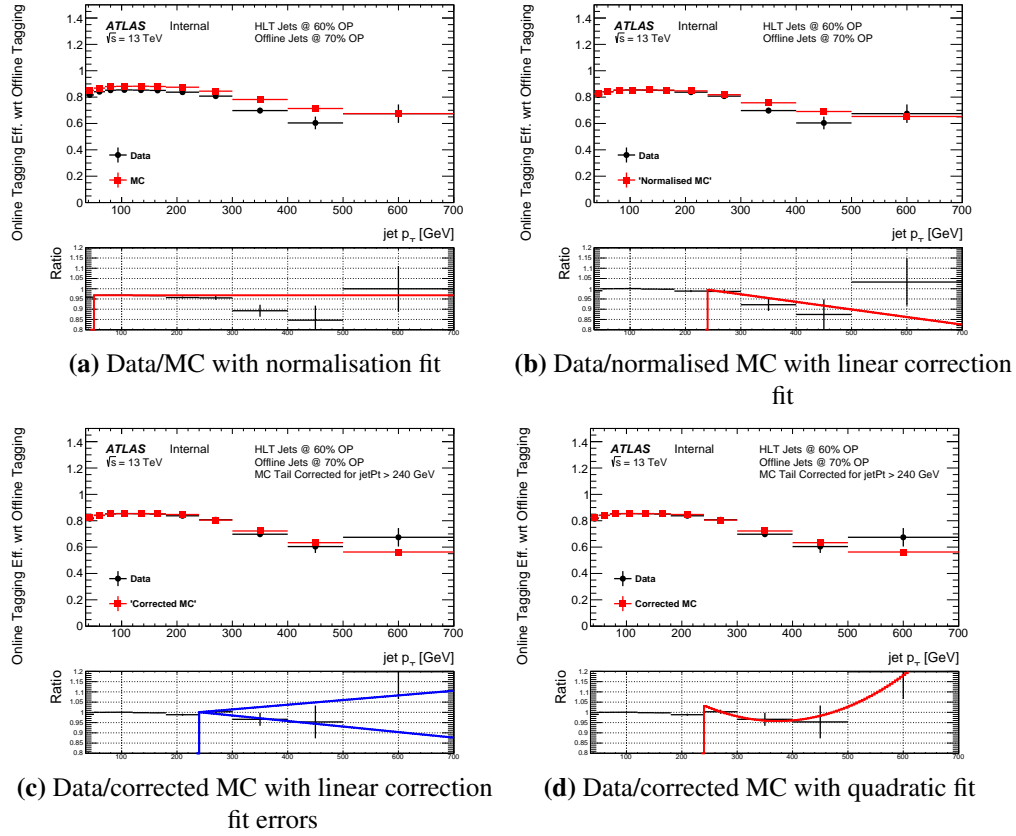


**Figure 5.15:** A figure to demonstrate the high- $p_T$  extrapolation procedure for the 60%  $b$ -jet trigger efficiency with respect to an offline 70% operating point tag. Data (black) is compared against simulation (red) after various corrections have been applied as a function of jet- $p_T$ . Panel (a) shows the the flat normalisation fit uncorrected simulation, panel (b) shows the linear correction fit to normalised simulation, panel (c) shows the linear correction fit errors to the corrected simulation and panel (d) shows the quadratic fit to the corrected simulation.

### 5.3.7.4 Jet-Level Efficiency and Scale Factor Measurement

Now the raw measurements of  $\epsilon_{bTrig}$  from Figure 5.10 and the additional corrections and systematics described above can be brought together. In Figure 5.10 it is shown that, whilst  $\epsilon_{bTrig}$  does depend on jet- $\eta$ , the data to simulation ratio is flat with respect to jet- $\eta$ . However there is no significant dependence on jet- $p_T$  hence data/simulation scale factors are derived as a function of only jet- $p_T$ .

The full jet-level  $\epsilon_{bTrig}$  measurement is shown in Figure 5.16. For use in combination with the simulation, a data/simulation scale factor as a function of jet- $p_T$  is also derived and will be applied at the jet-level, which is also shown in Figure 5.17.

The errors considered for the jet-level efficiency account for: mismodelling of the b-jet purity in simulation, mismodelling of the b-jet trigger efficiency for non b-jets, simulation statistical error , data statistical error ( $\text{jet-}p_T < 240 \text{ GeV}$ ) and simulation based extrapolation ( $\text{jet-}p_T > 240 \text{ GeV}$ ). Table 5.3 summarises the errors on the jet-level scale factor. These errors are taken as a symmetric error in each jet- $p_T$  bin and the scale factors are applied to each b-tagged jet.

As a final sanity check Figure 5.18 shows  $\varepsilon_{b\text{Trig}}$  measured in data to that from the corrected simulation, in the lower panel a ratio of data to corrected simulation is shown and the extrapolation and total errors are overlaid in red and green respectively. The derivation of the corrected simulation and associated extrapolation errors is described in Section 5.3.7.3 This shows that the corrected simulation lies within the total errors for the whole range of jet- $p_T$  and at high- $p_T$ , as one might expect, the error is dominated by the extrapolation uncertainties. Note that the corrected simulation is only used to represent data for jet- $p_T > 240 \text{ GeV}$ .

Jet $p_T$ [GeV]	SF	Total Err. (%)	Stat. (%)	Extrap. (%)	Pur. (%)	L. Trig. Eff. (%)
35.0-50.0	95.9	1.0	0.1	-	0.7	0.7
50.0-70.0	96.8	0.7	0.1	-	0.5	0.5
70.0-90.0	96.9	0.6	0.1	-	0.5	0.5
90.0-120.0	96.9	0.7	0.1	-	0.5	0.5
120.0-150.0	96.7	0.6	0.2	-	0.4	0.4
150.0-180.0	96.6	0.9	0.2	-	0.6	0.6
180.0-240.0	95.7	1.1	0.5	-	0.7	0.7
240.0-300.0	95.3	2.6	0.4	0.8	1.8	1.7
300.0-400.0	92.4	5.6	1.1	4.0	2.8	2.5
400.0-500.0	88.8	8.1	2.6	5.6	4.2	3.3
500.0-700.0	83.4	19.4	4.0	18.0	4.9	3.1

**Table 5.3:** A table showing the jet-level Data/simulation scale factor (SF) as a function of jet- $p_T$  with total error and the contributions of the different systematics considered; specifically statistical, high- $p_T$  extrapolation, non- $b$ -jet purity and non- $b$ -jet trigger efficiency.

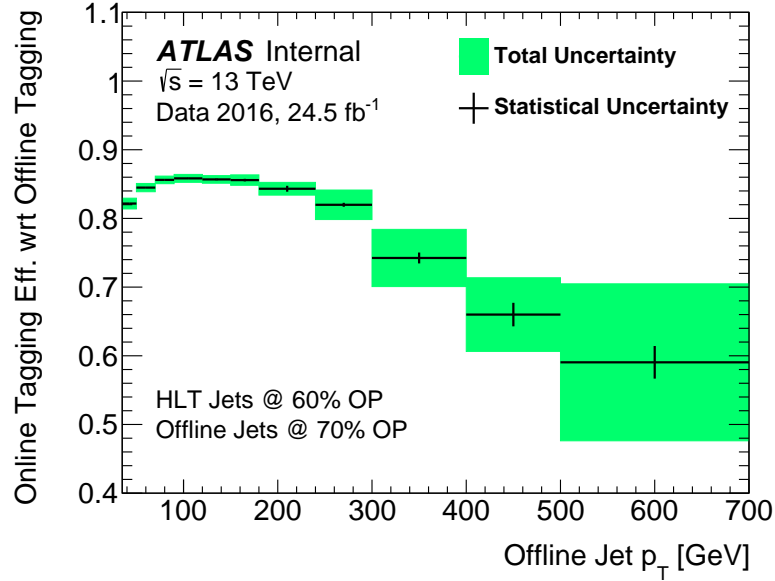


**Figure 5.16:** The measured 60%  $b$ -jet trigger efficiency with respect to an offline 70% operating point tag as measured in data as a function of offline jet- $p_T$ . The central values are shown in black with the statistical error and the green bands represent the total error including systematic errors.

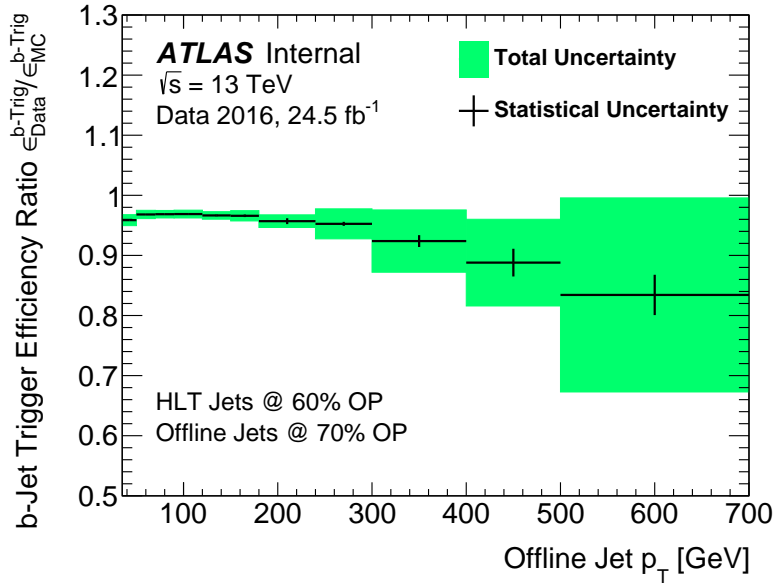


**Figure 5.17:** Data/simulation scale factors for the 60%  $b$ -jet trigger efficiency with respect to an offline 70% operating point tag as a function of offline jet- $p_T$ . The central values are shown in black with the statistical error and the green bands represent the total error including systematic errors.

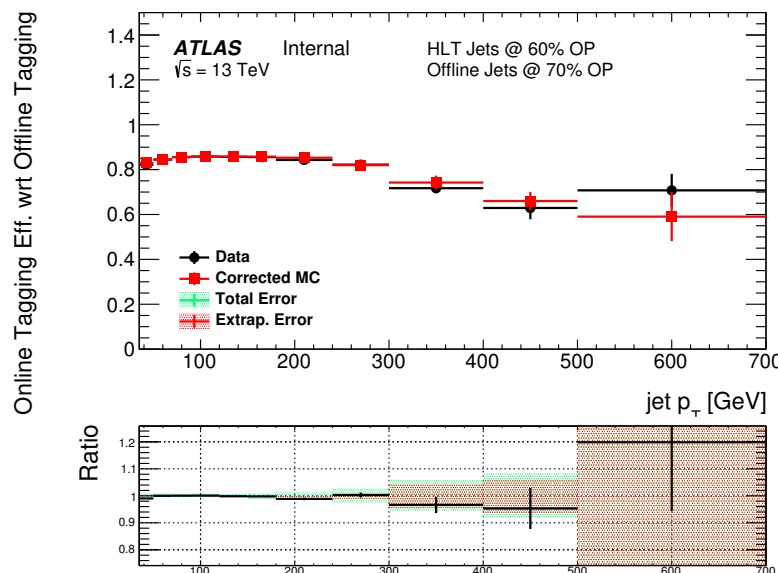


**Figure 5.18:** The measured 60%  $b$ -jet trigger efficiency with respect to an offline 70% operating point tag as measured in data (black) and from the corrected simulation (red) as a function of offline jet- $p_T$ . In the ratio plot on the lower panel the extrapolation errors is represented by the red band, whilst the total error is overlaid in green.

### 5.3.7.5 Event-Level Efficiency and Systematic

As already discussed, in some regions of data-taking the performance  $b$ -jet trigger efficiency itself depends on the online beamspot position. Hence, a  $b$ -jet trigger aware GRL is applied to remove a large fraction of events where poor  $b$ -jet trigger performance is observed.

However, even after the application of this GRL, there remains a bias with respect to leading jet- $\eta$  in the probability of finding a valid primary vertex, which is notated as  $\epsilon_{b\text{Perf}}$ . This bias is shown in Figure 5.11. This efficiency is measured differently in each epoch, in Epoch 1 it can be found as the number of events with vertex class = 0 divided by the number of events, in Epoch 2 it is defined as the dividing the number of events that pass the trigger `HLT_mu26_imedium_2j35_bpervf` by the number that pass the trigger `HLT_mu26_imedium` and in Epoch 3, due to the back-up vertex. It should be noted that this measurement made in each of the three regions separately and is then combined with each region weighted by its luminosity.

The value of  $\epsilon_{b\text{Perf}}$  is extremely close to 1 in simulation, in this case the efficiency in data and the scale factor are the same. To assign a systematic for this correction the statistical error in data and simulation in addition to a shape systematic are used. The shape systematic, to account for possible variations of the shape with respect to jet- $\eta$ , is defined as half of the difference between the maximum efficiency and the minimum efficiency in any jet- $\eta$  bin, which effectively covers a flat distribution with respect to jet- $\eta$  to one where the shape is twice as extreme as observed.

Table 5.4 and Figure 5.19 summarises the event-level efficiency correction and the associated systematics.

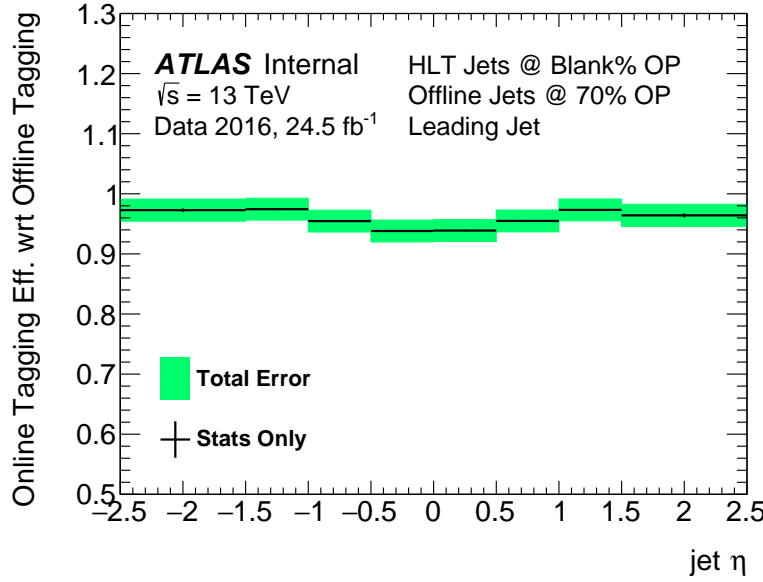


**Figure 5.19:** The measured  $\varepsilon_{bPerf}$  as measured in data as a function of offline leading jet- $\eta$ . The central values are shown in black with the statistical error and the green bands represent the total error including systematic errors.

Leading Jet $\eta$	SF	Total Error (%)	Data Stat. (%)	MC Stat. (%)	Shape Syst. (%)
-2.5–1.5	97.3	1.9	0.3	0.1	1.9
-1.5–1.0	97.4	1.9	0.1	0.0	1.9
-1.0–0.5	95.5	1.9	0.1	0.0	1.9
-0.5–0.0	93.8	1.9	0.2	0.0	1.9
0.0–0.5	93.9	1.9	0.2	0.0	1.9
0.5–1.0	95.5	1.9	0.2	0.0	1.9
1.0–1.5	97.3	1.9	0.1	0.0	1.9
1.5–2.5	96.4	1.9	0.3	0.1	1.9

**Table 5.4:** A table showing the event-level Data/MC scale factor (SF) as a function of leading jet- $\eta$  with total error and the contributions of the different systematics considered.

### 5.3.8 Cross-checks

#### 5.3.8.1 Simulation checks

- Ttbar alone vs ttbar+tW

- Try powheg

### 5.3.8.2 Electron/Muon overlap checks

### 5.3.8.3 Event Level Eff: Showing correlation with $z_{bs}^{online}$

- Show that it comes from high beamspot z-position only.
- i.e.  $\epsilon_{bPerf}$  vs eta for different bs regions.

### 5.3.8.4 Event Level Eff: Re-weighting of sub-leading jet

- We did a test where we applied correction to leading and shows the subleading was flat within systematics (2%)

Any others that are good?

Cross-checks can be moved to appendix

## 5.4 To Do

These can be considered on my list. - Cite in plot caption

- Uncertainty instead of error
- Update plots to most current version (and label those that are not)
- In caption I want (a) before plot i.e. (a) jet-pT, (b) jet-eta. - Always use data/simulation instead of data/MC
- use Epoch instead of epoch

## Chapter 6

# Di-*b*-jet Search: Outline and Event Selection

In Chapter 2 it was shown that many Beyond Standard Model theories predict new particles decaying to one or two *b*-quarks that could be produced by the LHC. Chapters 3, 4 and 5 described the detectors and reconstruction techniques used to observe such an event in the ATLAS detector. Hence, I have now outlined the motivation and the tools required to perform a search for resonances decaying to one or two *b*-jets, an analysis that is called a di-*b*-jet search.

In Chapters 6, 7 and 8 I will describe the di-*b*-jet search analysis using the ATLAS detector. Each chapter will describe a separate part of the analysis, the different parts are outlined Section 6.1. In this thesis, the di-*b*-jet analysis is performed using three different data-sets, the data-sets are described in Section 6.2.

### 6.1 Analysis Outline

The strategy used for the di-*b*-jet analysis can be split up into three parts, which form the three di-*b*-jet analysis chapters. A brief outline of the parts is given here, and full detail can be found in the relevant chapter.

- **Di-*b*-jet Event Selection:** (*Chapter 6*)

The first step is to select events that are consistent with a resonance decaying to one or two *b*-quarks. Briefly, two high-momentum jets are required and two *b*-tag categories are considered; a category in which both jets have been *b*-tagged (2 *b*-tag) and a category where at least one jet has been *b*-tagged ( $\geq 1$  *b*-tag). The remainder of the chapter will

focus on details of analysis selection; Section 6.2 will describe the data-sets used, Section 6.3 will describe the signal and backgrounds considered when defining the selections and Section 6.4 will set out the details of the event selection used for each of the data-sets.

- **Search Phase:** (*Chapter 7*)

Once events have been selected the next part of the analysis aims to determine if there is evidence of a new particle in the selected events; this step is known as the ‘search phase’. This step uses the  $m_{jj}$  spectrum, where  $m_{jj}$  is the invariant mass of the two highest  $p_T$  jets. A new particle will appear as a resonance (or ‘bump’) on the smoothly falling background  $m_{jj}$  distribution from QCD multi-jet, as illustrated in Figure 6.1. A fit function is used to model the smoothly falling QCD background and a model-independent search for resonances is performed using the BumpHunter algorithm. Chapter 7 contains a full description of the search phase strategy.

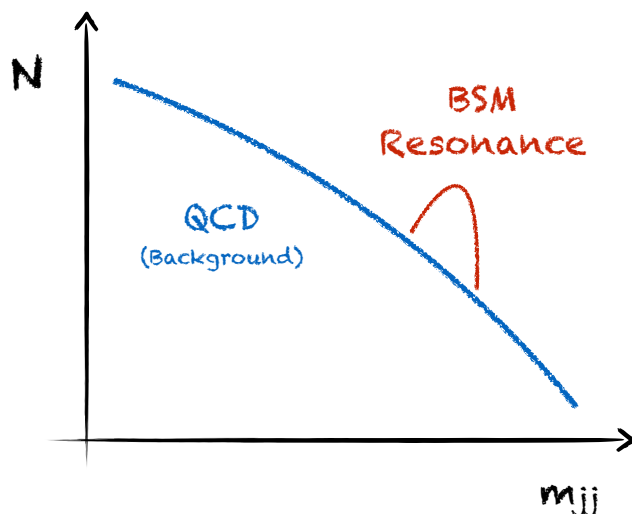


**Figure 6.1:** A cartoon illustrating the use of the dijet invariant mass ( $m_{jj}$ ) distribution in the search phase of the di- $b$ -jet analysis. Shown is the smoothly falling distribution from multijet QCD (SM) and a resonance shape caused by a Beyond Standard Model particle (BSM)

- **Limit Setting:** (*Chapter 8*)

If, in the search phase stage of the analysis, no significant evidence of signal is found then it is desirable to quantify what cross-sections can be excluded as a result. 95% confidence level limits are set on the two benchmark signals considered. Chapter 8 presents the limit-setting methodology, a description of systematics considered and the limit results for each of the data-sets considered.

## 6.2 List of Data Sets Used

The di-*b*-jet analysis is performed in several iterations as data is being collected, where each iteration uses a different data-set. This is done for two reasons; firstly it is important to know as soon as possible if there is evidence of a new resonance as this would affect the strategy of future di-*b*-jet analyses and that of other analyses at ATLAS. Secondly, this allows us to incrementally expand, adapt and improve this strategy in each iteration of the analysis.

In this thesis three different data-sets are considered by the di-*b*-jet analysis. The overall analysis strategy is the same for each data-set, so the iterations are described together. However, there are some significant differences in the details; as such the during the analysis description it will be clearly labelled which data-set is being referred to.

For any data-set a Good Run List (GRL) is applied to remove events of low data-quality, which is typically because an element of the detector was not operating optimally. For example, data-taking periods where the inner-most layer of the inner detector, the IBL, was not operating are removed as this data-taking period had a lower *b*-tagging performance. A GRL is applied to all data-sets considered in this analysis.

The data-sets are listed below, the trigger used in each data-set is described. All quoted luminosities are given after the GRL has been applied.

- **Summer16+15:**

The Summer16+15 data-set contains 13 TeV  $pp$  collision data collected between January 2015 to July 2016 which has an integrated luminosity  $13.3 \text{ fb}^{-1}$ . The trigger used in this data-set, known as `HLT_j380`, requires a trigger-level jet with  $p_T > 380 \text{ GeV}$ <sup>1</sup>. The analysis on this data-set has been published as a conference note [81].

- **Full16+15\_HighMass:**

The Full16+15\_HighMass data-set contains 13 TeV  $pp$  collision data collected between January 2015 to December 2016, which has an integrated luminosity of  $36.1 \text{ fb}^{-1}$ . The trigger used in this data-set, known as `HLT_j380`, requires a trigger-level jet with  $p_T > 380 \text{ GeV}$ <sup>2</sup>. The analysis on this data-set has yet to be published.

---

<sup>1</sup> Further details of single-jet triggers is in Section 5.1.

<sup>2</sup> Again, see Section 5.1 for details on single-jet triggers.

- **Full16\_LowMass:**

The Full16\_LowMass data-set contains 13 TeV  $pp$  collision data collected between January 2016 to December 2016, which has an integrated luminosity of  $24.3 \text{ fb}^{-1}$ . The trigger used in this data-set is known as a double  $b$ -jet trigger which requires two trigger-level jets with  $p_T > 150 \text{ GeV}$  and  $p_T > 50 \text{ GeV}$  where both jets have been  $b$ -tagged at the trigger level<sup>3</sup>. The Full16\_LowMass uses a  $b$ -jet trigger as the lower  $p_T$  thresholds allow the analysis to probe a lower range of  $m_{jj}$ . This analysis does not include data from 2015 which was collected using a significantly different  $b$ -jet trigger configuration. The Full16\_LowMass uses a  $b$ -jet trigger aware GRL which additionally removes periods of data where the  $b$ -jet trigger was performing in a sub-optimal way, the GRL is described in Section 5.3.6. As a double  $b$ -jet trigger is used only the 2  $b$ -tag category is considered. The analysis on this data-set has yet to be published.

### 6.3 Backgrounds and Signal

In the di- $b$ -jet analysis selection we consider two benchmark signal models and one background which is dominant. The signal models and dominant background are used to optimise event selection, so I will describe the signal and backgrounds considered here.

For both the background and the signal models Monte-Carlo simulation of the processes is produced. All the Monte-Carlo simulation is produced using the PYTHIA8 [82] generator, the EVTGEN package [80] is used for the decays of the  $B$  and  $C$  hadrons, the A14 parameter set [83] is used to model the parton shower, hadronisation and underlying event, and the NNPDF23LO PDF set [84] is used to describe the Parton Distribution Function. The detector response is modelled using the ATLAS detector simulation package [85]. The effect of pile-up is modelled by superimposing simulated minimum bias events on the hard-scatter simulation, where minimum-bias events are events collected with a loose trigger requirement and are dominated by inelastic scattering.

- **Background: QCD Di-jet:**

Section 2.2 discussed the details of QCD dijet production. In particular in Section 2.2.3.4 it was noted that the relative strength of the strong force compared to other forces of the

---

<sup>3</sup>Further details of  $b$ -jet triggers and this particular trigger used in this analysis is in Section 5.2.

Standard Model means that QCD dijet production would dominate other backgrounds in a di- $b$ -jet event selection. Hence, this will be considered as the only background. A description of how the QCD dijet background is modelled in this analysis is described in Chapter 7. However, a simulated QCD dijet sample is also used in this analysis for background studies and background modelling validation.

Before describing the signal models used it is useful to clearly differentiate between the two definitions of mass used in this analysis. The invariant dijet mass or reconstructed mass is the invariant mass of the two leading jets, and is denoted by  $m_{jj}$ . The simulated mass is the true mass of particle causing a resonance and is defined at the generator level. The two differ due to detector uncertainties when measuring jet energy.

- **Signal:  $Z'$  Boson:**

The  $Z'$  boson is an additional gauge boson that can decay to two  $b$ -quarks, the theoretical  $Z'$  models considered are described in detail in Section 2.3.2.1. The  $Z'$  boson provides a benchmark model in the 2  $b$ -tag category.

In the Summer16+15 data-set analysis two  $Z'$  boson models are considered; the first is the Sequential Standard Model (SSM)  $Z'$  and the leptophobic  $Z'$ . Monte-Carlo simulation is used to produce  $m_{jj}$  signal templates. Only decays to  $b\bar{b}$  are simulated; other decays of the  $Z'$  are ignored such that our results are easier to interpret for other signal models decaying to pairs of  $b$ -quarks. Simulated  $Z'$  boson templates are produced at simulated mass points of 1250, 1500, 1750, 2000, 2500, 3000, 4000 and 5000 GeV.

- **Signal:  $b^*$  Quark:**

The  $b^*$  quark is the third generation excited quark which results from quark compositeness models. The dominant decay mode of the  $b^*$  quark is to  $bg$ . The model considered is described in detail in Section 2.3.2.2. The  $b^*$  quark provides a benchmark model in the  $\geq 1$   $b$ -tag category.

In the Summer16+15 and Full16+15\_HighMass data-sets the same  $b^*$  quark model is considered. Monte-Carlo simulation is used to produce a  $b^*$  quark  $m_{jj}$  signal template. Decays to  $bg$ ,  $b\gamma$ ,  $bZ_0$  and  $tW^-$  are considered. In the Full16+15\_LowMass data-

set only the 2  $b$ -tag category is used and as such that the  $b^*$  model is not considered. Simulated  $b^*$  quark templates are produced at simulated mass points of 1250, 1500, 1750, 2000, 2500, 3000, 4000 and 5000 GeV.

## 6.4 Event Selection

The overall aim when designing the di- $b$ -jet analysis event selection is two-fold. Firstly, events are selected to maximise sensitivity to signal; which we approximate in terms of  $S/\sqrt{B}$ , where  $S$  is the number of benchmark signal events and  $B$  is the number of background events. Secondly, we need to maintain the smoothly falling nature of the background as this is the underlying assumption of the background estimation strategy, which will be described in Chapter 7.

The di- $b$ -jet event selection is split up into three sections each described separately. Firstly we select a pair of jets to be considered (Section 6.4.1), then we apply a set of event-level kinematic cuts using the selected jets (Section 6.4.2) and finally we apply  $b$ -tagging to the jets (Section 6.4.3). In Section 6.4.4 the full event selection is summarised and the signal acceptance is evaluated.

The event selection is slightly different for each of the data-sets considered, these differences will be noted and discussed in the text.

### 6.4.1 Jet Selection

Jets are reconstructed using the anti- $k_T$  algorithm with  $R = 0.4$  and calibrated using the EM+JES scheme; a full description of jets used in this analysis is in Section 4.2.

At least two jets are required in an event. The two highest  $p_T$  jets, referred to as the leading and subleading jet, are the jets used throughout this analysis. To reduce the number of fake jets from sources such as calorimeter noise both jets are required to pass *loose* jet cleaning cuts based on the properties and distributions of the energy deposits in the calorimeter associated to the jet; details can be found in [86].

Cuts are applied to the leading and subleading jet- $p_T$  such that events are on the trigger plateau; the kinematic region where all events passing the offline jet- $p_T$  selection would

also pass the online jet- $p_T$  requirements of the trigger<sup>4</sup>.

For the Summer16+15 data-set; it is required that the leading jet has  $p_T > 430$  GeV to be on the trigger plateau of HLT\_j380. This cut is derived by comparing the leading jet- $p_T$  distributions of jets that pass the trigger, HLT\_j380, relative to a benchmark trigger with a lower jet- $p_T$  threshold, L1\_J75. Figure 6.2 shows this comparison in one run of data where L1\_J75 was un-prescaled<sup>5</sup>; in the ratio plot it is shown that for leading jet- $p_T > 430$  GeV events are on the trigger plateau. The subleading jet is required to have jet- $p_T > 60$  GeV, to avoid contamination from pile-up jets. Both jets are required to have  $|\eta| < 2.4$  such that the jets lie within the volume of the ATLAS pixel detector, which is essential for optimal  $b$ -tagging performance.

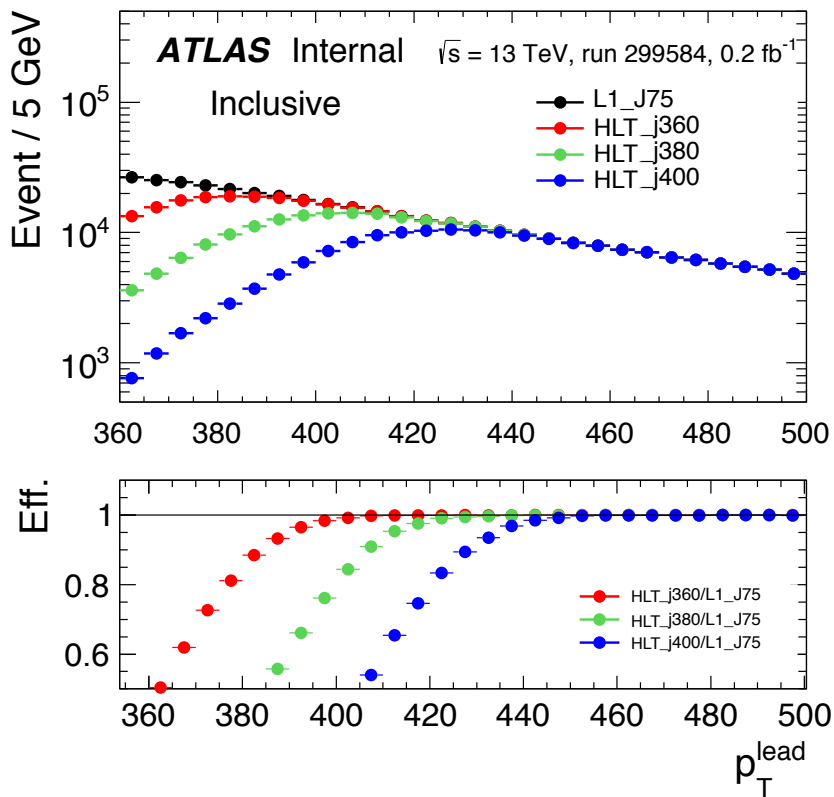


**Figure 6.2:** The comparisons of the leading jet- $p_T$  using an unprescaled L1\_J75 trigger (black dots) to the HLT\_J360 trigger (red dots), HLT\_J380 trigger (green dots) and HLT\_J400 trigger (blue dots) in one run of 2016 data. The ratio with respect to L1\_J75 is shown in the lower panel [81].

<sup>4</sup>Online refers to reconstructed objects used in the trigger decision whilst offline refers to objects reconstructed after events have passed the trigger at the data-processing level, from the definition in Section 5.3.

<sup>5</sup>Un-prescaled means that the trigger accepts every event passing the trigger selection criteria

### 6.4.2 Event Level Cuts

Using the two selected jets; there are a set of event-level requirements. Firstly, events are required to have good reconstruction quality; specifically the primary vertex must have at least two tracks associated with it and events with problematic reconstruction in the Tile calorimeter, LAr calorimeter or SCT are rejected. **LM Fix, not sure what these are**

Secondly, there is a cut applied to the variable  $y^*$ , defined as

$$y^* = \frac{(y_1 - y_2)}{2} \quad (6.1)$$

where  $y_1$  and  $y_2$  are the rapidities of the leading and subleading jet respectively. As discussed in Section 2.2.3.4, QCD dijet production can occur through  $t$ -channel processes leading to more background events at large values of  $|y^*|$ , whilst signal production occurs only through  $s$ -channel processes so will have no dependence on  $y^*$ . Therefore, requiring  $|y^*|$  below some threshold value will lead to an increased  $S/\sqrt{B}$ .

In the Summer16+15 data-set we require  $|y^*| < 0.6$ . This value has been shown to maximise  $S/\sqrt{B}$  when no  $b$ -tagging is applied at previous inclusive dijet searches at ATLAS [87]<sup>6</sup>. The effect of  $b$ -tagging on the optimal value of this cut is assumed to be small, as  $t$ -channel processes still dominate the background.

Finally, the invariant mass of the two leading jets,  $m_{jj}$ , is required to above a threshold value. This cut ensures that there is no kinematic bias on the  $m_{jj}$  distribution from the trigger or jet- $p_T$  requirements described in Section 6.4.1. In addition, it is also required that the background is smooth in the  $m_{jj}$  region chosen such that it can be described using our background modelling strategy.

In the Summer16+15 data-set we require  $m_{jj} > 1378$  GeV; which ensures the two conditions listed above are met. Firstly, Figure 6.3 shows the comparison of  $m_{jj}$  distributions for events that pass the analysis jet- $p_T$  requirements and trigger, HLT\_j380, compared to events that pass a reference trigger, L1\_J75 in one run of data where L1\_J75 was un-prescaled. The ratio plot demonstrates that for  $m_{jj} > 1100$  GeV there is no kinematic bias from the trigger or jet- $p_T$  cuts. Secondly, it has been shown using simulated events that

---

<sup>6</sup>Inclusive dijet analysis means a dijet analysis where no  $b$ -tagging is applied

$m_{jj} > 1378$  GeV is required such that the  $m_{jj}$  distribution from QCD dijet production can be described by our background modelling strategy; this study is presented in Section 7.4.3. Hence,  $m_{jj} > 1378$  GeV is the loosest cut that meets both of the conditions.

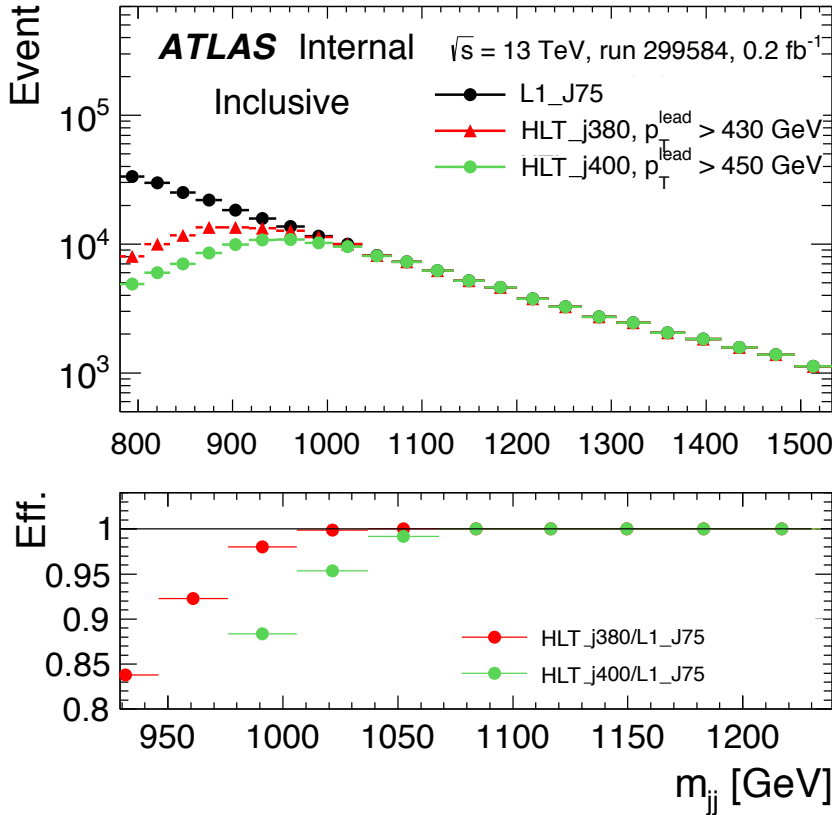


**Figure 6.3:** The comparisons of the  $m_{jj}$  distribution of events that pass an unprescaled L1\_J75 trigger (black dots) to the events that pass the HLT\_J380 trigger with leading jet- $p_T > 430$  GeV (red dots) and the HLT\_J400 trigger with a leading jet- $p_T > 450$  GeV (green dots) in one run of 2016 data. The ratio with respect to L1\_J75 is shown in the lower panel [81].

### 6.4.3 $b$ -Tagging

The selection of  $b$ -jets, known as  $b$ -tagging, and forms an essential technique in the di- $b$ -jet event selection. A detailed description of  $b$ -tagging is found in Section 4.3.  $b$ -tagging is performed using a multi-variate algorithm known as MV2c10 which has been described in 4.3.3.

Two  $b$ -tagging categories are used for the two different types of signal model considered. The 2  $b$ -tag category requires that the both jets are  $b$ -tagged, and is used to search for

resonances decaying to 2  $b$ -quarks such as the  $Z'$  boson. The  $\geq 1$   $b$ -tag category requires that at least one jet is tagged, and is used to search for resonances decaying to 1  $b$ -quark and a quark/gluon such as the  $b^*$  quark. The exclusive 1  $b$ -tag category was also considered but was found to be less sensitive to the  $b^*$  model.

In the `Summer16+15` and `Full16+15_HighMass` data-sets  $b$ -tagging is performed using the fixed cut 85% operating point of the MV2c10 algorithm<sup>7</sup>. This operating point was chosen to maximise  $S/\sqrt{B}$  for a range of simulated mass points in the 2  $b$ -tag category.

Below are details of the  $b$ -tagging optimisation study for the `Full16+15_HighMass` data-set are shown, the results also validate the choice of  $b$ -tagging operating point in the `Summer16+15` data-set. The number of background events,  $B$ , is estimated in a narrow mass window around each mass point considered using a  $18.9 \text{ fb}^{-1}$  subset of data for the 2  $b$ -tag category. The number of signal events,  $S$ , is estimated in the same narrow mass windows using the simulated SSM  $Z'$ -boson signal template described in Section 6.3 scaled to  $18.9 \text{ fb}^{-1}$ <sup>8</sup>. The full `Full16+15_HighMass` event selection has been applied. Table 6.1 summarises  $S/\sqrt{B}$  for each operating point; the 85% operating point is selected as it performs well across the full range of mass points considered. The conclusions of this study are luminosity independent as  $S/\sqrt{B} \propto 1/\sqrt{L}$  such that the relative sensitivity between operating points will be the same for all luminosities.

Signal Mass [GeV]	1500	2000	2500
Mass window [GeV]	1378-1573	1785-2114	2267-2659
$S/\sqrt{B}$ for 85% OP	2.02	0.72	0.21
$S/\sqrt{B}$ for 77% OP	2.12	0.64	0.17
$S/\sqrt{B}$ for 70% OP	1.73	0.47	0.12
$S/\sqrt{B}$ for 60% OP	0.96	0.21	0.07

**Table 6.1:** The estimated  $S/\sqrt{B}$  at  $18.9 \text{ fb}^{-1}$  for 4 different MV2c10 operating points (OP).  $S$  is estimated using a SSM  $Z'$ -boson and  $B$  is estimated using a  $18.9 \text{ fb}^{-1}$  subset of 2  $b$ -tag category data. The `Full16+15_HighMass` data-set event selection has been applied. Three different mass points are considered and the mass windows used to estimate  $S$  and  $B$  for each mass point are shown in the table [88].

To further understand the effect of  $b$ -tagging in this analysis the flavour composition of the background is studied. The dijet flavour composition is defined as the truth flavour

<sup>7</sup>Details on the operating points of MV2c10 are found in 4.3.3

<sup>8</sup>This is the amount of data collected when the studies were performed

of both of the jets used in the di-*b*-jet analysis, using the definition of truth flavour from Section 4.3.1. Figure 6.4 shows the dijet flavour composition of the simulated QCD dijet background in the case where no *b*-tagging has been applied (inclusive) and in the  $\geq 1$  and 2 *b*-tag categories. For this figure the `Summer16+15` data-set event selection has been applied, although the distributions are very similar for the `Full16+15_HighMass` data-set as the same *b*-tagging operating point has been chosen.

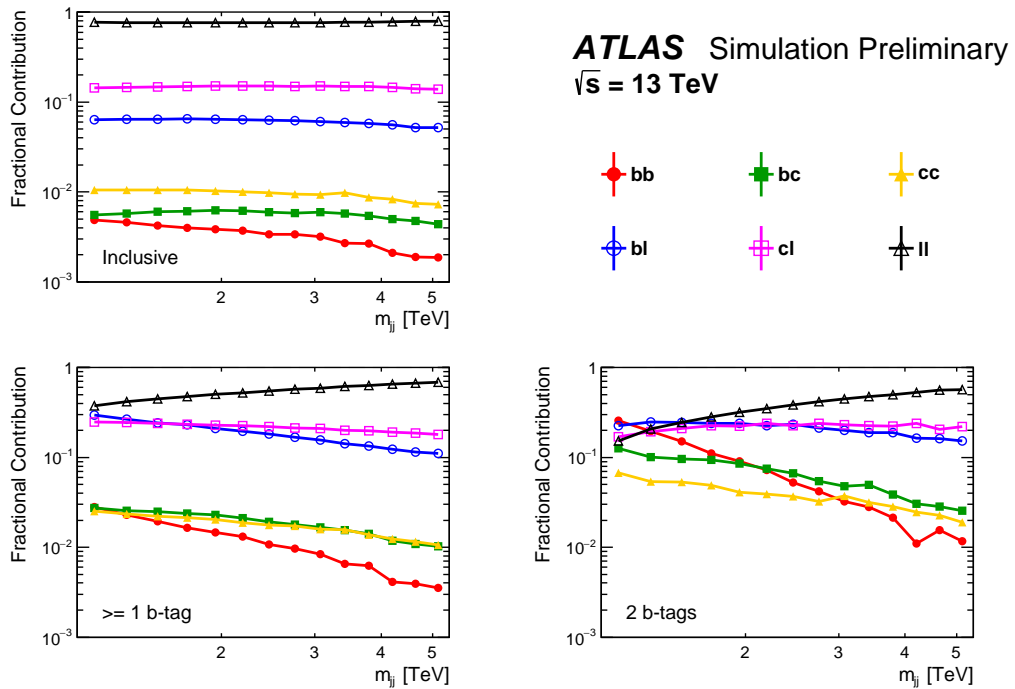


**Figure 6.4:** The dijet flavour composition of the simulated dijet background as a function of dijet mass, shown without applying *b*-tagging (inclusive) and for  $\geq 1$  *b*-tag and 2 *b*-tag categories. In the legend *b*, *c* and *l* refere to a truth matched *b*-jet, *c*-jet and light jet respectively. The *Summer16+15* dataset event selection has been applied.

There are a few features that can be noted in this figure. Firstly, the flavour fraction of the background before *b*-tagging is dominated by light-jets for the reasons outlined in Section 2.2.3.4. As the background is dominated by light-jets the application of *b*-tagging can increase background rejection and thus increase sensitivity to signal models that decay to *b*-quarks. This motivates the use of *b*-tagging in the analysis.

Secondly, even after the application of *b*-tagging the largest contribution to the background is from light jets, except for in a small region at low mass in the 2 *b*-tag category. This shows that the sensitivity of the analysis is limited by the light-jet rejection of *b*-tagging

at high jet- $p_T$ .

Finally, in all three cases the dijet flavour fractions are smooth, which is evidence that there are no sudden changes in  $b$ -tagging efficiency of the background that could introduce a non-smooth feature in the background invariant mass spectra.

#### 6.4.4 Event Selection Summary

A summary of the key components of the di- $b$ -jet event selection for each of the data-sets considered is listed Table 6.2.

Cut	Summer16+15	Full16+15_HighMass	Full16+15_LowMass
Trigger	Single-jet	Single-jet	Double $b$ -jet (60% OP)
Online LJ $p_T$	$> 380 \text{ GeV}$	$> 380 \text{ GeV}$	$> 150 \text{ GeV}$
Online SLJ $p_T$	-	-	$> 50 \text{ GeV}$
Leading Jet- $p_T$	$> 430 \text{ GeV}$	$> 430 \text{ GeV}$	$> 200 \text{ GeV}$
Subleading Jet- $p_T$	$> 60 \text{ GeV}$	$> 80 \text{ GeV}$	$> 80 \text{ GeV}$
Jet- $ \eta $	$< 2.4$	$< 2.0$	$< 2.0$
$m_{jj}$	$> 1378 \text{ GeV}$	$> 1200 \text{ GeV} (2 \text{ } b\text{-tag})$ $> 1341 \text{ GeV} (\geq 1 \text{ } b\text{-tag})$	$> 500 \text{ GeV}$
$ y^* $	$< 0.6$	$< 0.8$	$< 0.6$
$b$ -Tagging OP	85%	85%	70%
$b$ -Tag Categories	2 and $\geq 1$	2 and $\geq 1$	2

**Table 6.2:** A summary of the key event selections applied in the di- $b$ -jet analysis for each of the data-sets considered. For full details refer to the text.

To better visualise events that pass the event selection, Figure 6.5 show events displays for high  $m_{jj}$  events that pass the  $\geq 1$  and 2  $b$ -tag  $b$ -tag event selection respectively. The figure was made using the VP1 event display package [89]. These events are pass both the Summer16+15 and Full16+15\_HighMass data-set event selection.

With the event selection now defined the signal acceptance of the di- $b$ -jet analysis is studied to understand the performance of the analysis selection and as an input to the limit-setting phase of the analysis. The signal acceptance multiplied by trigger efficiency is defined as the fraction of signal events that would pass the analysis' trigger and event selection. In addition, as  $b$ -tagging is a unique cut in our analysis relative to other dijet searches, we also consider the event-tagging efficiency defined as the fraction of events that pass  $b$ -tagging cuts given that the event has passed all other aspects of the event selection.

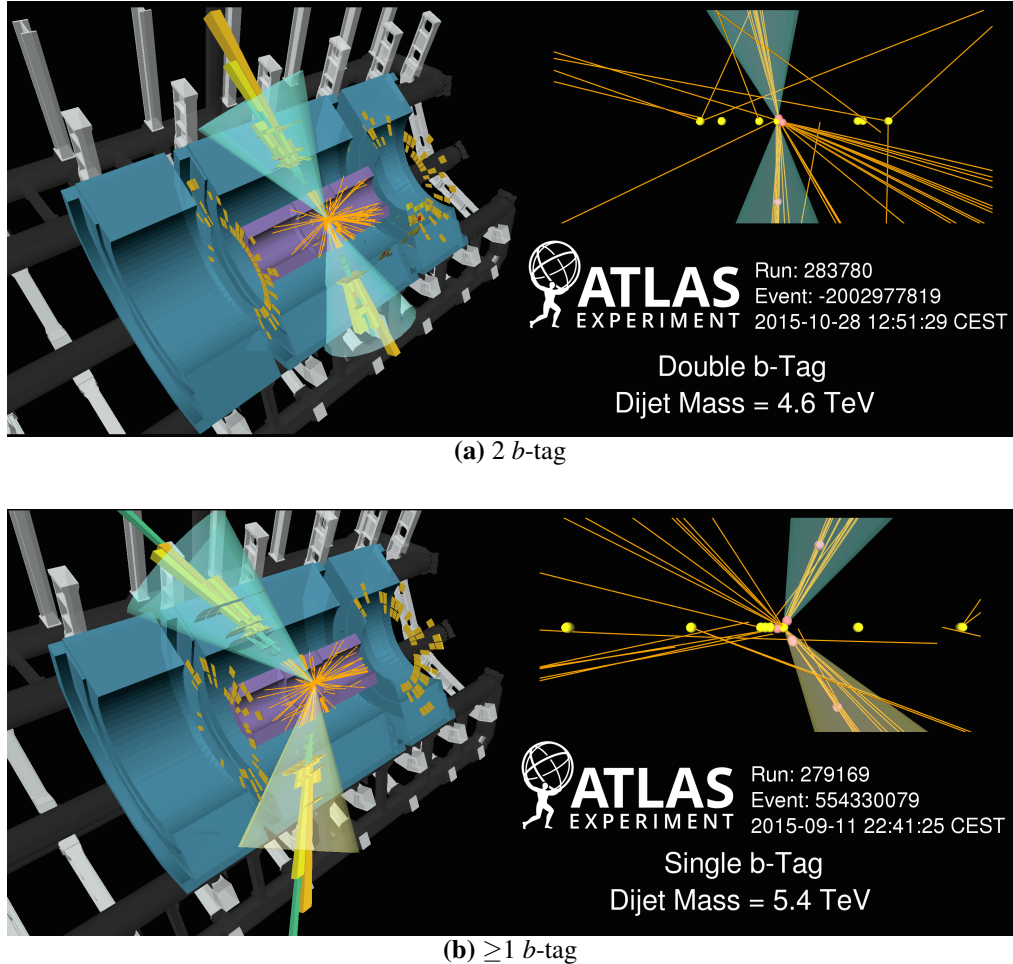


**Figure 6.5:** Event displays showing high  $m_{jj}$  events that pass the (a) 2 and (b)  $\geq 1$   $b$ -tag di- $b$ -jet event selection. The left section of the figures show a cut-away of the ATLAS detector; the inner detector is shown in purple, the hadronic calorimeter is shown in blue and the toroid magnet and supporting structure is shown in black and grey. The upper right section of the figures show a close-up view of the inner tracker in the  $r - z$  plane. In both sections tracks inside the inner detector are shown in orange and energy deposits in the EM and hadronic calorimeter are shown in cyan and yellow respectively. The two leading jets formed are indicated by the cones, where a blue cone indicates that the jet has been  $b$ -tagged and a yellow cone shows that it has not. The yellow spheres show the primary vertex candidates and the red spheres show the secondary vertex candidates.

Signal acceptance and event tagging efficiency are estimated using the Monte-Carlo signal templates discussed in Section 6.3.

For the Summer16+15 data-set event-selection; Figure 6.6(a) shows the signal acceptance multiplied by trigger efficiency for the  $b^*$  and  $Z'$  signal models as a function of the simulated mass in the case that  $b$ -tagging is applied and when it is not applied. Figure 6.6(b) shows the event tagging efficiency for the  $b^*$  and  $Z'$  for a range of simulated mass points

as a function of the reconstructed invariant mass,  $m_{jj}$ . In both plots the  $b$ -tagging category used is labelled in the legend.

There are a few features of the signal acceptance and tagging efficiency that can be commented on. There is reduced signal acceptance at lower values of simulated mass; this is because there is a low mass tail of the signal template which lies below the  $m_{jj}$  cut caused by a preference for low values of  $m_{jj}$  by the PDFs<sup>9</sup>. In addition, the event tagging efficiency decreases at high values of  $m_{jj}$  due to a lower performance of  $b$ -tagging at high jet- $p_T$ . **LM Fix: Reference high-pT b-tagging, will be added to b-tag chapter.** Finally, we see that the  $b^*$  quark has a similar tagging efficiency as the  $Z'$ -boson in the  $\geq 1$   $b$ -tag category at high  $m_{jj}$ ; whilst naively one would expect that the  $Z'$ -boson should have a higher event tagging efficiency as it decays to two  $b$ -quarks, the gluon from the  $b^*$  quark decay can split into a pair of lower  $p_T$   $b$ -quarks which can often be tagged leading to a similar tagging efficiency.

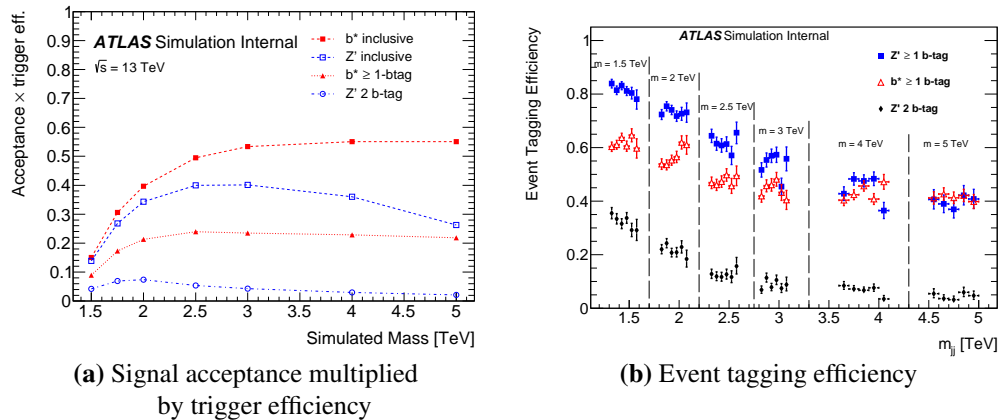


**Figure 6.6:** Plots to show the acceptance of the *Summer16+15* data-set event selection for the  $b^*$  quark and  $Z'$ -boson signal models. Panel (a) shows the signal acceptance multiplied by trigger efficiency as a function of the simulated mass of the signal model, in the case where  $b$ -tagging has been applied and not. Panel (b) shows the event tagging efficiency as a function of the dijet invariant mass,  $m_{jj}$ , for a range of simulated masses,  $m$ , as indicated on the plot. In both figures the  $b$ -tagging categories used are indicated in the legend. Details of the *Summer16+15* data-set event selection are described in the text. Figures taken from [81]

---

<sup>9</sup>Parton Distribution Function, see Section 2.2.3.3.

## Chapter 7

# Di-*b*-jet Search: Search Phase

The role of the search phase is to identify if there is any evidence of beyond standard model physics in the form of a resonance (or a bump) in the  $m_{jj}$  spectra of the di-*b*-jet events selected. This is carried out in two parts; firstly a background fit is used to estimate the  $m_{jj}$  distribution of the QCD dijet background. Then, the difference between the data and the background estimation is used to search for a significant excess that would be evidence of BSM physics.

In this chapter I will describe the details of the  $m_{jj}$  spectra used in the analysis (Section 7.1), the background estimation strategy (Section 7.2), the technique used to search for excesses (Section 7.3) and then I will present the search phase validation and results from each of the data sets.

## 7.1 Invariant Dijet Mass Spectrum

The invariant dijet mass spectrum, or  $m_{jj}$  spectrum, is the distribution of the invariant mass of the leading and subleading jet. The  $m_{jj}$  spectrum is analysed in a binned histogram, the bin width is chosen to be approximately the same size as the dijet mass resolution whilst still giving a smooth  $m_{jj}$  spectrum [90]. The exact bins are chosen are shown in Appendix A.

There is a different  $m_{jj}$  spectrum for each *b*-tagging category considered, and an independent search phase will be performed for both.

## 7.2 Background Estimation

Many analyses at ATLAS use Monte-Carlo simulation to model backgrounds [51]. However, simulation is not used to model the background in the di-*b*-jet search due to three problems; firstly it is difficult to produce Monte-Carlo simulation at high-enough statistical precision, secondly there are large theoretical uncertainties for Monte-Carlo QCD (such as PDF uncertainties and choice of renormalisation scale) and finally there are large experimental uncertainties affecting data-simulation comparisons (such as jet energy scale).

Instead, the background is described using a smooth fit function. This approach utilises the fact that the QCD dijet spectrum is smoothly falling with respect to  $m_{jj}$ , as discussed in Section 2.2.3.4. Fit functions have been widely used in a wide range of searches for resonances on smoothly falling backgrounds including previous dijet and di-*b*-jet searches [87, 91, 92].

This approach gives two requirements on a fit function; firstly the fit function must be able to describe the di-*b*-jet spectrum from QCD, including any detector or reconstruction effects that could impact the shape such as *b*-tagging. Secondly, the fit function used must be constrained enough such that there is no bias if there is a resonance present in the di-*b*-jet spectrum. As evidence of such a resonance is found when the data diverges from the fit, such a bias could reduce the sensitivity to signal. The fit functions considered in this analysis will be described in the following section.

For any given fit function, data is used to determine the parameters of the fit function. This is done by minimising the negative log likelihood, where the likelihood is calculated from comparing the binned data to the fit function under the assumption of Poisson errors.

### 7.2.1 Dijet Fit Functions

The di-*b*-jet mass spectrum will be described by the dijet fit functions, which are a family of functions with a varying number of parameters. The dijet fit functions are listed in Table 7.1.

The dijet fit functions are motivated using a theoretical understanding of the QCD dijet production and experience from previous dijet searches [16]. The 3 parameter dijet fit function has been used in dijet searches beginning with CDF [93] and the three compo-

Function Name	Equation	$x$
3 parameter	$f(x) = p_1(1-x)^{p_2}x^{p_3}$	$m_{jj}/\sqrt{s}$
4 parameter	$f(x) = p_1(1-x)^{p_2}x^{p_3+p_4 \ln x}$	$m_{jj}/\sqrt{s}$
5 parameter	$f(x) = p_1(1-x)^{p_2}x^{p_3+p_4 \ln x+p_5(\ln x)^2}$	$m_{jj}/\sqrt{s}$
6 parameter	$f(x) = p_1(1-x)^{p_2}x^{p_3+p_4 \ln x+p_5(\ln x)^2}$	$m_{jj}/p_6$

**Table 7.1:** The dijet fit function equations. The fit functions are named by the number of free parameters used.  $p_i$  are the free parameters of the fit function

nents are motivated as follows: the  $p_1$  term gives the normalisation, the  $(1-x)^{p_2}$  term is a common parameterisation for the behaviour of the PDFs with the property of vanishing as  $x$  approaches unity, and the  $x^{p_3}$  term is motivated by the  $1/m_{kl}$  term in the matrix element (shown in Equation 2.6). Additional parameters of  $x^{p_4 \ln x}$  and  $x^{p_5 \ln x^2}$  have been considered in dijet searches to give an adequate description of the tail when large mass ranges are considered [94, 90]. Finally, the  $x = m_{jj}/p_6$  term is added as an additional degree of freedom. This function has been found to provide a satisfactory fit to the leading and next-to-leading-order QCD Monte-Carlo simulation.

The functions with higher number of parameters may be required to describe the di- $b$ -jet mass spectrum; especially in large data-sets where small statistical errors reveal finer details of the QCD background shape and large mass ranges where larger constraints are applied to the fit in each mass range. However, additional parameters also allow for more flexibility in the background shape which might cause a fit bias if a resonance is present. Hence, there is an overall strategy to use the fewest number of parameters that can adequately describe the background, such that sensitivity to signal is maximised.

### 7.2.2 Wilks' Statistic

To decide whether a fit function has adequate number of parameters the Wilks' test statistic is used, as done in previous iterations of both the inclusive and  $b$ -tagged dijet search [87, 91]. For this test we consider a null hypothesis that a nominal dijet fit function contains enough parameters to describe the data and an alternate hypothesis that a dijet fit function with one extra parameter is required. The Wilks' test statistic is defined as  $-\log(\Lambda)$ , where  $\Lambda$  is the likelihood ratio of the nominal and alternate function. Using Wilks' theorem it is known

that for nested functions<sup>1</sup>, such as the dijet fit functions, the Wilks' test statistic will follow a  $\chi^2$  distribution with 1 degree of freedom [95]. Therefore a  $p$ -value can be calculated for our null hypotheses that the nominal function has sufficient number of parameters. Such a  $p$ -value will be referred to as the Wilks'  $p$ -value throughout this section.

### 7.3 BumpHunter Algorithm

Once the background has been modelled using a fit, the next step is to determine if there is evidence of a resonance in the di- $b$ -jet invariant mass spectra. As shown in Figure 6.1 such a resonance would appear as a bump on the smoothly falling background distribution. This can be observed as a discrepant excess in the  $m_{jj}$  spectrum; where an excess is defined as any set of consecutive bins that contains more events in data than the background prediction, and discrepant describes how inconsistent an excess is with the background estimation. To set this up in terms of hypothesis testing, the null hypothesis,  $H_0$ , states that there is only QCD dijet events described by our background function, whilst the alternate hypothesis,  $H_1$ , proposes that there is also a resonance at some unknown mass point in the di- $b$ -jet spectrum causing a discrepant excess.

Due to statistical fluctuations in the background, it is expected that excesses will occur in data even if there is no new physics occurring. Therefore, to claim evidence of a new resonance a significant excess is required, which is an excess that is highly unlikely to have occurred from such a fluctuation. To quantify how significant any excess is a  $p$ -value is used, where a  $p$ -value is defined as the probability of finding an excess which is at least as discrepant as the excess found in data under the assumption of  $H_0$ . Hence, a small  $p$ -value indicates the excess is inconsistent with the null hypothesis and that new physics is present; in particle physics it is conventional to consider that a  $p$ -value below 0.0027 (3  $\sigma$ ) is considered as evidence of new physics whilst a  $p$ -value below 1 in  $\sim$ 3.5 million (5  $\sigma$ ) is considered as the discovery of new physics.

In this analysis the BUMPHUNTER algorithm [?] is employed; this algorithm uses a test-statistic to search for the most discrepant excess in our data-set and calculate the  $p$ -

---

<sup>1</sup>Nested functions occur when the simpler function can be taken from a more complex function by setting one parameter to a specific value. For example the 3 parameter function can be taken from the 4 parameter function when  $p_4 = 0$  and so on

value of such an excess. The BumpHunter test statistic gives a quantitative measure of how discrepant any given excess in data is under the assumption of  $H_0$ . To derive the test statistic let's consider  $N$  consecutive bins for which a total of  $d$  data events are found and a total of  $b$  background events are expected. As this is a search for excesses we will consider the case where  $d > b$ . Using Poisson statistics one can calculate the probability of seeing an excess which is at least that discrepant under the assumption of the null hypothesis:

$$P(d, b) = \sum_{n=d}^{\infty} \frac{b^n e^{-b}}{n!} \quad (7.1)$$

From this probability, the BumpHunter test statistic,  $t$ , is defined as

$$t = -\log(P(b, d)) \quad (7.2)$$

The size of the test statistic represents how discrepant an excess is, with a large  $t$  indicating a discrepant excess. Using the same logic and requiring that  $d < b$  it is possible to also search for deficits, this is referred to as the DeficitHunter  $p$ -value.

The BumpHunter algorithm calculates the value of  $t$  for all excesses in the  $m_{jj}$  spectrum by scanning over all possible combinations of consecutive bins. The narrowest excess allowed is two bins and the widest excess allowed has half the number of bins in the spectrum. This excess with the largest BumpHunter test-statistic is the most discrepant excess and the value of  $t$  observed is labelled  $t_{obs}$ .

To calculate the  $p$ -value of the most discrepant excess Poisson fluctuations are applied to the background model to create pseudo-experiments, which are data-like spectra that are consistent with the null hypothesis. In each pseudo-experiment the BumpHunter scan is performed to find the most discrepant excess and corresponding value of  $t$ . This is done for many pseudo-experiments to estimate the probability density function of  $t$  under the assumption of the null hypothesis, which I will label as  $f_{PE}(t|H_0)$ . By comparing the observed test-statistic in data,  $t_{obs}$ , to the distribution in the pseudo-experiments, the BumpHunter  $p$ -value of the most discrepant excess in data is calculated using

$$\text{BumpHunter } p\text{-value} = \int_{t_{obs}}^{\infty} f_{PE}(t|H_0) \quad (7.3)$$

The BumpHunter algorithm is chosen to search for excesses due to two important features. Firstly, the BumpHunter  $p$ -value is model independant; the algorithm makes no prior assumptions about the nature of the new physics model that could be present other than it would produce extra events and that the extra events would occur in consecutive  $m_{jj}$  bins. Secondly, the BumpHunter  $p$ -value is naturally global; this means that the  $p$ -value accounts for the fact that under the null hypothesis an excess such as the one observed could have occurred at any mass point in the  $m_{jj}$  spectrum. This is due to the fact that in the pseudo-experiments there is no prior assumption on the location of the most discrepant excess.

## 7.4 *Summer16+15* Search Phase

This section presents the search phase for the *Summer16+15* data-set. Section 7.4.1 describes the background modelling strategy used, Section 7.4.2-7.4.4 shows studies performed to validate the background modelling strategy and Section 7.4.5 presents the results of the search phase.

As described in Chapter 6 there are two  $b$ -tag categories considered for the the *Summer16+15* data-set ( $2 b$ -tag and  $\geq 1 b$ -tag) giving two dijet invariant mass spectra to perform a search phase on.

### 7.4.1 Background Modelling Strategy

For the *Summer16+15* dataset the background is modelled using a global fit function, where a single fit function is used to describe the full mass range of the invariant mass spectra, similar to previous dijet and di- $b$ -jet searches at ATLAS [87, 91].

To select a fit function from the set of dijet fit function described in Table 7.1 the following strategy is used with the final data-set. The 3 parameter dijet function is used as the initial nominal function and hence the 4 parameter dijet fit function function is the initial alternate function. Using the Wilks' statistic a  $p$ -value can be calculated, if the  $p$ -value is less than 0.05, the nominal fit function is rejected and the alternative function becomes the nominal. The process is iteratively run until a dijet fit function is selected with a stable Wilks'  $p$ -value.

In the *Summer16+15* data-set the choice of the dijet fit function choice was fixed using

the Wilks' p-value calculated for a  $8.8 \text{ fb}^{-1}$  subset of data. This is because the analysis was being formed as data was being collected and a function choice was required to present the analysis to the collaboration before the final  $4.5 \text{ fb}^{-1}$  of data was processed and available. Figure 7.1 shows the Wilks'  $p$ -value as a function of luminosity for the  $\geq 1 b$ -tag and  $2 b$ -tag categories for the  $8.8 \text{ fb}^{-1}$  subset of data. For both categories the 3 parameter fit function when compared to the 4 parameter fit function has a Wilks'  $p$ -value  $> 0.05$ . Therefore the 3 parameter fit function was selected in both categories. Given that the 3 parameter fit function was adequate to describe the majority of the data-set it is a good assumption that it would be able to describe the full data-set. However, I think with hindsight that it would have been better to perform the Wilks' test on the full data-set.

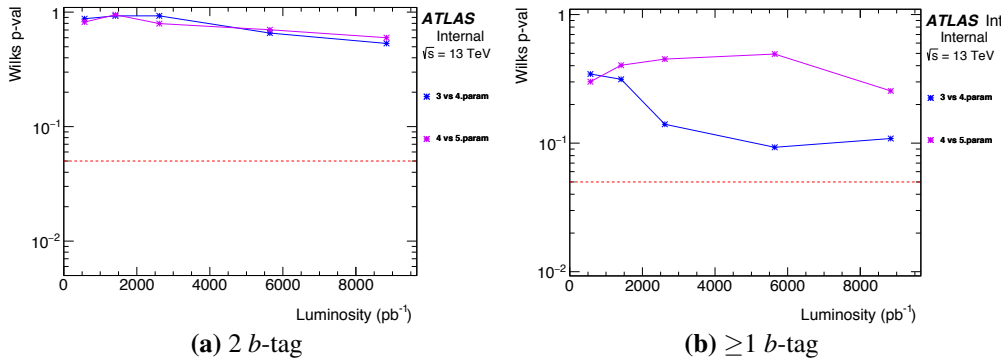


**Figure 7.1:** The Wilks'  $p$ -value as a function of luminosity in the case that the 3 parameter is the nominal function and the 4 parameter is the alternate (blue) and the case where the 4 parameter is the nominal function and the 5 parameter is the alternate (purple) for a  $8.8 \text{ fb}^{-1}$  subset of data in the (a)  $2 b$ -tag and (b)  $\geq 1 b$ -tag category. The *Summer16+15* data-set event selection has been applied [?].

### 7.4.2 Fit Tests: Background-Only Dataset

To demonstrate that the dijet fit functions are a valid description of the background, fit tests are performed to a representative background only data-set.

To perform these tests, the PYTHIA8 MC QCD multi-jet simulation is used as the representative background only data-set. The simulation sample is produced in several slices of leading jet  $p_T$ , where each slice contains the same number of events. A weight is applied to each event such that the final distribution is representative of the smoothly falling  $m_{jj}$  spectrum that is expected, whilst still maintaining a similar precision across the full mass range.

The weighted invariant mass distribution is then scaled to  $10 \text{ fb}^{-1}$ <sup>2</sup>, this is referred to as the ‘scaled distribution’, which can be interpreted as the expected number of data events in a specific mass bin. The precision of the scaled distribution is represented by the number of ‘effective entries’; the number of effective entries is the number of data events that would be required to give the same precision, or to put it another way it is the square of the error in that mass bin. The number of effective entries can be calculated from the event weights as shown in Equation 7.4.

$$N_{eff} = (\sum w_i)^2 / \sum w_i^2 \quad (7.4)$$

Figure 7.2 shows the scaled and effective entries distributions as a function of dijet invariant mass for the 2  $b$ -tag and  $\geq 1 b$ -tag categories.

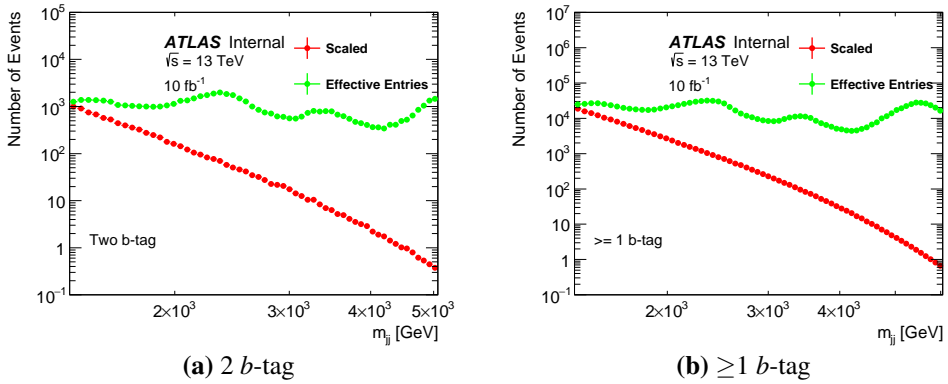


**Figure 7.2:** The scaled invariant mass distribution (red) compared to the effective entries of the invariant mass distribution (green) of Monte-Carlo simulation for the (a) 2  $b$ -tag and (b)  $\geq 1 b$ -tag category. The *Summer16+15* dataset event selection has been applied.

### 7.4.3 Fit Tests: Mass Range Studies

The first fit test is to demonstrate that the dijet fit functions are able to describe the  $m_{jj}$  spectra. In this test the scaled invariant mass spectra from simulation, are fitted to using the search phase procedure. The errors on the invariant mass spectrum are given by the square root of the number of effective entries which effectively gives the statistical error of the simulated sample.

The dijet mass spectra considered have a lower mass edge of  $m_{jj} = 1100 \text{ GeV}$ , selected

---

<sup>2</sup> These studies were carried out during data-taking and as such the final integrated luminosity of the data-set had to be estimated,  $10 \text{ fb}^{-1}$  was used where the final data-set is  $13.3 \text{ fb}^{-1}$ .

such that there is no kinematic bias from the single jet trigger, and the upper edge is the mass bin at which the dijet mass spectrum goes below one entry per bin. Figure 7.3 and 7.4 show the search phase for both  $b$ -tag categories, fitted to with the 4 and 5 parameter fit function. The most discrepant excess is indicated by the blue lines and the BumpHunter  $p$ -value of the excess is shown on the plot, which has been calculated using 10,000 pseudo-experiments. Similarly, the  $p$ -value of the most discrepant deficit is calculated using the same process, which is referred to as DeficitHunter, and an overall quality of fit  $p$ -value is also calculated by the same process using the  $\chi^2$  test statistic. The lower panel shows the significance in each  $m_{jj}$  bin, defined the difference between the data and the background estimate divided by the error on the data point.

For both fit functions in the  $\geq 1$   $b$ -tag category, a large excess is observed which has been assigned a BumpHunter  $p$ -value of 0.00. This indicates that the 4 and 5 parameter fit functions provide a poor description of the background distribution from simulation in the  $\geq 1$   $b$ -tag category. Note that although these studies have been performed with the 4 and 5 parameter function, as the 3 parameter function is a subset of the 4 parameter function it can also be concluded that the 3 parameter function will also be inadequate.

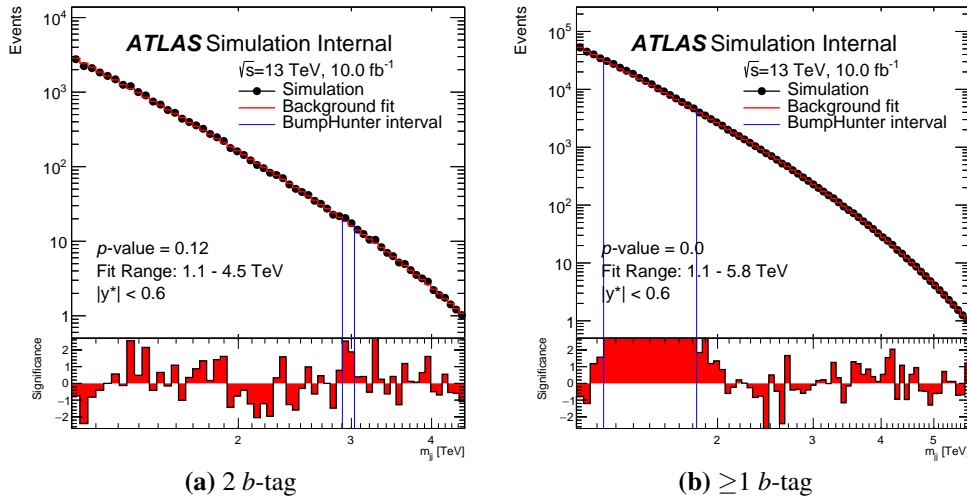


**Figure 7.3:** The invariant mass distribution taken from multi-jet simulation for the (a) 2  $b$ -tag and (b)  $\geq 1$   $b$ -tag, category, fitted to using the 4 parameter fit function, with lower mass bound of the fit range  $m_{jj} = 1100$  GeV. The BumpHunter algorithm is run to identify the most discrepant excess, as indicated by the blue lines. Pseudo-experiments are used to assign the excess a  $p$ -value, which is shown on the plot. The *Summer16+15* dataset event selection has been applied.

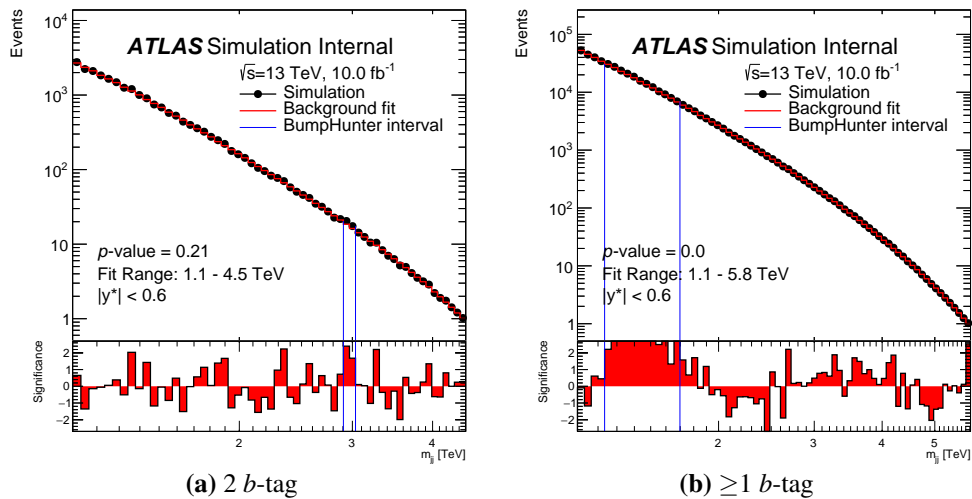
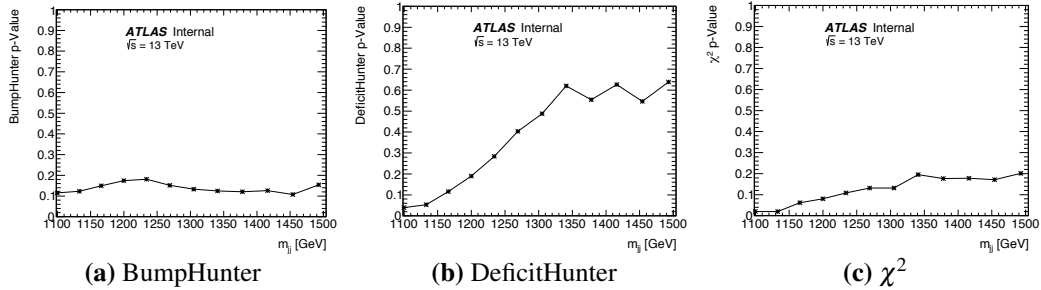


**Figure 7.4:** The invariant mass distribution taken from multi-jet simulation for the (a) 2  $b$ -tag and (b)  $\geq 1$   $b$ -tag, category, fitted to using the 5 parameter fit function, with lower mass bound of the fit range  $m_{jj} = 1100$  GeV. The BumpHunter algorithm is run to identify the most discrepant excess, as indicated by the blue lines. Pseudo-experiments are used to assign the excess a  $p$ -value, which is shown on the plot. The *Summer16+15* dataset event selection has been applied.

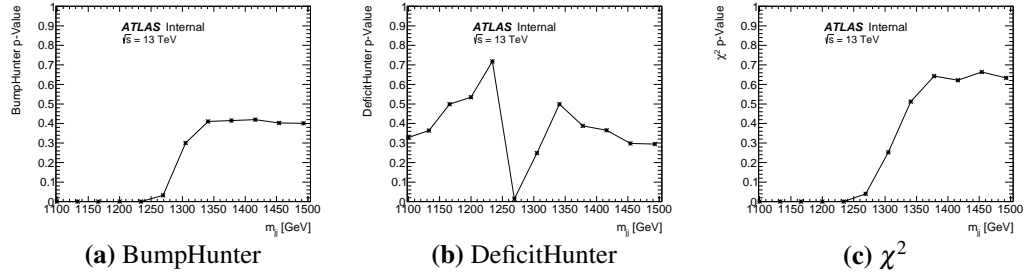
However, by changing the lower mass bound of the fit, a region can be found where the fit functions are able to describe the background accurately. To find the largest region with a stable fit quality, the simulated dijet mass spectrum is fitted to using the 4 parameter function with the lower mass bound of the fit region increased one bin at a time, beginning at  $m_{jj} = 1100$  GeV up to  $m_{jj} = 1500$  GeV. As before the upper edge of the fit region is the mass bin at which the simulation goes below one entry per bin. Figure 7.5 and 7.6 show, for the 2  $b$ -tag and  $\geq 1$   $b$ -tag categories, the distributions of the (a) BumpHunter, (b) DeficitHunter and (c)  $\chi^2$   $p$ -values as the lower mass bound of the fit region is increased. In both categories it is shown that there are fit regions that are stable if the lower mass bound is  $m_{jj} = 1378$  GeV or above. This demonstrates that there are features in the background mass spectrum at low masses that are causing a poor fit quality, which can be removed by using a fit region  $m_{jj} > 1378$  GeV.

Figure 7.7 shows the search phase applied to the dijet mass spectra of the simulated sample for both  $b$ -tagging categories, for the fit range with the lower mass bound of  $m_{jj} = 1378$  GeV, fitted to using the 4 parameter fit function. The most discrepant excess, as found by the BumpHunter algorithm, is indicated by the blue lines and the  $p$ -value of the excess is shown on the plot. This shows that the fit quality is reasonable for this choice of fit region.

The study presented in this section motivates the choice of  $m_{jj} > 1378$  GeV as the lower mass cut used in the Summer16+15 data-set event selection.



**Figure 7.5:** The distribution of the (a) BumpHunter, (b) DeficitHunter and (c)  $\chi^2$   $p$ -values for different values of lower mass bound of the fit range, when fitting to 2  $b$ -tag category invariant mass distribution taken from multi-jet simulation with the 4 parameter fit function. The *Summer16+15* dataset event selection has been applied, with the exception of the  $m_{jj}$  cut.



**Figure 7.6:** The distribution of the (a) BumpHunter, (b) DeficitHunter and (c)  $\chi^2$   $p$ -values for different values of lower mass bound of the fit range, when fitting to  $\geq 1$   $b$ -tag category invariant mass distribution taken from multi-jet simulation with the 4 parameter fit function. The *Summer16+15* dataset event selection has been applied, with the exception of the  $m_{jj}$  cut.

#### 7.4.4 Fit Tests: Spurious Signal

If the true background dijet invariant mass spectrum cannot be described by the chosen fit function, then fit discrepancies can occur that could appear as false signal or could hide a true signal, the former is referred to as spurious signal. To show that fit discrepancies are not occurring, fits are performed to a background-only representative data-set to demonstrate that the chosen fit function is a valid representation of the true background spectrum. Similar tests have been performed in previous iterations of both the inclusive and  $b$ -tagged dijet searches [87, 91].

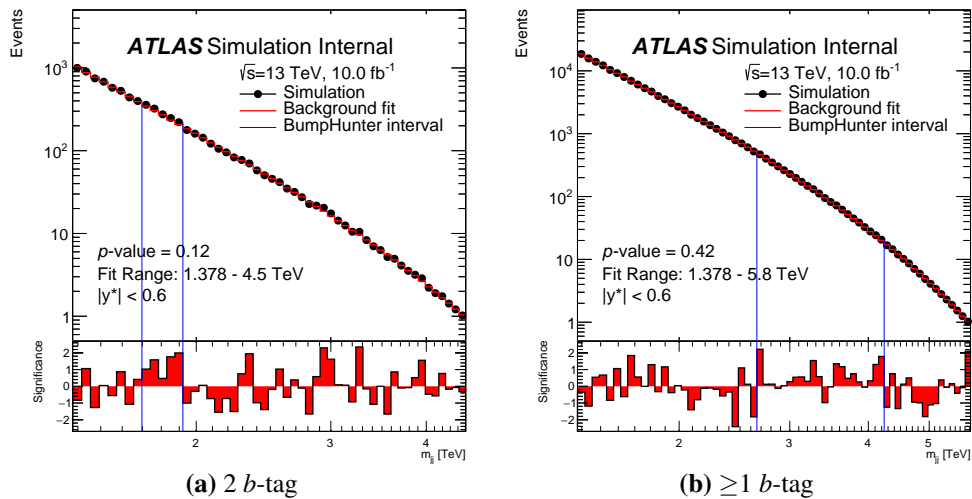


**Figure 7.7:** The invariant mass distribution taken from multi-jet simulation for the (a) 2  $b$ -tag and (b)  $\geq 1$   $b$ -tag, category, fitted to using the 4 parameter fit function, with lower mass bound of the fit range  $m_{jj} = 1378$  GeV. The BumpHunter algorithm is run to identify the most discrepant excess, as indicated by the blue lines. Pseudo-experiments are used to assign the excess a  $p$ -value, which is shown on the plot. The *Summer16+15* dataset event selection has been applied.

To perform these tests, the scaled distribution from the PYTHIA8 Monte-Carlo multi-jet simulation described in Section 7.4.2 is used as the representative background only data-set. As shown in Figure 7.2, the number of effective entries is larger than the number of scaled entries, meaning that the distribution contains smaller statistical fluctuations than are present in the final data-set. To create a more representative simulated data-set to test the fit functions, Poisson fluctuations are applied to the scaled distribution to create a ‘data-like’ distribution. Figure 7.8 shows the scaled and effective entries distributions for both  $b$ -tag categories overlaid with a data-like distribution in blue.

The search phase is then applied to the data-like distributions in both  $b$ -tag categories to test the fit function in a background-only data-set. Figure 7.9 shows an example data-like distribution for both  $b$ -tag categories fitted to with the 3 parameter fit function, with the most discrepant excess as identified by the BumpHunter algorithm shown. The  $p$ -value of the most discrepant excess is calculated by comparing the BumpHunter test statistic in the data-like distribution,  $t_{obs}$ , to 10,000 pseudo-experiments; the procedure is illustrated in Figure 7.10. Using a similar process, the  $p$ -value of the most discrepant deficit is calculated using the DeficitHunter test statistic and an overall quality of fit  $p$ -value is calculated by the  $\chi^2$  test statistic. For this specific set of Poisson fluctuations in the 2  $b$ -tag category the Bum-

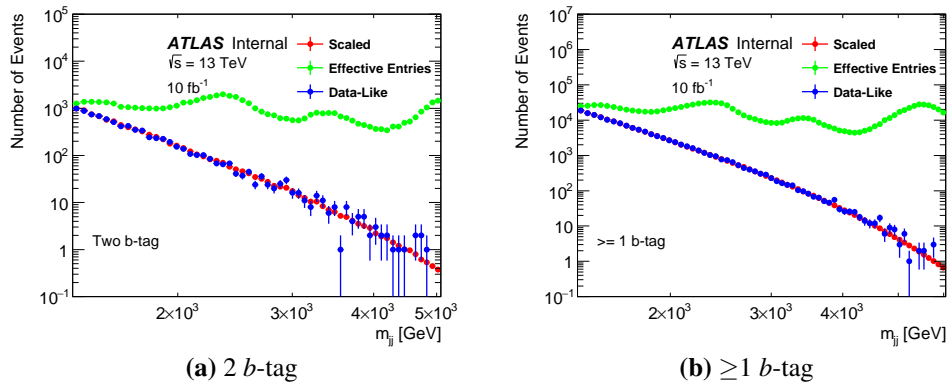


**Figure 7.8:** The scaled invariant mass distribution (red) compared to the effective entries of the invariant mass distribution (green) for the 2  $b$ -tag category, for the (a) 2  $b$ -tag and (b)  $\geq 1$   $b$ -tag case. Overlaid is a data-like distribution (blue) created by applying Poisson fluctuations to the scaled distribution. The *Summer16+15* dataset event selection has been applied.

pHunter, DeficitHunter and  $\chi^2$  *p*-value are found to be 0.57, 0.80 and 0.39 respectively. Similarly, in the  $\geq 1$  *b*-tag category the BumpHunter, DeficitHunter and  $\chi^2$  *p*-values are 0.93, 0.77 and 0.86 respectively. Therefore, the fit is performing well for both *b*-tagging categories for this set of Poisson fluctuations.

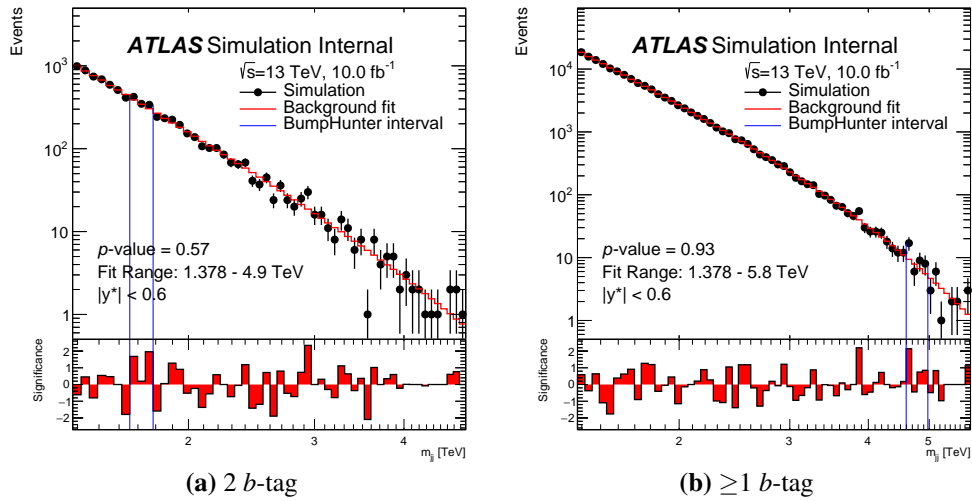


**Figure 7.9:** A data-like distribution taken from multi-jet simulation for the (a) 2  $b$ -tag and (b)  $\geq 1$   $b$ -tag, category, fitted to using the 3 parameter fit function. The BumpHunter algorithm is run to identify the most discrepant excess, as indicated by the blue lines. Pseudo-experiments are used to assign the excess a  $p$ -value, which is shown on the plot. The *Summer16+15* dataset event selection has been applied.

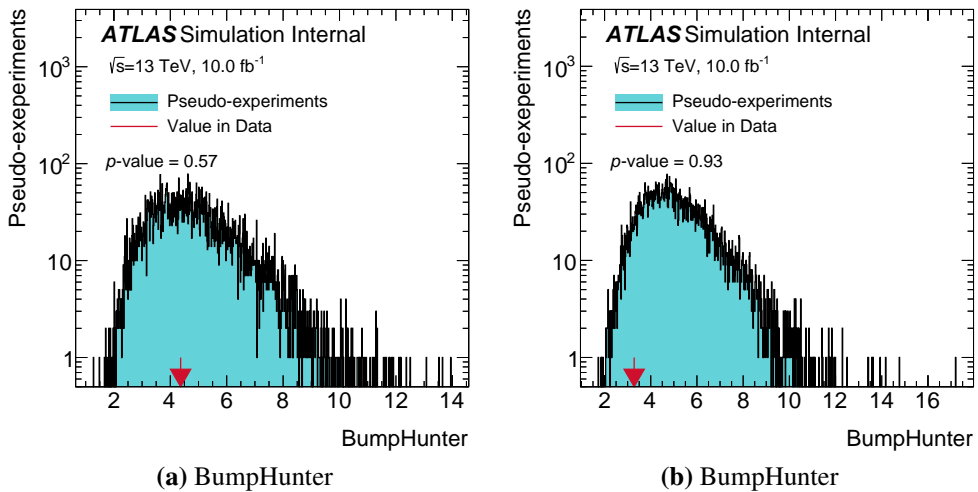


**Figure 7.10:** The distribution of the BumpHunter test statistic for 10,000 pseudo experiments compared to the value observed in a data-like distribution from the (a) 2  $b$ -tag category and (b)  $\geq 1$   $b$ -tag category. The fraction of pseudo-experiments with a BumpHunter test statistic greater than the value in data is the estimation of the respective  $p$ -value.

However, it is required to study the fit quality without being dependant on any one set of Poisson fluctuations. Therefore, different Poisson fluctuations are applied to the scaled distribution to give many different data-like distributions, and the search phase can be applied to each data-like distribution. Figure 7.11 and Figure 7.12 shows the distribution of BumpHunter, DeficitHunter and  $\chi^2$  *p*-values for 200 different data-like distributions, for the 2 *b*-tag and  $\geq 1$  *b*-tag category. There is no evidence of a fit-bias causing spurious signal in either category, which could be seen by a bias towards low BumpHunter *p*-values causing fake signals or a bias toward low DeficitHunter *p*-values causing fake deficits. The distribution of the  $\chi^2$  *p*-values also indicates that there is good fit quality in both tagging categories.

Hence, it can be concluded that the 3 parameter fit function is a good description of the simulated QCD background and that there is no evidence that spurious signal can occur. Similar tests were performed for the 4 parameter fit function but are not presented here because, as shown in Section 7.4.1, the 3 parameter function is chosen in both categories for this data-set.

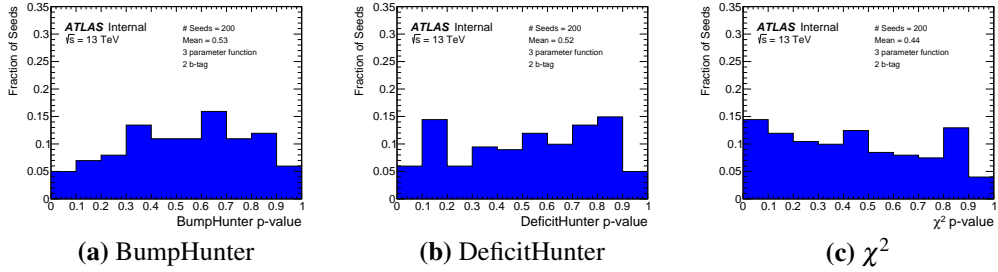


**Figure 7.11:** The distribution of (a) BumpHunter, (b) DeficitHunter and (c)  $\chi^2$  *p*-values for fits to 200 data-like invariant mass spectra in the 2 *b*-tag category. The *Summer16+15* dataset event selection has been applied.

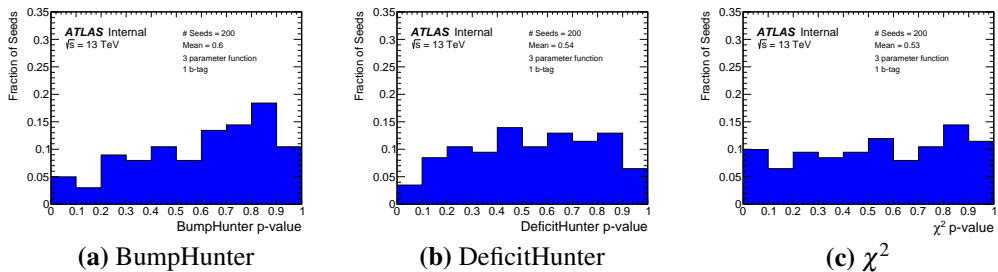


**Figure 7.12:** The distribution of (a) BumpHunter, (b) DeficitHunter and (c)  $\chi^2$  *p*-values for fits to 200 data-like invariant mass spectra in the  $\geq 1$  *b*-tag category. The *Summer16+15* dataset event selection has been applied.

#### 7.4.5 Search Phase

It has been shown that the 3 parameter dijet fit function has a sufficient number of parameters to provide an adequate background description in both *b*-tagging categories in the fit region that has been chosen and that there is no evidence that spurious signal can occur. Hence, for the *Summer16+15* data-set the 3 parameter fit function provides a valid background estimation in both categories.

Figure 7.13 shows the final *Summer16+15* data-set and the background estimate using the 3 parameter dijet fit function in the 2 and  $\geq 1$  *b*-tag categories. The upper panel shows the data compared to the background fit, in addition the benchmark signal models with enhanced cross sections have been overlaid. The lower panel shows the significance of the difference between the data and background estimate.

In both cases the BumpHunter algorithm has identified the most discrepant excess indicated in the figure using vertical blue lines. The BumpHunter *p*-value has been calculated

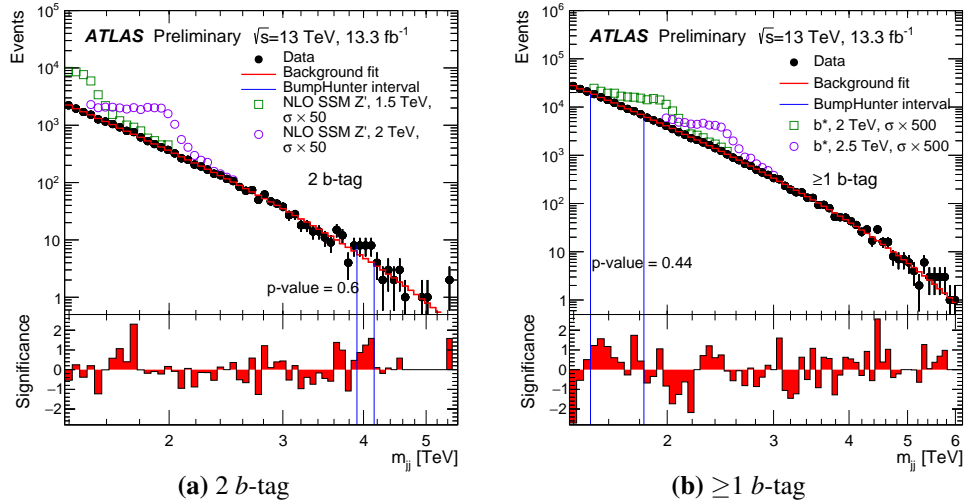


**Figure 7.13:** The final *Summer16+15* data-set in the (a) 2  $b$ -tag and the (b)  $\geq 1$   $b$ -tag category, where the background has been modelled using the 3 parameter dijet fit function. The upper panel shows the data compared to the background estimate, benchmark signal models with enhanced cross sections are overlaid. The lower panel shows the significance of the difference between the data and the background estimate. The most discrepant excess as found by the BumpHunter algorithm is indicated by the vertical blue lines and the  $p$ -value of this excess is printed on the plot [81].

using 10,000 pseudo-experiments. The BumpHunter  $p$ -value is 0.60 in the 2  $b$ -tag category and 0.44 in the  $\geq 1$   $b$ -tag category. Therefore, it can be concluded that no significant excess is found in either  $b$ -tag category and that there is no evidence of new physics in the Summer16+15 data-set.

## 7.5 Full\_2016 Search Phase

SWiFt and ect...

## Chapter 8

# Di-*b*-jet Search: Limit Setting

In Chapter 7 it was shown that there is no evidence of new physics in the di-*b*-jet spectra considered. However, it is also useful to quantify what this result means in the context of the signal models that we are searching for. Specifically, we can estimate the degree of belief that a signal model is true given the di-*b*-jet spectra that have been observed. If the degree of belief of a specific model is less than a certain threshold it is said that this model is excluded. This process is known as limit setting.

In this Chapter: Section 8.1 will describe the limit setting strategy used, Section 8.2 will discuss the systematic uncertainties considered and in Section 8.3 and Section 8.4 the results of the limit setting procedure for the various data-sets considered are shown.

## 8.1 Bayesian Limits

In this analysis a Bayesian limit setting approach is used [96]. For limit setting, one considers a hypothesis that the di-*b*-jet events are produced by a combination of the QCD background, which has been modelled by the background fit from the previous chapter, and some new physics process which produces  $\mu$  events according to some template shape in  $m_{jj}$ . This signal plus background hypothesis is denoted by the symbol  $H_\mu$ .

Now let us consider this hypothesis in the context of the data, denoted by  $D$ , which in this case is one of our observed di-*b*-jet spectra. For the hypothesis,  $H_\mu$ , the probability of producing the data is known as the “likelihood”. If, in each  $m_{jj}$  bin, the model predicts  $s_i(\mu)$  signal events,  $b_i$  background events and  $n_i$  events were observed in data. Then, by

only considering statistical uncertainties, the likelihood for a given value of  $\mu$  is given by

$$\mathcal{L}(\mu, D) = P(D | \mu) = \prod_i \frac{(s_i(\mu) + b_i)^{n_i} e^{-(s_i(\mu) + b_i)}}{n_i!} \quad (8.1)$$

where the product is over all  $m_{jj}$  bins.

Then, one can employ Bayes' theorem which states that

$$P(A | B) = \frac{P(B | A) P(A)}{P(B)} \quad (8.2)$$

to obtain the probability density function of  $\mu$  given the observed di-*b*-jet spectrum,

$$P(\mu | D) = \frac{P(D | \mu) \Pi(\mu)}{\Pi(D)} \quad (8.3)$$

This quantity, known as the posterior, is an expression of our confidence in the hypothesis  $H_\mu$  for any particular value of  $\mu$ .

The  $\Pi(\mu)$  term in the posterior is called the signal prior and gives the probability density of  $\mu$  before the experiment took place. For this experiment a flat signal prior was chosen<sup>1</sup> which represents ignorance to the size of the signal before the experiment. The  $\Pi(D)$  term does not depend on  $\mu$  and as such can be considered as a normalisation term.

However, to accurately represent a true degree of belief in a model one must consider systematic uncertainties, which are uncertainties in the model's predictions. The systematic uncertainties considered in this analysis are listed below in Section 8.2. The systematic uncertainties are incorporated by making  $s_i$  and  $b_i$  a function of a set of nuisance parameters,  $\vec{\theta}$ , where each nuisance parameter models the effect of a systematic uncertainty. Therefore likelihood becomes a function of the nuisance parameters

$$\mathcal{L}(\mu, D, \vec{\theta}) = P(D | \mu, \vec{\theta}) \quad (8.4)$$

The effect of the systematic uncertainties are then propagated to the posterior. To do this a prior is introduced for each the nuisance parameters, given by  $\Pi(\vec{\theta})$ , that describes the probability distribution of the nuisance parameters. Then, by integrating over the nuisance

---

<sup>1</sup>Flat from  $\mu = 0$  to the value of  $\mu$  where the likelihood has fallen to  $10^{-5}$  of the optimal likelihood value.

parameters, one obtains the probability density function for  $\mu$  that includes the systematic uncertainties

$$P(\mu | D) \propto \int d\vec{\theta} \mathcal{L}(\mu, D, \vec{\theta}) \Pi(\mu) \Pi(\vec{\theta}) \quad (8.5)$$

One can calculate the likelihoods for the data, perform the integral over nuisance parameters and then normalise to calculate the probability density of  $\mu$ <sup>2</sup>.

Using the posterior calculated from Equation 8.5, the 95% confidence level upper limit of  $\mu$ , denoted by  $\mu_{up}$ , is calculated using the expression

$$\int_0^{\mu_{up}} P(\mu | D) = 0.95 \quad (8.6)$$

The 95% confidence upper limit defines a confidence region ( $0 < \mu < \mu_{up}$ ) that will contain the true value of  $\mu$  with 95% confidence. Any model under the hypothesis  $H_\mu$  that predicts a  $\mu$  value outside of this region is said to be excluded at the 95% confidence level.

In the di- $b$ -jet analysis limits are set using the benchmark signal model templates for a range of mass points, as described in Section 6.3. The limits are presented in terms of the product of cross-section, detector acceptance and tagging efficiency,  $\sigma \times A \times \epsilon$ , which is related to the parameter  $\mu$  used in the limit setting description<sup>3</sup>. Further to this many BSM models predicting a narrow resonance not explicitly considered by this analysis can be approximated by a Gaussian distribution, if low-mass off-shell tails and non-perturbative effects are neglected. Therefore, limits are set using a signal template with a Gaussian shape, which can be reinterpreted for a wider range of models.

The di- $b$ -jet analysis will present two limits, which is typical of searches at ATLAS. The first is the observed limit, which is the limit using the observed di- $b$ -spectra as  $D$ , which was described above. The second is the expected limit under the assumption that there is no signal in the di- $b$ -jet spectrum. To calculate the expected limit the procedure is performed where  $D$  is replaced by pseudo-experiments created by varying the background estimate within the systematic uncertainties. This process can be done for many pseudo-experiments; the median upper limit found gives the expected limit and the 68% and 95% percentiles give the 1 and 2  $\sigma$  uncertainty bands on the expected limit.

---

<sup>2</sup>This integral is performed using a Monte-Carlo Markov chain using the Bayesian Analysis Toolkit. Full details on the implementation can be found here [11].

<sup>3</sup>Specifically  $\mu = \sigma / L$ , where  $L$  is the luminosity.  $A$  and  $\epsilon$  have been measured in Section 6.4.4.

In this analysis the Bayesian approach for limit setting is used, while there is another widely used approach known as the frequentist approach. The Bayesian approach defines a confidence region using the probability (or degree of belief) in a hypothesis given the observed data ( $P(\mu | D)$ ). On the other hand, the frequentist approach calculates the probability (or fraction of trials) of obtaining the data assuming a given signal model is true ( $P(D | \mu)$ ) and rejects models that produce a low probability [97]. Both approaches are valid and logically consistent, but it is important that one states clearly which approach is being taken.

## 8.2 Systematic Uncertainties

As discussed in the previous section, systematic uncertainties are an important consideration in limit-setting. They describe the uncertainty in the signal or background prediction and are accounted for in the limit setting procedure through the inclusion of nuisance parameters.

The systematic uncertainties in the di- $b$ -jet analysis considered are grouped into two categories [81]. The first are uncertainties on the signal  $m_{jj}$  templates used in the limit setting procedure. Simulated Monte-Carlo signal templates are used, hence a range of systematic uncertainties of the simulation are required. The signal systematic uncertainties considered are:

- **Jet Energy Scale, Jet Energy Resolution and  $b$ -Jet Energy Scale (Signal):**

Jet energy scale (JES) and jet energy resolution (JER) are uncertainties in the measurement of the jet energy, which causes an uncertainty in the  $m_{jj}$  signal template. The JES and JER uncertainties used in this analysis were described in Section 4.2.4. In addition, there is also an additional  $b$ -jet energy scale ( $b$ JES) uncertainty which has been described in Section 4.3.5.

- **$b$ -Tagging (Signal):**

The  $b$ -tagging modelling in Monte-Carlo simulation is calibrated to data using measured  $b$ -tagging scale factors, the scale factors and associated uncertainties are discussed in Section 4.3.4. Variations of the  $b$ -tagging scale factors within uncertainties can vary the signal template. The  $b$ -tagging systematic uncertainty is large at high values of jet- $p_T$ , and as such is the dominant uncertainty in this analysis.

- ***b*-Jet Trigger (Signal):**

Similarly, when using the  $b$ -jet trigger, the online  $b$ -tagging is corrected to data using  $b$ -jet trigger scale factors. The  $b$ -jet trigger scale factors and relevant uncertainties are derived in Section 5.3. These systematic uncertainties are only used in the `Full16_LowMass` data-set, as this is the only data-set using a  $b$ -jet trigger.

- **Luminosity (Signal):**

The luminosity uncertainty is determined using the methodology outlined in [98] from van der Meer scans performed in August 2015 and May 2016. The luminosity uncertainties used are 2.9% in the `Summer16+15` data-set, 2.2% in the `Full16_LowMass` data-set and 2.1% in the `Full16+15_HighMass` data-set.

- **Parton Distribution Functions (PDFs) (Signal):**

The PDFs are important in calculating the cross-section of any process at the LHC. As shown in Section 2.2.3.3 there are uncertainties on the measurements of the PDFs, which causes an uncertainty in the signal template used. A flat 1% uncertainty from the PDFs is considered, which has been found at previous dijet searches to conservatively cover the effect of the PDF uncertainties [87].

The second group of systematic uncertainties are systematic uncertainties of the background estimate. As the background estimate is data-driven, the large range of simulation modelling uncertainties considered for the signal model are not required. The uncertainties on the background estimation model are:

- **Fit Function Parameters (Background):**

The choice of fit parameters is made by maximising the likelihood of the fit function with respect to our data-set. However, due to the statistical fluctuations in data the optimal parameters to describe the true background shape may not have been chosen. To estimate the uncertainty on the choice of parameters, pseudo-experiments are created by applying Poisson fluctuations to the background estimate and then running the background estimation fit procedure on the pseudo-experiments. The *rms* of the difference between the nominal background estimate on data to those from the pseudo-experiments is taken as a symmetric uncertainty.

- **Fit Function Choice (Background):**

A different background estimation can be obtained if a different fit function is chosen. To obtain a uncertainty on our choice of fit function an alternate function is considered, which is the dijet fit function with one extra degree of freedom than the nominal function. The alternate function is then used to fit to the pseudo-experiments described in the previous bullet point and the mean of the difference between the nominal and alternate functions is taken as a one-sided uncertainty.

### 8.3 Limits: 2016\_Summer

Table 8.1 summarises the systematic uncertainties on the signal template used in the Summer16+15 data-set at three different values of dijet invariant mass  $m_{jj}$ . Figure 8.1 shows the systematics on the background in the two  $b$ -tagging categories as a function dijet invariant mass,  $m_{jj}$ .  $b$ -tagging is the dominant systematic for the full range of  $m_{jj}$ .

$m_{jj}$	Signal Systematic Uncertainties					
	JES	JER	$b$ JES	$b$ -Tagging ( $\geq 1 / 2$ )	PDF	Lumi
1.5 TeV	1.2%	1.0%	2.2%	20% / 10%	1%	2.9%
3 TeV	1.4%	0.7%	0.7%	50% / 60%	1%	2.9%
5 TeV	2.3%	0.3%	0.3%	50% / 70%	1%	2.9%

**Table 8.1:** A table summarising the signal systematic uncertainties used in the *Summer16+15* data-set. Jet Energy Scale (JES), Jet Energy Resolution (JER) and  $b$ -Jet Energy Scale ( $b$ JES) are uncertainties on the dijet invariant mass of a simulated event, whilst  $b$ -tagging, PDF and luminosity uncertainties are uncertainties on simulated event weight. Values taken from [88].

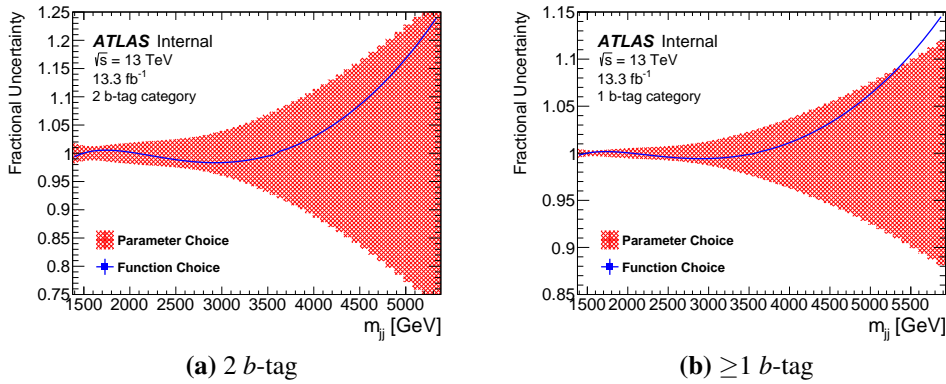


**Figure 8.1:** The background systematic uncertainties for the (a) 2 and (b)  $\geq 1$   $b$ -tag categories as a function of dijet invariant mass,  $m_{jj}$ , for the *Summer16+15* data-set. The red shaded region shows the function parameter uncertainty and the function choice uncertainty is shown by the blue line.

Figure 8.2 shows the 95% confidence level upper limits set on  $\sigma \times A \times \epsilon$  as a function of simulated mass for the  $Z'$ -boson and a  $b^*$ -quark. The observed limit, the expected limit and the  $1$  and  $2 \sigma$  error bands on the expected limit are shown. The  $\geq 1 b$ -tag category is used for the  $b^*$ -quark model and the  $2 b$ -tag category is used for the  $Z'$ -boson models as these categories provide the strongest limits on the models. Overlaid are theoretical predictions of  $\sigma \times A \times \epsilon$  for the benchmark models described in Section 6.3.

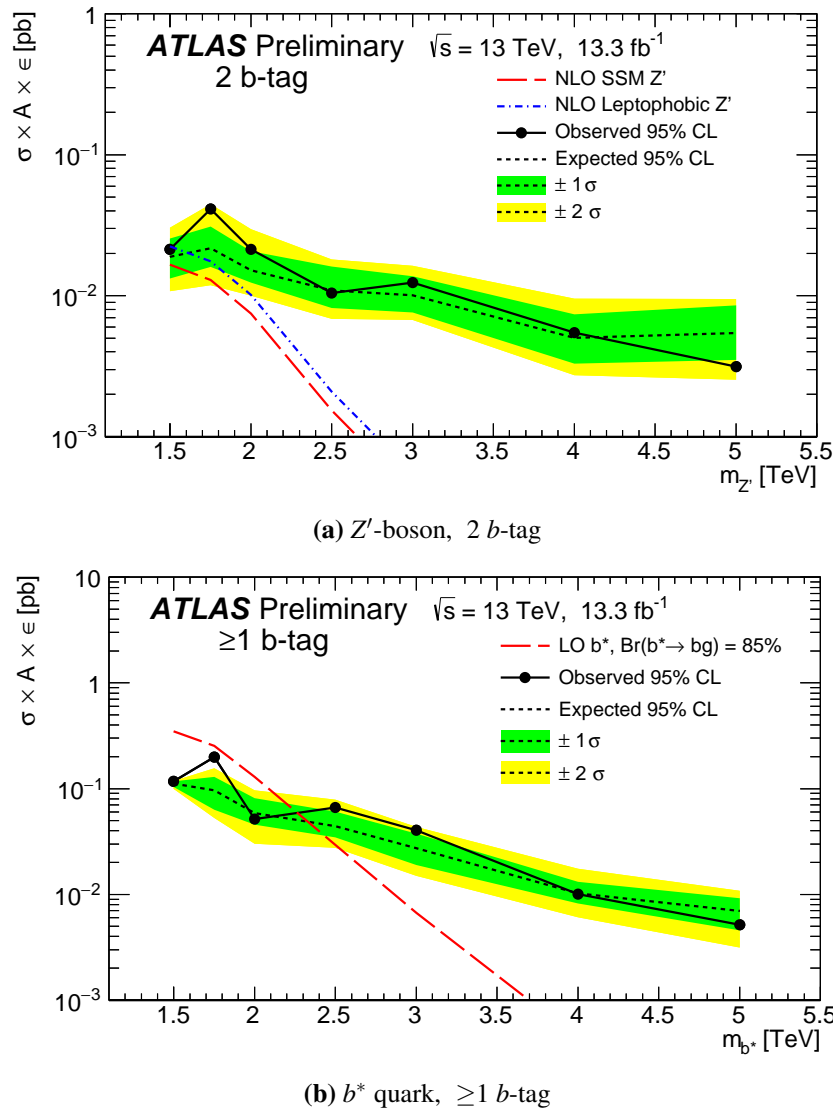


**Figure 8.2:** Bayesian 95% confidence level upper limits on cross-section times acceptance times tagging efficiency for the (a)  $Z'$ -boson and (b)  $b^*$ -quark as a function of simulated mass using the *Summer16+15* data-set in the 2 and  $\geq 1 b$ -tag category respectively. The observed limit is shown by the solid black line, the expected limit is shown by the dotted black line and the  $1$  and  $2 \sigma$  error bands on the expected limit are shown by the green and yellow bands. The theoretical prediction of  $\sigma \times A \times \epsilon$  for the Sequential Standard Model (SSM) and leptophobic  $Z'$ -boson and the  $b^*$ -quark are overlaid [81].

The observed and expected limits decrease with increasing simulated mass due to reduced number of background events at higher mass. The theoretical  $\sigma \times A \times \epsilon$  predictions decrease rapidly as mass increases, due to a combination of lower signal acceptance times efficiency at high mass, as shown in Figures 6.6, and a smaller signal cross-section at high mass. The signal cross-section is smaller at high mass because of PDF and matrix element effects, similar to those that caused a smaller QCD dijet production at high mass as described in Section 2.2.3.4.

In the mass regions where the theoretical prediction of  $\sigma \times A \times \epsilon$  is larger than the upper limit, it can be concluded that the model is excluded at the 95% confidence level. Using the `Summer16+15` data-set: the  $b^*$ -quark is excluded in the mass range of 1.38 - 2.3 TeV, the SSM  $Z'$ -boson cannot be excluded, and the leptophobic  $Z'$ -boson is excluded at a mass of 1.5 TeV.

For the generic Gaussian limit setting procedure, a signal template with a Gaussian shape in dijet invariant mass is used. The Gaussian shapes are centered on a range of masses and the width of the considered Gaussians are 15%, 10% and 7% of the simulated mass in addition to a Gaussian with the width of the detector mass resolution. The detector mass resolution has been estimated at previous dijet searches [87] and varies from 3% at 1.5 TeV to 2% at 5 TeV. For the Gaussian limit setting systematic uncertainties come from the luminosity uncertainty, the background modelling uncertainties, and an additional 10% flat uncertainty to incorporate sources of systematic uncertainties related to signal modeling  
**LM question. Why 10%? Much less than the other signal models.**

Figure 8.3 shows the observed 95% confidence upper limits on the product of cross-section, detector acceptance, tagging efficiency and branching ratio,  $\sigma \times A \times \epsilon \times BR$ , for the full range of Gaussian signals described above in both  $b$ -tagging categories. For the `Summer16+15` an upper limit is placed on a generic Gaussian signal ranging from 0.2 to 0.001 pb is set in the mass range 1.4 to 6 TeV.

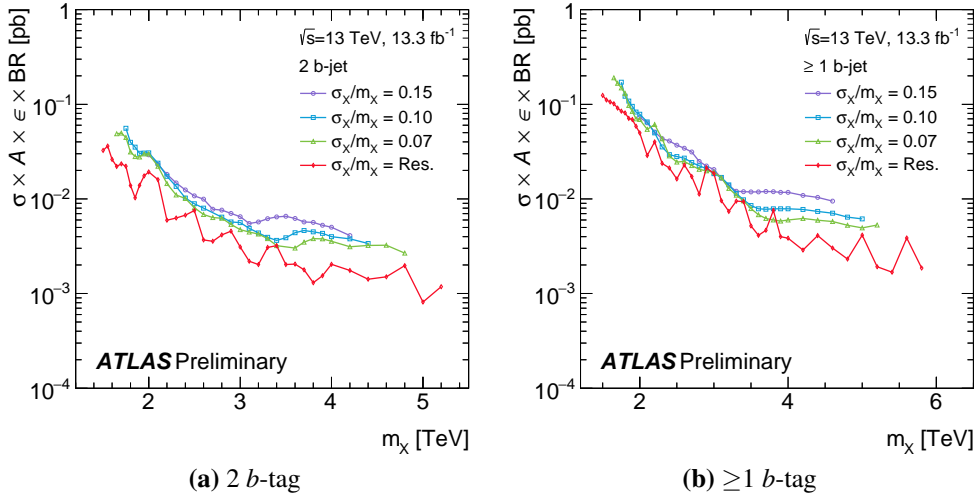


**Figure 8.3:** 95% confidence observed upper limits on the product of cross-section, detector acceptance, tagging efficiency and branching ratio,  $\sigma \times A \times \varepsilon \times BR$ , for Gaussian signals for both  $b$ -tagging categories using the *Summer16+15* data-set. The Gaussian widths considered are 15%, 10% and 7% of the simulated mass in addition to a Gaussian with the width of the detector mass resolution [81].

## 8.4 Limits: 2016\_Full

## To do...

## **Chapter 9**

# **General Conclusions**

Lorem ipsum dolor sit amet, consectetuer adipiscing elit. Etiam lobortis facilisis sem. Nullam nec mi et neque pharetra sollicitudin. Praesent imperdiet mi nec ante. Donec ullamcorper, felis non sodales commodo, lectus velit ultrices augue, a dignissim nibh lectus placerat pede. Vivamus nunc nunc, molestie ut, ultricies vel, semper in, velit. Ut porttitor. Praesent in sapien. Lorem ipsum dolor sit amet, consectetuer adipiscing elit. Duis fringilla tristique neque. Sed interdum libero ut metus. Pellentesque placerat. Nam rutrum augue a leo. Morbi sed elit sit amet ante lobortis sollicitudin. Praesent blandit blandit mauris. Praesent lectus tellus, aliquet aliquam, luctus a, egestas a, turpis. Mauris lacinia lorem sit amet ipsum. Nunc quis urna dictum turpis accumsan semper.

## **Appendix A**

### **Dijet Binning**

The binning used in the di-*b*-jet analysis is:

203, 216, 229, 243, 257, 272, 287, 303, 319, 335, 352, 369,  
387, 405, 424, 443, 462, 482, 500, 523, 544, 566, 588, 611,  
634, 657, 681, 705, 730, 755, 781, 807, 834, 861, 889, 917,  
946, 976, 1006, 1037, 1068, 1100, 1133, 1166, 1200, 1234,  
1269, 1305, 1341, 1378, 1416, 1454, 1493, 1533, 1573, 1614,  
1656, 1698, 1741, 1785, 1830, 1875, 1921, 1968, 2016, 2065,  
2114, 2164, 2215, 2267, 2320, 2374, 2429, 2485, 2542, 2600,  
2659, 2719, 2780, 2842, 2905, 2969, 3034, 3100, 3167, 3235,  
3305, 3376, 3448, 3521, 3596, 3672, 3749, 3827, 3907, 3988,  
4070, 4154, 4239, 4326, 4414, 4504, 4595, 4688, 4782, 4878,  
4975, 5074, 5175, 5277, 5381, 5487, 5595, 5705, 5817, 5931,  
6047, 6165, 6285, 6407, 6531, 6658, 6787, 6918, 7052, 7188,  
7326, 7467, 7610, 7756, 7904, 8055, 8208, 8364, 8523, 8685,  
8850, 9019, 9191, 9366, 9544, 9726, 9911, 10100, 10292,  
10488, 10688, 10892, 11100, 11312, 11528, 11748, 11972,  
12200, 12432, 12669, 12910, 13156

## **Appendix B**

# **Colophon**

*This is a description of the tools you used to make your thesis. It helps people make future documents, reminds you, and looks good.*

(example) This document was set in the Times Roman typeface using L<sup>A</sup>T<sub>E</sub>X and Bib<sup>L</sup>T<sub>E</sub>X, composed with a text editor.

## **Appendix C**

# **Contents Plan**

A few notes from Laurie:

The aim is to be concise and to focus on what I used and did. If I have not done or used something then I should not write it much detail about it. Christian Gutchow did it in 100 pages including everything, this shows that it can be concise!

### **C.1 Introduction**

**Status: Not Started**

- Introduce basics of analysis
- Explain why each section fits into larger picture

### **C.2 Theoretical Background**

**Status: First Draft Done**

### **C.3 ATLAS Detector**

**Status: First Draft Done**

Still needs cleaning and response to comments

I want to add pile-up and calo noise here.

## C.4 Object Reconstruction And Calibration

### Status : First Draft Done

Needs editing Want to add primary vertexing Add in some discussion of high pT b-tagging

## C.5 Trigger

### Status : First draft done

Move trigger description here.

Needs a bit more cleaning and a bit of upmarketing.

## C.6 Event Selection

**Status: First Draft with summer16 done** Need to add: Full 16 + 15 data-set

## C.7 Background Estimation and Search Phase

**Status: First Draft with summer16 done** Need to add: Full 16 + 15 data-set

## C.8 Systematics and Limits Setting

**Status: First Draft with summer16 done** Need to add: Full 16 + 15 data-set

## C.9 Looking Forward - What more can be done?

### Status: Not started

- Combination of b-tagging channels
  - Refer to CMS paper and the way they do it. We probably should have done this.
- 1 b-tag low mass

- See if appropriate trigger exists, could be done...
- bTrigger efficiency.
  - Optimise purity selection, bTrigger combined with offline b-tagging, (i.e. one systematic.)

## C.10 Rough list of things I have done

Note from Laurie: Apologies, the stuff in italics is useful for me, and probably not for anyone else.

## C.11 2014/15 - High $p_T$ b-tagging

*See 2015\_09\_EndOfFirstYear.pdf and 15\_05\_TrackStudies.pdf*

- Studied pt distribution of tracks from different origin
- Found a cut that would be able to increase selection of tracks from B-hadron
- Suggested that this is taken into b-tagging algorithms I think this is interesting, but I didn't really drive this through. I think some version of this was adopted, can I refer to this.

## C.12 2015 - Validation of b-tagging in dijet events

*See https://cds.cern.ch/record/2032461, 15\_09\_CTIDE.pdf, 2015\_09\_EndOfFirstYear.pdf*

- Setup - selecting jets
- Comparison of bunch of variables
- Spot discrepancy in data in IP3D
- What could be the problem
  - IBL Geometry
- b-jet enhanced selection
- New geometry comparisons

*See 16\_08\_newGeoComp.pdf*

## C.13 2015 Di-b-jet - Moriond

- Background flavour fraction studies.
- Plot flavour fraction.
- Show robustness with respect to flavour fraction changes.
  - Extract flavour fractions
  - Fit to individual flavour fractions

- Combine in various ways and re-fit  
(See *16\_03\_FlavourFit\_bumpHunter.pdf*)

- VP1 Displays ( : ] )

## C.14 2015 low mass Di-b-jet - LHCP

- LHCP low mass MC studies. Difficult to do...
- Flavour composition studies, various iterations.
- Emulated trigger, emulated offline b-tagging, trigger from MC.
- Fitting studies with MC and fitting CR.
- Changing fit CR, spurious signal

*16\_05\_dibjet\_spuriousSignal\_EB2.pdf*

- Effect on limits of any spurious signal.
- Search for deficits in spectrum.
- What happens if you play with parameter 2 of fit.

*(16\_06\_dibjet\_S+B\_Check.pdf)*

## C.15 Half 2016 high mass Di-b-jet - ICHEP

- Fitting studies with MC.
- Mass cut choice from MC fitting
- Spurious signal check.
- Background flavour fraction.

*(16\_07\_mjjCut\_pValues\_INTnote.pdf).*

## C.16 2017 - bTrigger

See *bTriggerEfficiencies\_00-02-01.pdf*

- Event selection
- Derivation of efficiency
- Investigation
  - We spot problem, early plots period A-F
  - Split into regions correctly
  - Observation of dependance w.r.t online beamspot position
  - Suggestion of GRL creation of GRL

*See 17\_01\_Trig\_full.pdf*

- Jet-level Efficiency
  - Purity Systematic
  - Light Eff. Systematic
  - Extrapolation to high pT
  - Result
- Event-level correction
  - Systematics and measurement
  - Cross-checks, including on subleading jet.

*See 17\_01\_bTrigPres\_bPerf\_Eta.pdf*

## C.17 Full 2016 low mass Di-b-jet

- Analysis contact:
  - Followed and reviewed all aspects of analysis closely,
  - note editing, close interaction with paper editors ;),
  - representation of analysis in approval process.
- Event Selection:
  - Trigger turn-on
  - OP selection (with Nishu)
  - $y^*$  selection (with Bing).
- Fit studies:
  - Global fit fails

- SWiFt: Window selection procedure
- SWiFt: Spurious signal for various wHW and fit functions
- SWiFt: Signal injection tests

## **C.18 Event Display**

- Was on call expert for 18 months

# Bibliography

- [1] Sylvia Berryman. Ancient atomism, 2005. <https://plato.stanford.edu/archives/fall2008/entries/atomism-ancient/>.
- [2] Professor E. Rutherford F.R.S. Lxxix. the scattering of  $\alpha$  and  $\beta$  particles by matter and the structure of the atom. *Philosophical Magazine*, 21(125):669–688, 1911.
- [3] C. Patrignani et al. Review of Particle Physics. *Chin. Phys.*, C40(10):100001, 2016.
- [4] Boris Kayser. Neutrino Mass, Mixing, and Flavor Change. 2008.
- [5] S. L. Glashow. Partial Symmetries of Weak Interactions. *Nucl. Phys.*, 22:579–588, 1961.
- [6] S. Bethke and G. Dissertori and G. P. Salam. Quantum Chromodynamics, 2015. <http://pdg.lbl.gov/2015/reviews/rpp2015-rev-qcd.pdf>.
- [7] F. Englert and R. Brout. Broken symmetry and the mass of gauge vector mesons. *Phys. Rev. Lett.*, 13:321–323, Aug 1964.
- [8] Peter W. Higgs. Broken symmetries and the masses of gauge bosons. *Phys. Rev. Lett.*, 13:508–509, Oct 1964.
- [9] ATLAS Collaboration. Observation of a new particle in the search for the standard model higgs boson with the atlas detector at the lhc. *Physics Letters B*, 716(1):1 – 29, 2012.
- [10] CMS Collaboration. Observation of a new boson at a mass of 125 GeV with the CMS experiment at the LHC. *Phys. Lett.*, B716:30–61, 2012.
- [11] Katherine Pachal. Search for new physics in the dijet invariant mass spectrum at 8 TeV, Jan 2015. Presented 01 Jun 2015.

- [12] Bo Andersson, G. Gustafson, G. Ingelman, and T. Sjostrand. Parton Fragmentation and String Dynamics. *Phys. Rept.*, 97:31–145, 1983.
- [13] B.R. Webber. A qcd model for jet fragmentation including soft gluon interference. *Nuclear Physics B*, 238(3):492 – 528, 1984.
- [14] John Butterworth. This is not a measurement, 2015. <https://www.theguardian.com/science/life-and-physics/2015/jan/10>this-is-not-a-measurement>.
- [15] Christine A. Aidala, Steven D. Bass, Delia Hasch, and Gerhard K. Mallot. The Spin Structure of the Nucleon. *Rev. Mod. Phys.*, 85:655–691, 2013.
- [16] Robert M. Harris and Konstantinos Kousouris. Searches for Dijet Resonances at Hadron Colliders. *Int. J. Mod. Phys.*, A26:5005–5055, 2011.
- [17] F. D. Aaron et al. Combined Measurement and QCD Analysis of the Inclusive e+ p Scattering Cross Sections at HERA. *JHEP*, 01:109, 2010.
- [18] L. A. Harland-Lang, A. D. Martin, P. Motylinski, and R. S. Thorne. Parton distributions in the lhc era: Mmht 2014 pdfs. *The European Physical Journal C*, 75(5):204, May 2015.
- [19] T. Aaltonen et al. Observation of Single Top Quark Production and Measurement of —Vtb— with CDF. *Phys. Rev.*, D82:112005, 2010.
- [20] Michael E. Peskin. Dark matter and particle physics. *J. Phys. Soc. Jap.*, 76:111017, 2007.
- [21] M. Roos. Dark Matter: The evidence from astronomy, astrophysics and cosmology. *ArXiv e-prints*, January 2010.
- [22] Jonathan L. Feng. Dark Matter Candidates from Particle Physics and Methods of Detection. *Ann. Rev. Astron. Astrophys.*, 48:495–545, 2010.
- [23] Paul Langacker. The Physics of Heavy  $Z'$  Gauge Bosons. *Rev. Mod. Phys.*, 81:1199–1228, 2009.

- [24] Search for new high-mass phenomena in the dilepton final state using  $36.1 \text{ fb}^{-1}$  of proton-proton collision data at  $\sqrt{s} = 13 \text{ TeV}$  with the ATLAS detector. Technical Report ATLAS-CONF-2017-027, CERN, Geneva, Apr 2017.
- [25] Cheng-Wei Chiang, Takaaki Nomura, and Kei Yagyu. Phenomenology of  $E_6$ -Inspired Leptophobic  $Z'$  Boson at the LHC. *JHEP*, 05:106, 2014.
- [26] Andreas Albert et al. Recommendations of the LHC Dark Matter Working Group: Comparing LHC searches for heavy mediators of dark matter production in visible and invisible decay channels. 2017.
- [27] Durmus A. Demir, Gordon L. Kane, and Ting T. Wang. The Minimal  $U(1)'$  extension of the MSSM. *Phys. Rev.*, D72:015012, 2005.
- [28] U. Baur, I. Hinchliffe, and D. Zeppenfeld. Excited Quark Production at Hadron Colliders. *Int. J. Mod. Phys.*, A2:1285, 1987.
- [29] G. Arnison et al. Experimental Observation of Isolated Large Transverse Energy Electrons with Associated Missing Energy at  $s^{1/2} = 540 \text{ GeV}$ . *Phys. Lett.*, 122B:103–116, 1983. [,611(1983)].
- [30] G. Arnison et al. Experimental Observation of Lepton Pairs of Invariant Mass Around  $95\text{-GeV}/c^2$  at the CERN SPS Collider. *Phys. Lett.*, 126B:398–410, 1983.
- [31] M. Banner et al. Observation of Single Isolated Electrons of High Transverse Momentum in Events with Missing Transverse Energy at the CERN anti-p p Collider. *Phys. Lett.*, 122B:476–485, 1983.
- [32] P. Bagnaia et al. Evidence for  $Z_0 \rightarrow e^+e^-$  at the CERN anti-p p Collider. *Phys. Lett.*, 129B:130–140, 1983.
- [33] F. Abe et al. Observation of top quark production in  $\bar{p}p$  collisions with the collider detector at fermilab. *Phys. Rev. Lett.*, 74:2626–2631, Apr 1995.
- [34] S. Abachi et al. Observation of the top quark. *Phys. Rev. Lett.*, 74:2632–2637, Apr 1995.
- [35] Atlas public lumi results run-2. <https://twiki.cern.ch/twiki/bin/view/AtlasPublic/LuminosityPublicResultsRun2>.

- [36] G. Aad et al. The ATLAS Experiment at the CERN Large Hadron Collider. *JINST*, 3:S08003, 2008.
- [37] A. Airapetian et al. *ATLAS detector and physics performance: Technical Design Report, 1.* Technical Design Report ATLAS. CERN, Geneva, 1999.
- [38] G. Aad et al. Performance of the atlas detector using first collision data. *Journal of High Energy Physics*, 2010(9):56, Sep 2010.
- [39] C Gutschow. First observation of electroweak z boson plus two jet production, October 2014.
- [40] M Capeans, G Darbo, K Einsweiller, M Elsing, T Flick, M Garcia-Sciveres, C Gemme, H Pernegger, O Rohne, and R Vuillermet. ATLAS Insertable B-Layer Technical Design Report. Technical Report CERN-LHCC-2010-013. ATLAS-TDR-19, Sep 2010.
- [41] C Gemme. The ATLAS Insertable B-Layer (IBL) Project. Jul 2011.
- [42] Claude Leroy and Pier-Giorgio Rancoita. *Principles of Radiation Interaction in Matter and Detection*. World Scientific, 2016.
- [43] Michele Livan and Richard Wigmans. Misconceptions about Calorimetry. *Instruments*, 1(1):3, 2017.
- [44] Lene Bryngemark, Torsten AKESSON, Else LYTKEN, and Johan RATHSMAN. Search for new phenomena in dijet angular distributions at  $s = 8$  and 13 TeV, Feb 2016. Presented 18 Mar 2016.
- [45] J.J. Goodson. *Search for Supersymmetry in States with Large Missing Transverse Momentum and Three Leptons including a Z-Boson*. PhD thesis, Stony Brook University, May 2012. Presented 17 Apr 2012.
- [46] Georges Aad et al. Technical Design Report for the Phase-I Upgrade of the ATLAS TDAQ System. Technical Report CERN-LHCC-2013-018. ATLAS-TDR-023, Sep 2013. Final version presented to December 2013 LHCC.
- [47] Morad Aaboud et al. Performance of the ATLAS Trigger System in 2015. *Eur. Phys. J.*, C77(5):317, 2017.

- [48] ATLAS Collaboration. Performance of the ATLAS Track Reconstruction Algorithms in Dense Environments in LHC run 2. 2017.
- [49] R. Frhwirth. Application of kalman filtering to track and vertex fitting. *Nuclear Instruments and Methods in Physics Research Section A: Accelerators, Spectrometers, Detectors and Associated Equipment*, 262(2):444 – 450, 1987.
- [50] H. Kirschenmann. Jets at cms and the determination of their energy scale. <http://cms.web.cern.ch/news/jets-cms-and-determination-their-energy-scale>.
- [51] ATLAS Collaboration. Evidence for the  $H \rightarrow b\bar{b}$  decay with the ATLAS detector. 2017.
- [52] ATLAS Collaboration. Topological cell clustering in the atlas calorimeters and its performance in lhc run 1. *The European Physical Journal C*, 77(7):490, Jul 2017.
- [53] Gavin P. Salam. Towards jetography. *arXiv:0906.1833*, 2009.
- [54] G. Arnison et al. Hadronic Jet Production at the CERN Proton - anti-Proton Collider. *Phys. Lett.*, 132B:214, 1983.
- [55] Matteo Cacciari, Gavin P. Salam, and Gregory Soyez. The Anti-k(t) jet clustering algorithm. *JHEP*, 04:063, 2008.
- [56] ATLAS Collaboration. Jet Calibration and Systematic Uncertainties for Jets Reconstructed in the ATLAS Detector at  $\sqrt{s} = 13$  TeV. Technical Report ATL-PHYS-PUB-2015-015, CERN, Geneva, Jul 2015.
- [57] ATLAS Collaboration. Jet energy scale measurements and their systematic uncertainties in proton-proton collisions at  $\sqrt{s} = 13$  TeV with the ATLAS detector. 2017.
- [58] ATLAS Collaboration. Search for diboson resonances with boson-tagged jets in  $pp$  collisions at  $\sqrt{s} = 13$  TeV with the ATLAS detector. 2017.
- [59] ATLAS Collaboration. Data-driven determination of the energy scale and resolution of jets reconstructed in the atlas calorimeters using dijet and multijet events at  $\sqrt{s} = 8$  tev. Technical Report ATLAS-CONF-2015-017, CERN, Geneva, Apr 2015.

- [60] ATLAS Collaboration. Measurements of top-quark pair differential cross-sections in the  $e\mu$  channel in  $pp$  collisions at  $\sqrt{s} = 13$  TeV using the ATLAS detector. *Eur. Phys. J.*, C77(5):292, 2017.
- [61] Expected performance of the ATLAS  $b$ -tagging algorithms in Run-2. Technical Report ATL-PHYS-PUB-2015-022, CERN, Geneva, Jul 2015.
- [62] Optimisation of the ATLAS  $b$ -tagging performance for the 2016 LHC Run. Technical Report ATL-PHYS-PUB-2016-012, CERN, Geneva, Jun 2016.
- [63] Calibration of  $b$ -tagging using dileptonic top pair events in a combinatorial likelihood approach with the ATLAS experiment. Technical Report ATLAS-CONF-2014-004, CERN, Geneva, Feb 2014.
- [64] ATLAS Collaboration.  $b$ -tagging calibration plots using dileptonic  $t\bar{t}$  events produced in  $pp$  collisions at  $s=13$  tev and a combinatorial likelihood approach, 2016.
- [65] Gordon Watts, Frank Filthaut, and Giacinto Piacquadio. Extrapolating Errors for  $b$ -tagging. Technical Report ATL-COM-PHYS-2015-711, CERN, Geneva, Jul 2015.  
This is for internal information only, no approval to ever be seen outside of ATLAS.
- [66] Jeremy Love, Andrea Coccato, Andreas Korn, Sergei Chekanov, Jeffrey Rogers Dandoy, Francesco Gescini, Thomas LeCompte, Laurie McClymont, James Proudfoot, Soo Ryu, Rui Wang, Ning Zhou, Gabriel Facini, Tobias Golling, and Nishu Nishu. Search for Resonances in the Mass Spectrum of  $b$ -Tagged Jets with the ATLAS Detector. Technical Report ATL-PHYS-INT-2016-022, CERN, Geneva, Oct 2016.
- [67] ATLAS Collaboration. Electron efficiency measurements with the ATLAS detector using the 2015 LHC proton-proton collision data. Technical Report ATLAS-CONF-2016-024, CERN, Geneva, Jun 2016.
- [68] ATLAS Collaboration. Muon reconstruction performance of the ATLAS detector in protonproton collision data at  $\sqrt{s}=13$  TeV. *Eur. Phys. J.*, C76(5):292, 2016.
- [69] ATLAS Collaboration. Measurement of the photon identification efficiencies with the ATLAS detector using LHC Run-1 data. 2016.

- [70] ATLAS Collaboration. Reconstruction, Energy Calibration, and Identification of Hadronically Decaying Tau Leptons in the ATLAS Experiment for Run-2 of the LHC . 2015.
- [71] ATLAS Collaboration. Performance of missing transverse momentum reconstruction for the ATLAS detector in the first proton-proton collisions at  $\sqrt{s} = 13$  TeV. Technical Report ATL-PHYS-PUB-2015-027, CERN, Geneva, Jul 2015.
- [72] Search for dark matter and other new phenomena in events with an energetic jet and large missing transverse momentum using the ATLAS detector. Technical Report ATLAS-CONF-2017-060, CERN, Geneva, Jul 2017.
- [73] Yu Nakahama. The atlas trigger system: Ready for run-2. *Journal of Physics: Conference Series*, 664(8):082037, 2015.
- [74] M. Aaboud et al. Search for pair production of higgs bosons in the  $b\bar{b}b\bar{b}$  final state using proton-proton collisions at  $\sqrt{s} = 13$  TeV with the atlas detector. *Phys. Rev. D*, 94:052002, Sep 2016.
- [75] 2015 start-up trigger menu and initial performance assessment of the ATLAS trigger using Run-2 data. Technical Report ATL-DAQ-PUB-2016-001, CERN, Geneva, Mar 2016.
- [76] Simone Alioli, Paolo Nason, Carlo Oleari, and Emanuele Re. A general framework for implementing NLO calculations in shower Monte Carlo programs: the POWHEG BOX. *JHEP*, 06:043, 2010.
- [77] Torbjorn Sjostrand, Stephen Mrenna, and Peter Z. Skands. PYTHIA 6.4 Physics and Manual. *JHEP*, 05:026, 2006.
- [78] J. Pumplin, D. R. Stump, J. Huston, H. L. Lai, Pavel M. Nadolsky, and W. K. Tung. New generation of parton distributions with uncertainties from global QCD analysis. *JHEP*, 07:012, 2002.
- [79] Peter Zeiler Skands. Tuning Monte Carlo Generators: The Perugia Tunes. *Phys. Rev. D*, 82:074018, 2010.
- [80] D. J. Lange. The EvtGen particle decay simulation package. *Nucl. Instrum. Meth. A*, 462:152, 2001.

- [81] Search for resonances in the mass distribution of jet pairs with one or two jets identified as  $b$ -jets with the ATLAS detector with 2015 and 2016 data. Technical Report ATLAS-CONF-2016-060, CERN, Geneva, Aug 2016.
- [82] Torbjorn Sjostrand, Stephen Mrenna, and Peter Z. Skands. A Brief Introduction to PYTHIA 8.1. *Comput. Phys. Commun.*, 178:852, 2008.
- [83] ATLAS Run 1 Pythia8 tunes. Technical Report ATL-PHYS-PUB-2014-021, CERN, Geneva, Nov 2014.
- [84] Richard D. Ball et al. Parton distributions with LHC data. *Nucl. Phys.*, B867:244–289, 2013.
- [85] G. Aad et al. The ATLAS Simulation Infrastructure. *Eur. Phys. J.*, C70:823–874, 2010.
- [86] Selection of jets produced in 13TeV proton-proton collisions with the ATLAS detector. Technical Report ATLAS-CONF-2015-029, CERN, Geneva, Jul 2015.
- [87] ATLAS Collaboration. Search for new phenomena in dijet mass and angular distributions from  $pp$  collisions at  $\sqrt{s} = 13$  TeV with the ATLAS detector. *Phys. Lett.*, B754:302–322, 2016.
- [88] Sergei Chekanov, Andrea Coccaro, Jeffrey Rogers Dandoy, Francesco Gescini, Andreas Korn, Thomas LeCompte, Jeremy Love, Laurie McClymont, James Proudfoot, Soo Ryu, Rui Wang, Ning Zhou, Nishu Nishu, Jinlong Zhang, Gabriel Facini, Lydia Beresford, and Tobias Golling. Search for high-mass resonances in the mass distribution of jet pairs with one or two jets identified as  $b$ -jets in proton-proton collisions at  $\sqrt{s}=13$  TeV with the ATLAS detector. Technical Report ATL-COM-PHYS-2016-515, CERN, Geneva, May 2016.
- [89] Thomas Kittelmann, Vakhtang Tsulaia, Joseph Boudreau, and Edward Moyse. The virtual point 1 event display for the atlas experiment. *Journal of Physics: Conference Series*, 219(3):032012, 2010.
- [90] Torsten Paul Ake Akesson, Adi Ashkenazi, Matteo Bauce, Harinder Singh Bawa, Lydia Beresford, Javier Bilbao De Mendizabal, Jonathan David Bossio Sola, Antonio Boveia, Lene Bryngemark, Brian Lee Clark, Jeffrey Rogers Dandoy, Merlin

- Davies, Caterina Doglioni, Gabriel John Facini, Meghan Frate, James Frost, Esteban Fullana Torregrosa, Francesco Guescini, Todd Brian Huffman, Cigdem Issever, Guy Koren, David Lopez Mateos, Bogdan Malaescu, Gino Marceca, Andrea Messina, Katherine Pachal, James Pilcher, Steven Schramm, Pavel Starovoitov, Jaryd Franklin Ulbricht, Marco Vanadia, Daniel Whiteson, Dengfeng Zhang, Ning Zhou, Zdenek Hubacek, David Strom, Benjamin William Allen, Christopher Grud, Karishma Sekhon, Junjie Zhu, Dante Eric Amidei, Jacob Searcy, John Huth, and Ricardo Piegaia. Search for New Phenomena in Dijet Events with the ATLAS Detector at  $\sqrt{s} = 13$  TeV. Technical Report ATL-PHYS-INT-2015-013, CERN, Geneva, Sep 2015.
- [91] ATLAS Collaboration. Search for resonances in the mass distribution of jet pairs with one or two jets identified as  $b$ -jets in proton–proton collisions at  $\sqrt{s} = 13$  TeV with the ATLAS detector. *Phys. Lett.*, B759:229–246, 2016.
- [92] ATLAS Collaboration. Observation of a new particle in the search for the Standard Model Higgs boson with the ATLAS detector at the LHC. *Phys. Lett.*, B716:1–29, 2012.
- [93] F. Abe et al. Search for new particles decaying to dijets in  $p\bar{p}$  collisions at  $\sqrt{s} = 1.8$  TeV. *Phys. Rev. Lett.*, 74:3538–3543, 1995.
- [94] T. Aaltonen et al. Search for new particles decaying into dijets in proton-antiproton collisions at  $s^{**}(1/2) = 1.96$ -TeV. *Phys. Rev.*, D79:112002, 2009.
- [95] S. S. Wilks. The Large-Sample Distribution of the Likelihood Ratio for Testing Composite Hypotheses. *Annals Math. Statist.*, 9(1):60–62, 1938.
- [96] J. Heinrich, C. Blocker, J. Conway, L. Demortier, L. Lyons, G. Punzi, and P. K. Sinervo. Interval estimation in the presence of nuisance parameters. 1. Bayesian approach. *ArXiv Physics e-prints*, September 2004.
- [97] Glen Cowan, Kyle Cranmer, Eilam Gross, and Ofer Vitells. Asymptotic formulae for likelihood-based tests of new physics. *The European Physical Journal C*, 71(2):1554, Feb 2011.
- [98] ATLAS Collaboration. Luminosity determination in pp collisions at  $\sqrt{s} = 8$  TeV using the ATLAS detector at the LHC. *Eur. Phys. J. C*, 76(arXiv:1608.03953).

CERN-EP-2016-117. 12):653. 71 p, Aug 2016. Comments: 53 pages plus author list + cover pages (71 pages total), 19 figures, 9 tables, submitted to EPJC, All figures including auxiliary figures are available at <http://atlas.web.cern.ch/Atlas/GROUPS/PHYSICS/PAPERS/DAPR-2013-01>.